Treatment plan optimization and delivery using dynamic gantry-couch trajectories

Joel A. Mullins

Department of Physics
McGill University

A thesis submitted to McGill University in partial fulfillment of the requirements of the degree of
Doctor of Philosophy

 December 2020

Acknowledgements

As I come to the conclusion of my thesis research, I would be remiss to not thank the numerous people who have supported me.

First, thank you to my supervisor, Jan Seuntjens, who was a valuable resource throughout my research, providing calm guidance and support. I always came out of our research discussions with a renewed sense of direction and purpose.

I would also like to acknowledge Alasdair Syme, who supervised me during my Masters research and initially set me on this trajectory research path. This topic has provided me both a deeper understanding of the technical details of medical physics, but also allowed me to gain knowledge and experience into many aspects of clinical medical physics practice, for which I am grateful.

There are many clinical medical physicists that I must thank, who have tolerated my questions and queries over the years, and generously donated their time to help with my research: François DeBlois, Russell Ruo, Monica Serban, Tanner Connell, and Krum Asiev.

Specific mention should be made to my fellow student collaborators, Marc-André Renaud and Veng Heng, for the countless discussions spent troubleshooting bugs and rooting out sources of discrepancy.

There are a multitude of friends and student colleagues that have made life in Montreal and the Medical Physics Unit not just bearable, but enjoyable. I will refrain from mentioning specific names, but if we've shared a drink or a conversation, thank you.

Finally, a very heartfelt thank you to my parents, Frazer and Anita, who have, throughout my life, always been encouraging and supportive, and enabled me to embark on this career path. As well, thank you to my brothers, Adam, Graeme, and Lee, for pushing me when we were younger, and supporting me later in life.

Thank you to all.

Abstract

In radiation therapy, trajectory-based delivery involves the dynamic motion of linear accelerator components combined with continuous arc radiation delivery. The increased complexity of the delivery may yield dosimetric advantages, but the delivery technique has not seen clinical implementation. The purpose of this thesis work is to provide support for clinical implementation of trajectory-based treatment delivery, through the application of novel trajectories, implementation of a trajectory-based optimization algorithm, and verification of the treatment delivery accuracy under dynamic conditions.

The initial study in this thesis applied translational couch trajectories to reduce the effective source-to-axis distance (SAD), with potential benefits due to the decreased projected size of the multileaf collimator and an increased effective dose rate. A noncoplanar trajectory was applied to patients presented with cranial targets, and treatment plans were optimized at shortened and standard SAD. Through comparisons to clinical treatment plans, the shortened SAD treatment plans yielded a fraction size dependent decrease in the treatment delivery time due to the increased effective dose rate. The noncoplanar trajectories yielded comparable plan quality to the clinical deliveries.

The next study focused on the novel implementation of a trajectory optimization algorithm for concurrent gantry and couch rotation. The optimization algorithm implemented uses the column generation approach to simultaneously determine the trajectory path during volumetric modulated arc therapy optimization (simTr-VMAT). With comparisons to coplanar VMAT plans and to randomly generated trajectories that represent the solution space for the optimization problem, the simTr-VMAT optimization methodology was validated.

The complex trajectory paths resulting from the simTr-VMAT optimizations were observed as a potential source of dose delivery inaccuracy. A trajectory smoothing procedure was implemented, and the base and smoothed treatment plans were delivered on the TrueBeam linear accelerator. The trajectory smoothing retained the treatment plan quality of the base trajectories. The delivery accuracy was largely within combined standard uncertainty. A systematic difference between

measurement and calculation was observed that requires further investigation. The smoothed trajectory plans yielded improved agreement with measurement compared to the base trajectory plans.

The final study investigated the gantry-couch rotation angle coordinate system. Trajectory optimizations were performed under a cartesian and spherical coordinate system for seven patient cases, using a overlap score map approach. The arclength between adjacent control points showed less variation for cases where the cartesian trajectory included arc segments with couch-only rotations. The objective function value was improved for 4 out of 7 patient cases for the spherical trajectories, but limitations of two-step trajectory optimization approaches were observed.

Through the research presented in this thesis, clinical advantages of trajectory-based delivery were demonstrated, as well as the importance of trajectory smoothing to improve the accuracy of dose delivery. This work helps to pave the way towards the clinical implementation of trajectory-based treatment delivery.

Résumé

En radiothérapie, l'administration basée sur la trajectoire implique le mouvement dynamique de composants d'accélérateur linéaire combiné à l'administration continue de rayonnement en arc. La complexité accrue de l'administration peut apporter des avantages dosimétriques, mais la technique d'administration n'a pas encore été mise en œuvre dans la pratique. L'objectif de ce travail de thèse est de fournir un soutien à la mise en œuvre clinique de l'administration de traitement basée sur la trajectoire, par l'application de nouvelles trajectoires, la mise en œuvre d'un algorithme d'optimisation basé sur la trajectoire, et la vérification de la précision de l'administration du traitement dans des conditions dynamiques.

L'étude initiale de cette thèse a appliqué des trajectoires translationnelles du divan pour réduire la distance source-axe (SAD) effective, avec des avantages potentiels dus à la taille réduite projetée du collimateur multi-feuilles et à un débit de dose efficace accru. Une trajectoire non coplanaire a été appliquée aux patients présentant des cibles crâniennes, et les plans de traitement ont été optimisés à une SAD raccourcie et standard. En comparant avec les plans de traitement cliniques, les plans de traitement à SAD raccourcis entraînent une diminution du temps de traitement en fonction de la taille de la fraction, en raison de l'augmentation du débit de dose efficace. Les trajectoires non coplanaires ont donné une qualité de plan comparable aux plans cliniques.

L'étude suivante s'est concentrée sur la nouvelle mise en œuvre d'un algorithme d'optimisation des trajectoires pour la rotation simultanée du portique et de la table. L'algorithme d'optimisation mis en œuvre utilise l'approche de génération de colonnes pour déterminer simultanément la trajectoire pendant l'optimisation de la thérapie par arc modulé volumétrique (simTr-VMAT). La méthodologie d'optimisation simTr-VMAT a été validée par des comparaisons avec des plans de VMAT coplanaires et des trajectoires générées de manière aléatoire qui représentent l'espace de solution du problème d'optimisation.

Les trajectoires complexes résultant des optimisations simTr-VMAT ont été observées comme une source potentielle d'imprécision dans l'administration des doses. Une procédure de lissage des trajectoires a été mise en œuvre, et les plans de base et lissés ont été livrés à l'aide d'un

accélérateur linéaire TrueBeam. Le lissage des trajectoires permettait de conserver la qualité des plans de traitement des trajectoires de base. La précision de l'administration était largement dans les limites de l'incertitude standard combinée. Une différence systématique entre la mesure et le calcul a été observée, ce qui nécessite une étude plus approfondie. Les plans de trajectoires lissés ont donné une meilleure concordance avec la mesure par rapport aux plans de trajectoires de base.

L'étude finale a examiné le système de coordonnées de l'angle de rotation du portique. Des optimisations de trajectoires ont été réalisées sous un système de coordonnées cartésien et sphérique pour sept cas de patients, en utilisant une approche de carte de scores de chevauchement. La longueur d'arc entre les points de contrôle adjacents a montré moins de variation pour les cas où la trajectoire cartésienne comprenait des segments d'arc avec des rotations uniquement au niveau de la table de soin. La valeur de la fonction objectif n'a été améliorée que pour 4 cas sur 7 pour les trajectoires sphériques, mais les limites des approches d'optimisation des trajectoires en deux étapes ont été démontrées.

Grâce aux recherches présentées dans cette thèse, les avantages cliniques de l'administration basée sur les trajectoires ont été démontrés, ainsi que l'importance du lissage des trajectoires pour améliorer la précision de l'administration des doses. Ce travail fournit une justification supplémentaire pour la mise en œuvre clinique de l'administration de traitement basée sur la trajectoire.

Contents

List of Figures

List of Tables

List of Abbreviations

3DCRT	Three-Dimensional Conformal Radiation Therapy
AAA	Analytical Anisotropic Algorithm
AAPM	American Association of Physicists in Medicine
APBI	Accelerated Partial Breast Irradiation
BEV	Beam's Eye View
BAO	Beam Angle Optimization
BOO	Beam Orientation Optimization
CCCS	Collapsed Cone Convolution Superposition
CPE	Charged Particle Equilibrium
CT	Computed Tomography
CTV	Clinical Target Volume
EBRT	External Beam Radiation Therapy
EDK	Energy Deposition Kernel
DAO	Direct Aperture Optimization
DD	Dose Difference
DTA	Distance-To-Agreement
DV	Dose-Volume

DVH	Dose Volume Histogram
FFF	Flattening Filter-Free
FMO	Fluence Map Optimization
gEUD	Generalized Equivalent Uniform Dose
GTV	Gross Tumour Volume
ICRU	International Commission on Radiation Units and Measurements
IMRT	Intensity Modulated Radiation Therapy
ITV	Internal Target Volume
KERMA	Kinetic Energy Released per Unit Mass
KKT	Karush-Kuhn-Tucker
MC	Monte Carlo
MLC	Multileaf Collimator
MP	Master Problem
MU	Monitor Unit
NTCP	Normal Tissue Complication Probability
OAR	Organ-At-Risk
PDD	Percent Depth Dose
PE	Photoelectric Effect
PP	Pair Production
PRV	Planning Organ-At-Risk Volume
PTV	Planning Target Volume
RMP	Restricted Master Problem

RMSE	Root Mean Square Error
ROI	Region Of Interest
SAD	Source-to-Axis Distance
SBRT	Stereotactic Body Radiation Therapy
SSD	Source-to-Surface Distance
SRS	Stereotactic Radiosurgery
TCP	Tumor Control Probability
TCPE	Transient Charged Particle Equilibrium
TERMA	Total Energy Released per Unit Mass
Tr-VMAT	Trajectory Volumetric Modulated Arc Therapy
VMAT	Volumetric Modulated Arc Therapy
XML	Extensible Markup Language

Preface

Contribution to original knowledge

The thesis is comprised of four manuscripts, two of which are published in *Medical Physics*, with the remaining two manuscripts in preparation. Each manuscript represents original contributions to knowledge. In particular:

- The use of translational couch motion to shorten the effective treatment distance
- The implementation of a novel trajectory optimization technique that simultaneously generates a trajectory path with treatment plan optimization
- The implementation of a trajectory smoothing procedure, and the delivery and measurement of complex trajectory-based plans
- The implementation of a trajectory optimization under a spherical coordinate system

Each of the above items had not previously been presented in the literature.

Contribution of Authors

Chapters 1-4 provide an introduction to the area of research, and Chapter 9 summarizes the thesis work, and for each of these chapters, I was the sole author. Jan Seuntjens provided proofreading and review for each of these chapters. Marc-André Renaud reviewed the French translation of the abstract. Chapters 5-8 contain the manuscripts, with the author contributions for each described in the following:

- *Joel Mullins, Marc-André Renaud, Veng Heng, Russell Ruo, François DeBlois, Jan Seuntjens. "Trajectory-based VMAT for cranial targets with delivery at shortened SAD", Medical*

Physics 47, 3103-3112, 2020. (Chapter 5)
I was involved in the design of the study, performed the treatment plan optimizations, final dose calculations, and the plan delivery and measurements, and also analyzed the results, and wrote the manuscript. Marc-André Renaud developed the VMAT optimization framework and the beamlet dose calculation algorithm. Veng Heng assisted with the plan delivery and measurements. Russell Ruo selected patient cases for the study, and provided clinical expertise in the treatment planning process and interpretation of the results. François DeBlois assisted in the design of the study. Jan Seuntjens assisted in the design of the study. Each co-author reviewed the manuscript.

- *Joel Mullins, Marc-André Renaud, Monica Serban, Jan Seuntjens. "Simultaneous trajectory and volumetric modulated arc therapy optimization", Medical Physics 47, 3078-3090, 2020.* (Chapter 6)
  I designed the study, implemented the trajectory optimization algorithm, performed the random trajectory optimizations, analyzed the data, and wrote the manuscript. Marc-André Renaud developed the underlying optimization framework that the trajectory optimization algorithm interfaced with, and wrote the beamlet dose calculation algorithm. Monica Serban provided clinical expertise in optimizing the coplanar VMAT treatment plans and the trajectory-based treatment plans, and in the interpretation of the results in a broader clinical context. Jan Seuntjens contributed to the interpretation of the results. Each co-author reviewed the manuscript.

- *Joel Mullins, Veng Heng, Jan Seuntjens. "Delivery verification of trajectory-based treatment plans", in preparation.* (Chapter 7)
  I designed the study, implemented the smoothing algorithm and the conversion of the optimization to a deliverable treatment plan, and performed the treatment plan delivery and dose calculations, as well as analyzed the results and wrote the manuscript. Veng Heng assisted in the treatment plan delivery, analyzed the radiochromic film results, and aided in the interpretation of the results. Jan Seuntjens assisted in the treatment plan delivery and the interpretation of the results, and reviewed the manuscript.

- *Joel Mullins, Jan Seuntjens. "Spherical decomposition for trajectory-based delivery", in preparation.* (Chapter 8)
  I designed the study, defined the trajectory optimization workflow under each coordinate system, performed the optimizations, analyzed the results, and wrote the manuscript. Jan Seuntjens assisted in the interpretation of the results and reviewed the manuscript.

1 Introduction

1.1 Introduction

The diverse class of diseases characterized by abnormal cell growth and the potential to spread throughout the body are collectively referred to as cancer. The inability to control the local growth of the primary cancerous tumour or the metastatic spread to secondary locations in the body inevitably leads to patient death [1]. Cancer is the leading cause of death in Canada, accounting for 30% of all deaths, with 225 000 new cancer cases resulting in 80 000 deaths projected for 2020 [2].

The medicine of cancer is called oncology, with surgery, chemotherapy, and radiation therapy as the primary treatment modalities, but other approaches such as immunotherapy or hormone therapy can be included as part of a patient's course of treatment [3]. The intent of oncological treatment may be curative, to eradicate the disease, or palliative, to manage or alleviate symptoms resulting in an improved quality of life [1]. Surgery is the primary treatment for most solid malignancies, in which the gross and microscopic tumour are resected. Chemotherapy is a systemic treatment that employs chemical compounds that preferentially interferes with the proliferation of cancer cells when introduced into the bloodstream of a patient. With radiation

therapy, the delivery of radiation to the tumour volume induces lethal genomic damage to cells. The treatment intent and regimen are dependent on a multitude of factors, including cancer site, severity, and evidence of metastatic spread [3]. In estimating the primary modality for patients with successful curative treatment regimens, 49% were attributed to surgery, 40% were attributed to radiation therapy, and 11% were attributed to chemotherapy [1]. Cancer treatments commonly require a multidisciplinary approach of treatment options, with 50% of cancer patients estimated to benefit from the inclusion of radiation therapy to their treatment regimen [4].

1.2 Radiation Therapy

1.2.1 Overview

Radiation therapy, or radiotherapy, uses ionizing radiation to target and eradicate tumours, through the liberation of electrons and reactive oxygen species that inflict lethal genomic damage to cells [3]. There are two categories of ionizing radiation: i) directly ionizing, in which charged particles (electrons, protons, or heavy ions) deposit energy into a medium directly through Coulombic interactions; ii) indirectly ionizing, in which uncharged particles (photons, neutrons) first interact in a medium to release charged particles, which then proceed to deposit energy directly. The unit for energy deposition in a medium, or dose, is the gray (Gy), defined as 1 joule per kilogram ($J \cdot kg^{-1}$) [5]. The principal cause of cell death due to radiation deposition is attributed to double-strand breaks of the DNA molecules within the nucleus of a cell. A radiation dose of 1 Gy yields on the order of 10^5 ionization events within a cell, and approximately 40 double-strand breaks [3].

The aim of radiotherapy is to achieve local control of the tumour while minimizing the potential for complications in the surrounding healthy tissue. The tumour control probability (TCP) and the normal tissue complication probability (NTCP) are often represented as sigmoid curves as a function of radiation dose (Fig. 1.1). In an idealized scenario, the function representing the TCP is situated at a lower dose than the NTCP, defining a therapeutic window at which a high probability of tumour eradication can be achieved without substantial risk of normal tissue complication. In practice, this therapeutic window may not exist, and achieving tumour control without normal tissue complications requires a radiation treatment and fractionation (or treatment regimen describing the amount of dose delivered per radiation therapy session) customized to the patient anatomy and presentation of the disease.

Radiation therapy treatment can be delivered through the insertion of radioactive sources into or near the tumour volume (brachytherapy), or by generating radiation externally to the patient

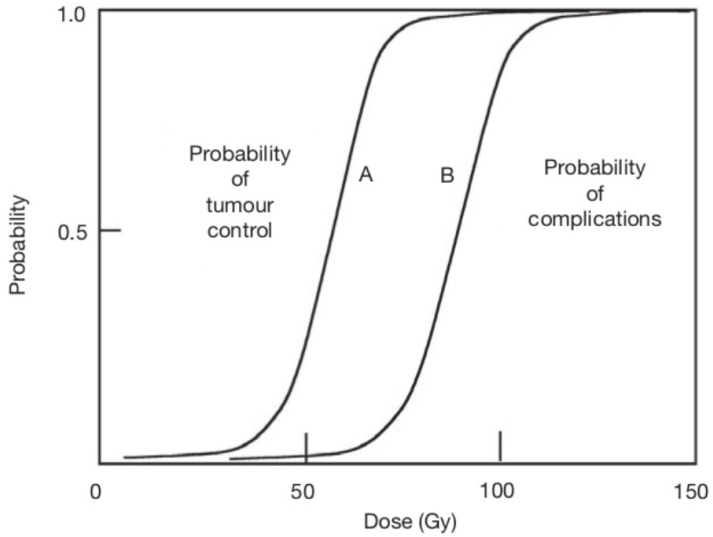

Figure 1.1 The probability of tumour control (TCP) and normal tissue complications (NTCP) are represented as sigmoids as a function of dose. Reproduced from Podgorsak [5].

and directing the radiation beam towards the tumour volume (external beam radiation therapy, EBRT). EBRT delivery modalities include kilovoltage x-ray tubes, Cobalt-60 treatment units, proton accelerators (cyclotrons, synchrotrons), but conventional clinical practice mainly uses linear accelerators to generate electron or photon radiation beams [3, 5].

1.2.2 Linear Accelerators

In conventional photon and electron radiotherapy, the nominal beam energies range between 4 MeV to 25 MeV, and are produced with linear accelerators (linacs). Through thermionic emission, electrons are emitted from a cathode into a waveguide and are accelerated using a radiofrequency power source. The accelerated electrons are redirected using bending magnets upon exiting the waveguide, and will then interact with components to define the beam characteristics. For electron treatment beams, a thin scattering foil is used to disperse the electrons into a broader field. For photon treatment beams, a target is placed in the path of the accelerated electrons, yielding photons through bremsstrahlung interactions. A flattening filter may be used to further adjust the lateral intensity of the photon beam. Due to the lack of a target for electron beams, the electrons are nearly monoenergetic upon exiting the linear accelerator, and the beam is often labelled by this energy (*e.g.* a 6 MeV electron beam). Clinical photon beams produced through bremsstrahlung interactions are polyenergetic, but are by convention labelled by their peak energy (*e.g.* 6X or 6

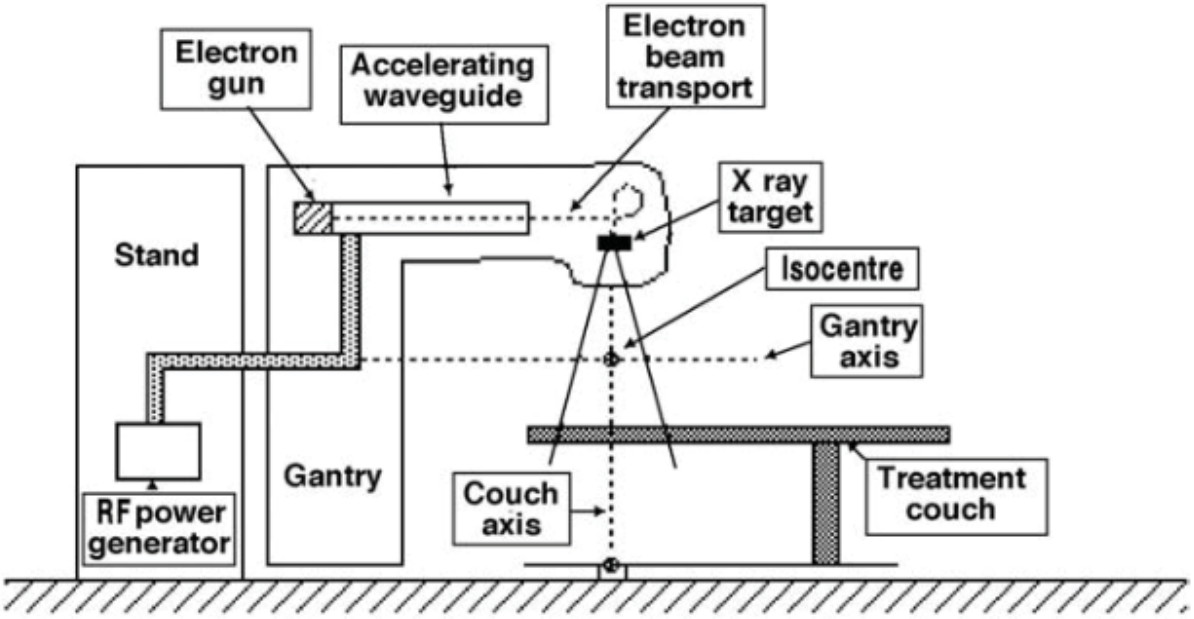

Figure 1.2 Schematic of a conventional linear accelerator. Reproduced from Podgorsak [5].

MV photons). For photon beams that do not use a flattening filter, the acronym FFF (flattening filter-free) is appended to the beam energy descriptor (*e.g.* 6X-FFF). Flattening filter-free beams have a softer energy spectrum (lower average energy) but with a drastically increased fluence rate.

The radiation field can be shaped using collimating jaws to define rectangular fields, and may be further refined into irregular shapes using a multileaf collimator (MLC), which arranges opposing pairs of thin leaves, composed of a high Z material (often tungsten), that can be translated orthogonally to the radiation beam. The linear accelerator assembly and beam shaping components are commonly mounted on a C-arm gantry that can be rotated in a 360° arc around the treatment isocentre. During treatment, the patient is positioned on a treatment couch that can both be rotated and moved translationally. The treatment head assembly (namely, the collimating jaws and MLC) can also be rotated around the beam central axis. Fig. 1.2 depicts a simplified schematic of a linear accelerator treatment unit [5].

1.2.3 Treatment Planning Workflow

Following the diagnosis of cancer, an oncologist may recommend a course of radiotherapy treatment. Conventional treatments are fractionated, in which the prescribed dose is divided into multiple dose fractions between 1.8-2 Gy and delivered over a time period of 6-8 weeks.

Alternatively, advances in treatment accuracy have led to hypofractionation with higher doses delivered in fewer fractions. Stereotactic radiosurgery (SRS) often refers to single fraction treatments for cranial targets, while stereotactic body radiation therapy (SBRT) refers to few treatment fractions (less than 10) for extracranial targets, such as in the liver or lung. The high treatment doses associated with stereotactic treatments places additional importance on accurate and precise treatment delivery [3, 6, 7].

For megavoltage photon external beam radiation therapy, the treatment planning workflow follows four essential steps [5]:

1. **Computed Tomography Scan**: For the purposes of treatment planning, a computed tomography (CT) scan is necessary to identify the location and extent of the tumour and surrounding anatomy. CT is an imaging modality that uses transmission measurements of kilovoltage x-rays delivered from numerous projection angles around the patient to reconstruct a three-dimensional (voxelized) representation of the patient anatomy [8]. A typical CT scan is arranged as axial slices of the patient with image resolution of 2.5 mm $\times$ 2.5 mm, with a slice thickness of 3 mm. For smaller target volumes, such as brain metastases, a higher resolution may be required on the order of 1 mm. The patient position during the planning CT scan will match the setup during treatment delivery, including the use of immobilization devices such as thermoplastic masks. Fiducial markers may be used to aid in replicating the CT positioning during treatment delivery [5].

2. **Contouring**: For each axial slice of the patient CT image, relevant anatomical structures are delineated with contoured regions-of-interest (ROIs), including the tumour and critical normal structures. In clinical practice, the target volume is conceptualized as several overlapping volumes to account for biological and physical uncertainties inherent to the radiation therapy workflow. The gross tumour volume (GTV) encompasses the visible tumour, identified through clinical examination or imaging techniques, and represents the minimum volume that must receive an adequate dose in order to achieve local tumour control. There is often subclinical malignant growth that is suspected but not observed, and an additional margin is added to the GTV, defining the clinical target volume (CTV). The position, shape, and size of the tumour volume may also vary as a result of patient physiology, such as respiratory motion, and the internal target volume (ITV) is defined to include a margin for these factors. The added margin may be asymmetrical based on the potential anatomical motion of the CTV. The planning target volume (PTV) further extends the ITV to account for uncertainties in patient setup or radiation delivery, and is defined to

ensure that the radiation dose prescription is delivered to the CTV. Organ-at-risk (OAR) volumes delineate structures that have specific dose tolerances that must be considered during treatment planning, and may also include margins analogous to the definition of the PTV (labelled as a planning organ-at-risk volume, or PRV) [9–11, 7].

3. **Treatment Planning**: The characteristics of a treatment plan, including beam orientations and energy, PTV prescription dose and OAR dose limits, fractionation scheme, and treatment delivery method, are often defined in clinical protocols or by recommendation of a radiation oncologist. Treatment planning is performed with the aid of computer software that provides visualization of the patient CT data and contoured volumes, and includes dose calculation algorithms for evaluation of the treatment plan dose distribution and its adherence to the planning criteria. The planning process can be forward-planned, in which the treatment planner manually adjusts the beam orientation, weight, or field boundaries iteratively to achieve the treatment objectives. Treatment plans with increased complexity can be generated using inverse-planning, in which a treatment planner defines an objective function representing the therapeutic goals, and the planning software will optimize a treatment to minimize the objective function. The objective function is typically defined as a sum of dose-volume constraints that describe threshold dose limits for a percentage of a structure volume, either as upper limits (X% of structure cannot receive more than Y Gy) or as lower limits for the target volume prescription dose (X% of structure must receive at least Y Gy). Inverse treatment plan optimization will be expanded on in Chapter 3. A comparison of forward and inverse treatment planning workflow is shown in Fig. 1.3. In both cases, iterative adjustments to the planning parameters are typically required before a clinically acceptable treatment plan is achieved [11].

4. **Treatment Delivery**: Confidence in the normal functioning of the linear accelerator is attained through quality assurance testing, and can be repeated on a daily, monthly, quarterly, or annual, basis. Quality assurance testing includes evaluation of the mechanical positioning of the linear accelerator components, and consistency in the radiation output and beam characteristics.

   During treatment delivery, the patient is positioned to closely match the setup of the planning CT scan, using kV x-ray projection images or cone-beam CT scans to align the patient based on fiducial markers or anatomical landmarks such as bony anatomy. Following verification of the patient position, the planned treatment delivery can proceed [5].

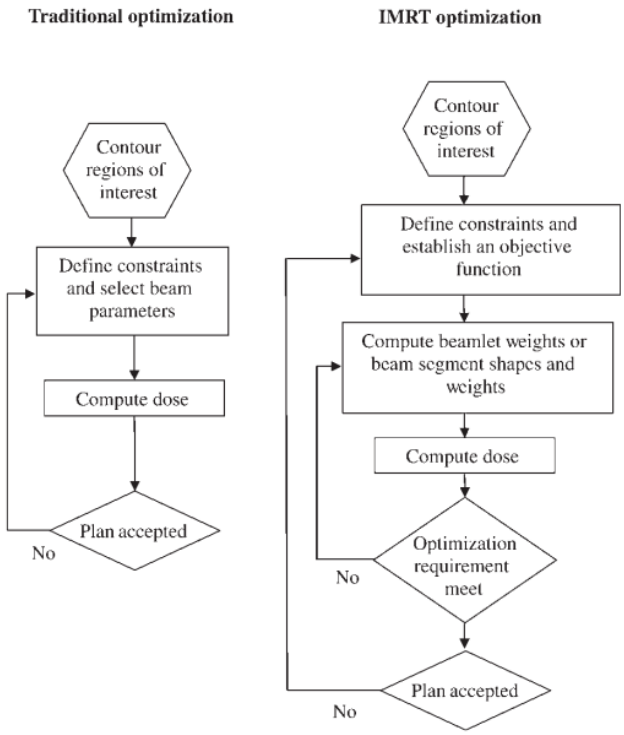

Figure 1.3 Comparison of forward and inverse (intensity modulated radiation therapy, IMRT) treatment planning workflow. Reproduced from ICRU Report 83 [11].

1.2.4 External Beam Radiation Therapy Modalities

Early Radiation Therapy Innovations

Over the history of modern photon radiotherapy, technological advances have improved the quality of treatment plans that are able to be delivered to the patient. The development of 3D imaging with computed tomography and magnetic resonance imaging have led to increased confidence in the tumour boundaries and surrounding critical structures. Additionally, the multileaf collimator was introduced, enabling complex-shaped fields that could tightly conform to the target volume. In combination, these innovations led to three-dimensional conformal radiation therapy (3D-CRT), which conventionally refers to an arrangement of beams in which the MLC aperture is shaped to the tumour volume projection for each beam's eye view [3].

Intensity Modulated Radiation Therapy

With improved computing infrastructure, optimization techniques were adopted into radiotherapy treatment planning. Intensity modulated radiation therapy (IMRT) was developed on the observation that nonuniform radiation intensity patterns from various beam orientations could be combined synergistically to yield an improved dose distribution, especially for complex-shaped target volumes. In practice, nonuniform fluence distributions from a given beam orientation can be achieved by subdividing a field into multiple smaller segments of varying intensity, referred to as segmental IMRT, static MLC IMRT, or step-and-shoot IMRT. Alternatively, a nonuniform fluence distribution can be achieved with a single unidirectional sweep of the MLC leaves, referred to as dynamic MLC IMRT, or sliding window IMRT [11, 12].

Volumetric Modulated Arc Therapy

The benefits of IMRT include the ability to deliver highly conformal dose distributions while sparing healthy tissue, but often at the cost of an increased treatment time and linear accelerator monitor unit output. Increases in treatment time have raised concerns about patient comfort and intrafraction motion [13, 14], while increased MU output leads to increased low dose radiation delivered to patients due to transmission through highly modulated fields, with an associated risk in secondary radiation-induced malignancies [15].

The concept of arc-based radiation therapy employing MLC-defined apertures to modulate the fluence was initially proposed by Yu *et al.* in 1995, but arc-based delivery never gained clinical adoption, in part due to the lack of efficient inverse planning algorithms [16]. In 2008, Otto

introduced an optimization algorithm based on simulated annealing and progressively increasing beam angle sampling that could obtain a computationally tractable treatment plan with comparable plan quality to IMRT while reducing treatment time and monitor unit output, called volumetric modulated arc therapy (VMAT) [17]. In contrast to IMRT, only a single intensity profile is defined at a given beam orientation, but instead, the dose distribution is modulated through arc-based delivery over a larger patient volume. Following this publication, VMAT has been widely adopted into clinical practice [15]. Conventional clinical practice includes each of 3D-CRT, IMRT, and VMAT, with the choice of technique dependent on the treatment site and clinical infrastructure and expertise.

Trajectory-based Treatment Delivery

The introduction of the TrueBeam linear accelerator (*c.* 2010) by Varian Medical Systems (Palo Alto, CA, USA) included a non-clinical research environment called "developer's mode". This environment enabled customized treatment plans with dynamic motion of linear accelerator components including gantry rotation, treatment couch rotation and translation, and collimator rotation; the dynamic motion of these components is referred to as a trajectory. With trajectory-based delivery, improved treatment outcomes may be achieved, such as through avoidance of critical structures, or steeper dose gradients using noncoplanar beam orientations. Despite the purported benefits of trajectory-based treatment plans, the increased complexity and concerns for the treatment delivery accuracy and patient safety have prevented clinical implementation [18].

1.3 Thesis Objectives

This thesis presents research to demonstrate the feasibility of trajectory-based radiotherapy in a clinical environment, including the application of novel trajectories, the development of a trajectory-based optimization methodology, and evaluation of radiation delivery accuracy for trajectory-based treatment plans. The objectives of this work were the following:

- To implement trajectory-based treatment plans with a shortened treatment distance, and to quantify the associated benefits to clinical workflow and patient standard of care. Radiotherapy at a shortened treatment distance yields potential advantages including a reduced MLC leaf width at treatment isocentre and an increased effective dose rate, and can be implemented through translational couch motion in synchrony with gantry rotation.

- To develop and validate an optimization methodology that determines the gantry angle-couch angle trajectory path simultaneously with volumetric modulated arc therapy optimization, leveraging the column generation approach to iteratively construct trajectory-based treatment plans.
- To assess the clinical viability of trajectory-based treatment plans with regard to dose delivery accuracy during complex dynamic trajectory motion.
- To determine advantages of trajectory-based treatment plan optimization under a spherical coordinate system rather than a gantry-couch angle coordinate system.

1.4 Thesis Outline

This introductory chapter outlined the background of radiation therapy practice for the treatment of cancer, and introduces modern treatment delivery techniques, leading to the description of trajectory-based delivery and the objectives of this thesis. In Chapter 2, topics related to clinical dosimetry are described, with the basic physical processes of radiation in matter, dosimetry measurements, and dose calculation algorithms. Chapter 3 introduces the mathematical background for nonlinear optimization, forming the basis of modern radiation therapy treatment planning, and introduces the column generation approach applied to treatment plan optimization, which is featured prominently throughout this thesis. Chapter 4 reviews the current literature of trajectory-based treatment planning, and provides the context for the objectives of this thesis. Chapter 5 is a manuscript published in *Medical Physics* on the implementation of a patient-generalized trajectory applied to patients presented with cranial targets, using translational couch motion to reduce the effective treatment distance [19]. Chapter 6 is a manuscript published in *Medical Physics* on the development and validation of a simultaneous trajectory and volumetric modulated arc therapy optimization algorithm [20]. In Chapter 7, a study investigating the radiation delivery accuracy of complex trajectory-based treatment plans, as well as the implementation of a trajectory-smoothing procedure, is presented. Chapter 8 investigates the use of a spherical coordinate system for trajectory-based delivery in place of the conventional gantry-couch coordinate system used in the literature. A conclusion of this thesis is given in Chapter 9, as well as discussion of future trajectory-based treatment delivery research directions.

2

Clinical Dosimetry

Preface

The work presented in this thesis pertains directly to modern radiotherapy practice. This chapter introduces the basic radiation physics on which radiotherapy is founded, and proceeds to discuss clinical dosimetry methods, dose calculation algorithms used for treatment planning, and related clinical procedures.

2.1 Physical interactions

2.1.1 Photons

There are three dominant mechanisms by which photons deposit energy to a medium in the clinical radiotherapy energy range (4-25 MV): photoelectric effect, Compton scattering, and pair production. With each interaction, there is a transfer of the photon kinetic energy to secondary charged particles (electrons) which are released into the medium.

A photoelectric effect interaction may occur when a photon is absorbed by a bound (inner shell) electron of an atom, and the incident photon energy exceeds the binding energy of the electron to the atomic nucleus. The kinetic energy of the resultant electron is equal to the incident photon energy less the binding energy. The vacancy produced in the inner electron shell due to the released electron may be filled by higher shell electrons, with the difference in binding energy being emitted as characteristic photons or Auger electrons released into the medium.

Compton scattering is a process in which a photon interacts with a loosely bound (valence shell) electron, imparts a portion of its energy to the electron, and both particles scatter into the medium. Prior to the interaction, the electron is considered free and stationary due to the incident photon energy greatly exceeding the electron binding energy.

The production of an electron-positron pair can occur when a photon interacts with a nucleus and the incident photon energy exceeds 1.022 MeV, equal to the rest mass of the resultant particles (neglecting a very small energy fraction going to momentum conservation). The interaction with the nucleus is necessary for the conservation of momentum, but may also occur with an orbital electron, resulting in the release of the electron-positron pair as well as the orbital electron into the medium (triplet production). The threshold energy for triplet production, due to recoil of the orbital electron, is 2.044 MeV.

The absorption of a high-energy photon by the nucleus of an atom, resulting in the emission of a neutron or proton and the nucleus becoming radioactive, is called a photonuclear interaction. The threshold energy for photonuclear reactions for the atoms that are relevant in radiation therapy is approximately 10 MeV. The contribution of photonuclear interactions to attenuation of the photon beam amounts to only a few percent above the threshold energy.

An additional interaction may occur called Rayleigh scattering, but this is an elastic collision that scatters the photon at a small angle and does not transfer energy to the medium, contributing only to narrow-beam photon attenuation.

Fig. 2.1 shows the relative dominance of each of these interactions as a function of energy and atomic number Z of the medium. For therapeutic energy ranges of 4-25 MV and a soft tissue effective atomic number of approximately $Z_{\text{eff}} = 7.5$, Compton interactions are the most prevalent [5, 21].

2.1.2 Electrons

Electrons traversing a medium undergo Coulombic interactions with nearby orbital electrons and nuclei. The type of interaction is dependent on the distance of the electron relative to the atomic

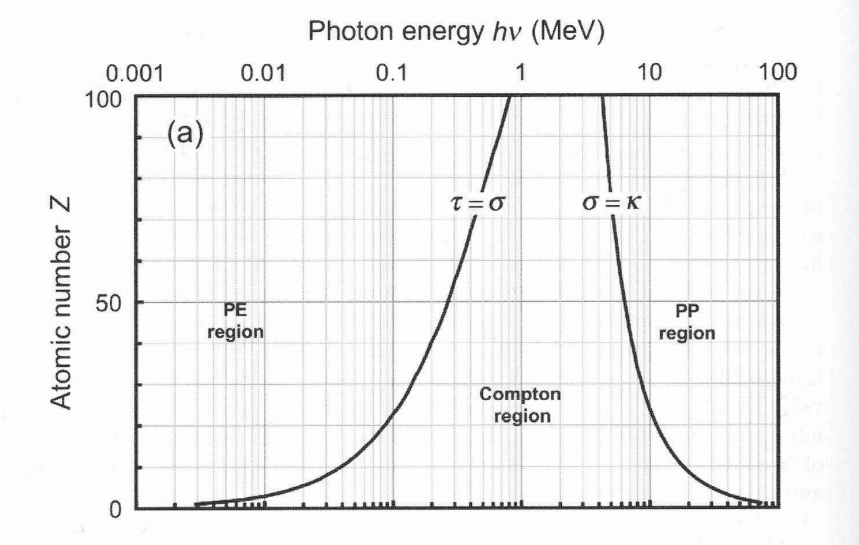

Figure 2.1 Dominant regions of photon interactions as a function of incident photon energy and atomic number of the medium. Lines indicate regions of equal contribution between adjacent regions. Photoelectric effect (PE): τ; Compton scattering: σ; pair production (PP): κ. Reproduced from Podgorsak [21].

nucleus, called the impact parameter. Soft collisions can occur when the impact parameter is large, as the incident electron may induce excitations of electrons to higher energy states or ionize valence electrons. Approximately 50% of energy loss by a charged particle in a medium is due to soft collisions. When the impact parameter is on the order of the classical atomic radius, a hard collision may occur with a direct Coulomb impact releasing an orbital electron into the medium. For a small impact parameter, the electron primarily interacts with the positively-charged nucleus, and radiative (bremsstrahlung) processes can occur with the change in velocity of the electron yielding an emitted photon [5, 21].

2.1.3 Radiation beam in matter

The work described in this thesis focuses on external beam photon radiotherapy. When a photon beam is impinging on a medium, the photoelectric effect, Compton scattering, and pair production interactions occur, releasing secondary charged particles into the medium which in turn result in further ionizations, excitations, and bremsstrahlung photons. As these interactions occur, the photon intensity is attenuated as a function of depth.

A useful quantity is the kinetic energy released by the primary photon interactions, called KERMA (kinetic energy released per unit mass). KERMA is often split based on the resulting sec-

ondary electron interactions as either electronic (or collisional) KERMA (K_{el} or K_{col}) for soft/hard collisions, or radiative KERMA (K_{rad}) for bremsstrahlung interactions or positron/electron annihilation resulting in the emission of photons that exit the local region without further energy deposition. K_{col} is closely related to the dose deposition in a medium, but the location at which kinetic energy is transferred does not necessarily coincide with the location where the energy is ultimately deposited due to the nonzero range of the secondary electrons [5].

K_{col} is maximized on the surface due to the attenuation of a photon beam as a function of depth. The secondary electrons released in the medium preferentially travel in a forward direction, resulting in a build-up region prior to the depth of maximum dose deposition. At the depth of maximum dose, the condition of charged particle equilibrium (CPE) has been established, where electrons entering a depth are offset by electrons being mobilized downstream. Due to attenuation and scattering of the photon beam, only transient charged particle equilibrium (TCPE) can occur beyond the depth of maximum dose [5]. Radiation fields are often characterized by a percentage depth dose (PDD) curve, which illustrates the dose deposition as a function of depth, relative to the maximum dose (Fig. 2.2a).

2.2 Dosimetry

Characterizing the radiation output of a linear accelerator is important for accurate dose calculations during the treatment planning process as well as for treatment delivery. The field of radiation dose measurements is called dosimetry, and devices that measure dose are called dosimeters. This section introduces the concepts of reference and relative dosimetry, as well as two dosimeters that are used in this thesis work.

2.2.1 Reference Dosimetry

Reference dosimetry is the term used when referring to the output calibration of a clinical linear accelerator through measurements under a specific set of clinical reference conditions. The American Association of Physicists in Medicine (AAPM) Task Group 51 delineated an ionization chamber-based protocol for performing reference dosimetry measurements [22]. The recommended reference conditions include: a 30 cm $\times$ 30 cm $\times$ 30 cm water phantom (or larger); a radiation field size of 10 cm $\times$ 10 cm; a source-to-surface distance (SSD) of 100 cm (if using an SSD setup); a point of measurement at 10 cm depth on the radiation beam central axis (for photon

beam reference dosimetry). The dose measurement using an ionization chamber at that point is given by:

$$D_w^Q = M_{\text{corr}} N_{D,w}^Q \tag{2.1}$$

where M_{corr} is the ionization chamber charge measurement, with correction factors applied for variations in temperature and pressure, ion recombination in the chamber, polarity effects, and the electrometer used for the measurement. $N_{D,w}^Q$ is an absorbed dose-to-water calibration coefficient, where Q denotes the beam quality, and D,w indicates the conversion of the measurement to dose-to-water. The beam quality Q is a parameter that represents the energy characteristics of the radiation beam as a single value. The $N_{D,w}^Q$ factor is a quantity that is traceable through cross-calibration to a national standards laboratory (in Canada, the National Research Council).

Through a reference dosimetry measurement, the linear accelerator output (defined in monitor units, MU) can be calibrated to correspond to a specific dose output in a water phantom. Commonly, the output is defined such that 100 MU corresponds to deposition of 1 Gy at the depth of maximum dose for a 10 cm $\times$ 10 cm field and an SSD of 100 cm. In order to calibrate the output to the depth of maximum dose, relative dose measurements of the percentage depth dose deposition must also be performed.

2.2.2 Relative Dosimetry

Further characterization of a linear accelerator output is performed through relative dosimetry measurements, where the data are normalized to a characteristic measurement point. Examples include the percentage depth dose (PDD) which characterizes the dose deposition on the beam central axis as a function of depth and normalized as a percentage of the maximum dose, or field profile measurements that describe in-plane, cross-plane, and diagonal characteristics of a field relative to the measurement on the beam central axis. Fig. 2.2 shows relative dose measurements for a 6 MV photon beam (flattening filter-free), with a 10 cm $\times$ 10 cm field and an SSD of 100 cm. A comprehensive set of relative dosimetry measurements under a variety of measurement conditions are necessary for the commissioning of dose calculation algorithms used for treatment planning [23].

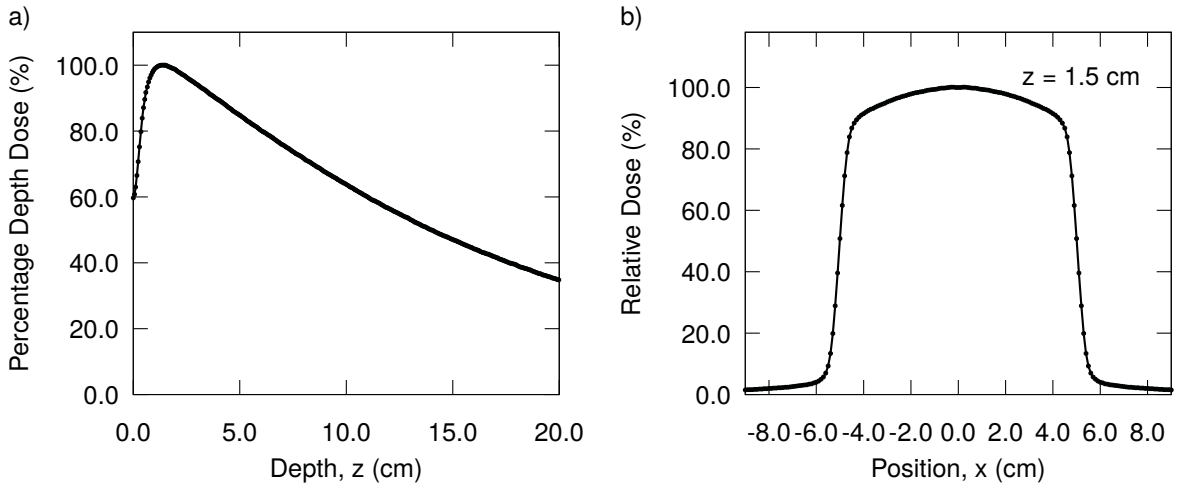

Figure 2.2 Relative dose measurements for a 6X-FFF radiation beam with a 10 cm $\times$ 10 cm field size. a) percentage depth dose curve; b) cross-plane field profile at a measurement depth of 1.5 cm.

2.2.3 Dosimeters

Ionization Chambers

Ionization chambers are a commonly used dosimeter in radiation therapy that provides a point dose measurement. Cylindrical ionization chambers consist of a gas-filled (usually air) chamber with a central collecting electrode and a conductive outer wall. By applying a voltage across the electrode and wall, ion pairs produced in the chamber by ionizing radiation will be collected and contribute to a charge measurement that can be read out by an electrometer. As explained in the reference dosimetry section, by applying correction factors to the charge measurement and multiplying by an absorbed dose-to-water calibration coefficient, the measured dose can be determined [5].

Radiochromic Film

Upon exposure to ionizing radiation, the active emulsion layer of radiochromic film polymerizes, resulting in a visible colour change. The relationship between dose and the colour change response can be modeled through calibration measurements by irradiating film to known doses, with a flat-bed scanner used to separate the film response into red/green/blue (RGB) colour channels. Film read-out cannot be performed immediately following irradiation as the film response takes up

to 24 h to stabilize [5]. Radiochromic film is not recommended for absolute dose measurements, but as a relative two-dimensional (planar) dosimeter [24].

2.3 Dose Calculation Algorithms

An integral component of the radiation therapy workflow is the simulation of treatment plan parameters to predict the dose distribution within a patient. As part of the dose calculation, each voxel in the 3D patient CT data will be assigned a dose value, which allows evaluation of the treatment plan quality. Among dose calculation algorithms, there is often a trade-off between accuracy and computational efficiency.

2.3.1 Monte Carlo

The Monte Carlo (MC) technique applied to medical physics involves the simulation of individual particles (histories) as they are transported in a predefined geometry, using random sampling of interaction cross section data to determine the physical interactions that occur during the simulation. The physical interactions, resulting direction, energy, and secondary particles that may be produced are determined based on the cross section data, and continue until the particle energy is below a threshold, at which point it is assumed that the remaining energy is deposited locally, or the particle leaves the simulation environment. In clinical treatment planning, MC simulations are used to determine the macroscopic dose distribution by summing the energy deposition in a voxelized patient or phantom geometry, and is considered a gold standard for dose calculation accuracy. The Type A (or statistical) uncertainty in the dose distribution is dependent on the number of particles simulated, and decreases as $\frac{1}{\sqrt{N}}$, where N is the total number of histories, typically on the order of 1 million - 1 billion to achieve an uncertainty of less than 1% [25].

2.3.2 Convolution Superposition

Due to the long computation times that may be required for MC dose calculations, analytical dose calculations are typically used in a clinical environment. By separately calculating the TERMA (total energy released per unit mass) for a field arrangement and convolving TERMA with a MC-based energy deposition kernel (EDK) that describes the distribution of energy around a primary photon interaction point, a dose distribution can be obtained by summing each of the convolutions (superposition). Polyenergetic EDKs are often calculated as a weighted sum of

monoenergtic EDKs based on the photon beam fluence spectrum [26]. Scaling approximations are used to account for the impact of density and material heterogeneity on the EDK.

Analytical Anisotropic Algorithm

The Analytical Anisotropic Algorithm (AAA) is a convolution superposition algorithm developed by Varian Medical Systems (Palo Alto, CA, USA) that uses a polyenergetic pencil beam EDK to determine the energy deposited as a function of depth, which is convolved with an analytical model function of the lateral scatter kernel. Tissue heterogeneity is accounted for anisotropically by separating the lateral scatter kernel into angular sectors.

The algorithm is separated into two components: the configuration algorithm and the dose calculation algorithm. In the configuration algorithm, the phase space of the photon beam is determined, based on Monte Carlo simulations of the treatment head and adapted to match a specific treatment unit using beam commissioning measurements including percentage depth dose curves, in-plane, cross-plane, and diagonal field profiles, and field output factors under a variety of measurement conditions.

The dose calculation component is separated into three sources: (i) primary photon energy fluence, for bremsstrahlung photons produced in the linear accelerator target; (ii) extra-focal photon energy fluence, for photons that interact in the treatment head; and (iii) contaminant electron fluence, for electrons produced in the treatment head and in air. The configuration algorithm modifies the characteristics of these sources, such as the energy fluence as a function of beamlet position. Dose is calculated separately for each source, and summed to obtain a final dose distribution.

AAA dose calculations have demonstrated good agreement under most clinical scenarios, but have shown discrepancies in the build-up region, in small fields, and in the presence of tissue heterogeneities [27–30].

Collapsed Cone Convolution

The use of a point spread kernel rather than a line spread kernel can result in improved dosimetric accuracy at the expense of computational efficiency. The collapsed cone approach minimizes the detriment of using a point spread-based convolution by discretizing the point spread EDKs into solid angle cones, with the energy propagated along the cone axes. The point spread kernel is modeled analytically as a sum of exponential functions separating the primary photon energy deposition and the scatter contribution, enabling further efficiency gains through recursion

as the energy is propagated along the cone axes. Collapsed cone-convolution superposition dose calculations have shown improved performance compared to AAA dose calculations when benchmarked against Monte Carlo dose calculations for patient cases [31, 32].

2.4 Patient-Specific Quality Assurance

Due to the complex dose distributions in modern radiotherapy treatment planning, the verification of treatment plan dose calculations through physical measurement is an important clinical process. Discrepancies between the planned and delivered doses may arise due to factors such as the implementation of heterogeneity corrections or the modeling of the MLC, or be related to the physical aspects of the radiation delivery, such as positioning errors of the linear accelerator components (*e.g.* MLC leaves, gantry rotation angle), or the beam characteristics (*e.g.* flatness, symmetry).

The verification of calculated treatment plans can be performed through a patient-specific (or plan-specific) quality assurance protocol, and often combines a point measurement of absolute dose with relative planar dose measurements to evaluate the spatial properties of the dose distribution [33].

For planar dose distributions, determining if the dose is within clinically relevant limits requires an evaluation of both the spatial and dosimetric properties of the dose distribution, and can be represented by the distance-to-agreement (DTA) and dose difference (DD%) quantities, respectively. For each point in the reference distribution, the DTA is defined as the distance to the equivalent dose in the evaluated distribution, and is useful for evaluating the spatial alignment of high dose gradients. DD% is the numerical difference between the reference distribution and evaluated distribution, often normalized to the global dose maximum, and is suitable for evaluations in low dose gradient regions. To evaluate both the spatial and dosimetric components of a planar dose distribution simultaneously, the gamma index was defined [24, 34]:

$$\gamma = \sqrt{\left(\frac{DTA}{\Delta DTA}\right)^2 + \left(\frac{DD}{\Delta DD}\right)^2} \tag{2.2}$$

where ΔDTA and ΔDD are the evaluation criteria, suggested as 2 mm and 3%, respectively, by the AAPM Task Group 218 [33]. A point in the reference distribution is said to pass the gamma test if the gamma index is less than 1, and the percentage of passing points for the entire dose plane indicates the acceptability of the comparison, with an average acceptance expected of approximately 90% [35]. The AAPM TG-218 report suggests a tolerance limit of 95%, above

which the delivery is said to be operating normally, and an action limit of 90%, above which it is recommended to assess aspects of the delivery for errors. The use of a threshold dose of 10% of the maximum dose is recommended to exclude low dose regions.

In clinical practice, ionization chambers may be used as absolute point dosimeters in conjunction with radiochromic film to evaluate the planar relative dose distribution, but other patient-specific quality assurance techniques exist, such as planar or three-dimensional arrays of ionization chambers or diodes that provide both an absolute dose and spatial measurement of the dose distribution [33].

2.5 Conclusion

In this chapter, aspects of clinical dosimetry were presented. It was explained how dose calculations have been developed to approximate the physical processes that occur when a photon beam is directed into matter, and are used to evaluate the clinical acceptability of a treatment plan. These dose calculations must be verified with comparisons to physical dose measurements, and for treatment planning, quality assurance procedures have been developed to confirm the calculation accuracy. In this thesis, collapsed cone-convolution superposition dose calculations are used during the treatment planning process, with final treatment plan dose calculations performed with Eclipse AAA (Chapter 5) and Monte Carlo (Chapter 6). In Chapter 7, patient-specific quality assurance protocols are followed to evaluate the agreement between Monte Carlo dose calculations and measurements with ionization chamber and radiochromic film.

3

Optimization methods in radiotherapy

Preface

Radiotherapy treatment plan optimization has been a well-studied topic over the past 30 years, with technological advances and improved computer infrastructure enabling increasingly sophisticated delivery techniques and associated optimization implementations. In this chapter, a background to mathematical optimization is first presented, and followed by an overview of optimization in radiation therapy. Importantly for the research presented in this thesis, the column generation approach for treatment plan optimization is outlined.

3.1 Nonlinear Programming

3.1.1 Optimization Basic Definitions

Mathematical optimization (or mathematical programming) entails the determination of an optimal set of input variables, subject to constraints, in order to maximize or minimize the value of a real

function. The general formulation of a nonlinear programming problem is given as:

$$\text{minimize: } f(\boldsymbol{x}) \tag{3.1}$$

$$\text{subject to: } g_i(\boldsymbol{x}) \leq 0, \qquad i = 1,\ldots,m \tag{3.2}$$

$$h_j(\boldsymbol{x}) = 0, \qquad j = 1,\ldots,p \tag{3.3}$$

$$\boldsymbol{x} \in X \tag{3.4}$$

where $f : \mathbb{R}^n \to \mathbb{R}$ is the objective function encoding the optimization criteria, $g_i(\boldsymbol{x})$ for $i = 1,\ldots,m$ are the inequality constraints, $h_j(\boldsymbol{x})$ for $j = 1,\ldots,p$ are the equality constraints, and $\boldsymbol{x}$ is a vector of input values in the domain X, which itself is a subset of $\mathbb{R}^n$. If $\boldsymbol{x}$ satisfies all the constraints, then it is a feasible solution to the optimization problem, and the set of all feasible solutions defines the feasible region. The purpose of optimization is to determine an input vector $\boldsymbol{x}^*$ such that $f(\boldsymbol{x}) \geq f(\boldsymbol{x}^*)$ for each feasible point $\boldsymbol{x}$. By convention, the objective function is minimized rather than maximized, since the maximization of an objective function (max:$f(\boldsymbol{x})$) can be trivially changed into a minimization problem by negating the objective function (min: $-f(\boldsymbol{x})$) [36].

3.1.2 Convexity

The convexity of an objective function is an important property for optimization problems, enabling improved efficiency in determining the minimum solution. A function is convex over a domain X if $\forall \boldsymbol{x}_1, \boldsymbol{x}_2 \in X$ and $\forall t \in [0,1]$:

$$f(t\boldsymbol{x}_1 + (1-t)\boldsymbol{x}_2) \leq tf(\boldsymbol{x}_1) + (1-t)f(\boldsymbol{x}_2) \tag{3.5}$$

This inequality implies that a function is convex over a domain X if a line joining any two points in X does not intersect the function between those points. The domain X must also be a convex set, that is, $\forall \boldsymbol{x}_1, \boldsymbol{x}_2 \in X$, then $s\boldsymbol{x}_1 + (1-s)\boldsymbol{x}_2 \in X, \forall s \in [0,1]$ [36, 37].

Nonlinear programming refers to optimization problems where the objective function or constraints are nonlinear functions of the input variables $\boldsymbol{x}$. In general, nonlinear optimization problems are not convex over the entire domain, and may feature several local minima [36].

3.1.3 First-Order Conditions for Optimality

To determine if a particular feasible solution $\boldsymbol{x}^*$ to a nonlinear programming optimization problem is a minimum (either local or global), there are a necessary set of conditions called Karush-Kuhn-Tucker (KKT) conditions that must be satisfied:

$$\nabla f(\boldsymbol{x}^*) + \sum_{i=1}^{m} \mu_i \nabla g_i(\boldsymbol{x}^*) + \sum_{j=1}^{l} \lambda_j \nabla h_j(\boldsymbol{x}^*) = \mathbf{0} \tag{3.6}$$

$$g_i(\boldsymbol{x}^*) \leq 0 \text{ for } i = 1, \ldots, m \tag{3.7}$$

$$h_j(\boldsymbol{x}^*) = 0 \text{ for } j = 1, \ldots, p \tag{3.8}$$

$$\mu_i \geq 0 \text{ for } i = 1, \ldots, m \tag{3.9}$$

$$\sum_{i=1}^{m} \mu_i g_i(\boldsymbol{x}^*) = 0 \tag{3.10}$$

with μ_i and λ_j called KKT multipliers. Eq. 3.10 are referred to as complementary slackness conditions, and imply that when an inequality constraint is active ($g_i(\boldsymbol{x}) = 0$), the associated KKT multiplier μ_i can be nonzero, with its magnitude referred to as a "price" indicating the influence of the constraint on the objective function value. If the inequality constraint is not binding ($g_i(\boldsymbol{x})$ is nonzero), then the KKT multiplier μ_i must equal 0 and thus, the associated inequality constraint has no influence on the optimality of the solution. Due to Eq. 3.9, if μ_i is negative, then the solution cannot be an optimum [36, 38].

3.1.4 Optimization Algorithms

The algorithms used to solve optimization problems are often iterative, relying on an initial estimate and exploiting features of the optimization problem to efficiently converge to a solution. For example, the gradient (steepest) descent method evaluates the gradient at an initial solution ($\nabla f(\boldsymbol{x}_0)$), then selects a new evaluation point by taking a "step" in the negative gradient direction ($\boldsymbol{x}_1 = \boldsymbol{x}_0 - t\nabla f(\boldsymbol{x}_0)$, where t is the step size). The iterative algorithm halts when some convergence criteria is satisfied. It is important to note that for nonlinear optimization problems, convergence to a solution is only guaranteed to be a local minimum, and is dependent on the initial guess [38].

Simulated annealing differs from other optimization methods in that it uses a stochastic approach to perturb the current solution to a neighbouring candidate solution. Commonly, if the candidate solution results in a decreased objective function, the perturbation is retained,

but a candidate solution resulting in an increased objective function may also be retained with a probability defined by a cooling schedule. The probability of accepting a worse solution approaches 0 as the number of iterations increases. The objective function is often referred to as the energy of the system, with the solutions called states. Simulated annealing is a heuristic optimization method, but has the advantage of being able to escape local minima due to the probability function [39].

The work in this thesis employs several different optimization methods. An interior-point algorithm is used as a general-purpose optimization algorithm to determine treatment plan weights (MU) for predetermined aperture dose distributions based on the minimization of an objective function [40]. The column generation approach is used as a heuristic to formulate a restricted (and more computationally manageable) optimization problem. A stochastic simulated annealing approach is also used to modify treatment plan parameters to avoid local minima. The column generation approach and simulated annealing will be discussed later in this chapter in the context of radiotherapy treatment planning.

3.2 Treatment Plan Optimization

3.2.1 Initial Plan Parameters

Prior to treatment plan optimization, several predefined features of the treatment delivery are decided upon, including the energy and orientation of the radiation beams, the location of the target volume and critical structures in the voxelized patient CT data, and the location of the treatment isocentre. For beamlet-based optimizations, the radiation field is decomposed into a rectangular beamlet grid. Beamlet dose distributions may be precalculated for all beamlets intersecting the target volume, or performed during treatment plan optimization as necessary.

3.2.2 Objective Function

The objective function defined for treatment plan optimization in radiation therapy is dependent on the dose distribution in the patient, and is often comprised of a sum of individual structure-based penalty functions (called planning constraints). These penalty functions may employ biological models (such as the generalized equivalent uniform dose (gEUD), tumour control probability (TCP), or normal tissue complication probability (NTCP)) but typically are dose- or dose-volume based functions [41–43]. The contouring step of the treatment planning process attributes voxels

in the patient to the target volume, critical structures, and other regions of interest. For target volume constraints, lower dose limits are defined to ensure the treatment plan achieves the prescription dose, while upper dose limits can be set to encourage target dose homogeneity or as dose thresholds for critical structures. Hard dose constraints may be defined as piecewise functions with a tolerance dose, with noncompliant voxels incurring a penalty. Dose-volume constraints specify a dose threshold and a fractional volume, requiring a sorted dose array for voxels in that structure to identify the noncompliant voxels to be penalized. The penalty for noncompliant voxels may be linear functions of the dose, but more often the squared dose difference is used [44]. A weighting factor is applied to modify the importance of matching a specific dose constraint. In general, dose-volume constraints are nonconvex, but the multiple local minima each tend to yield a similar objective function value, with no substantial difference in the treatment plan quality [45, 46]. Although the planning objectives are referred to as "constraints" in medical physics, these are distinct from the equality and inequality constraints in the general formulation of the optimization problem.

3.2.3 Treatment Plan Optimization Formalism

The general optimization problem in radiation therapy is:

$$\text{minimize: } f(\boldsymbol{z}) \tag{3.11}$$

$$\text{subject to: } z_j = \sum_k y_k D_{kj} \tag{3.12}$$

$$y_k \geq 0 \tag{3.13}$$

The dose distribution $\boldsymbol{z}$ is comprised of a total of $|V|$ voxels, with individual voxel doses indexed by $j \in V$. For each beamlet dose k (or aperture dose, depending on the optimization approach), the unit dose deposition coefficient for a voxel j is given as D_{kj}, and is multiplied by the (non-negative) optimization weight y_k associated with that beamlet. The optimization weights are related to the monitor unit output for the deliverable treatment plan, and the conversion can be calibrated through measurement.

The objective function itself can be defined as a sum of hard constraints $h_{sm}(\boldsymbol{z})$ and dose-volume constraints $g_{sn}(\boldsymbol{z})$ for each structure s in the set of all optimization structures S, where $m, n \geq 0$ (note that these constraints are not related to those of the general nonlinear programming problem definition in section 3.1.1). Weighting factors (w) are chosen by the planner based on the importance of the constraint to the optimization problem. The set of voxels for each structure

are denoted as V_s. Each constraint either specifies a lower limit ($-$) or an upper limit ($+$). For quadratic objective functions, hard constraints based on a dose threshold D^{thr} are given as:

$$h^{+}_{sm}(\boldsymbol{z}) = w_m \sum_{j \in V_s} \begin{cases} 0 & z_j \leq D^{thr}_m \\ (z_j - D^{thr}_m)^2 & z_j > D^{thr}_m \end{cases} \tag{3.14}$$

$$h^{-}_{sm}(\boldsymbol{z}) = w_m \sum_{j \in V_s} \begin{cases} (z_j - D^{thr}_m)^2 & z_j < D^{thr}_m \\ 0 & z_j \geq D^{thr}_m \end{cases} \tag{3.15}$$

To evaluate dose-volume constraints, the structure voxels must be sorted by their associated dose in ascending order, denoted as $\widetilde{V}_s$. For a threshold dose D^{thr} and fractional volume v, an upper limit dose-volume constraint can be described as: "no more than fractional volume v of the structure can contain D^{thr}", while lower limit dose-volume constraints can be described as "at least fractional volume v of the structure must contain D^{thr}". The penalization of dose-volume constraints is given as:

$$g^{+}_{sn}(\boldsymbol{z}) = w_n \sum_{j \in \widetilde{V}_s} \begin{cases} 0 & z_j \leq D^{thr}_n \\ (z_j - D^{thr}_n)^2 & z_j > D^{thr}_n \end{cases} \quad \text{for: } j < (1 - v_n)|\widetilde{V}_s| \tag{3.16}$$

$$g^{-}_{sn}(\boldsymbol{z}) = w_n \sum_{j \in \widetilde{V}_s} \begin{cases} (z_j - D^{thr}_n)^2 & z_j < D^{thr}_n \\ 0 & z_j \geq D^{thr}_n \end{cases} \quad \text{for: } j > (1 - v_n)|\widetilde{V}_s| \tag{3.17}$$

The objective function is then given as:

$$f(\boldsymbol{z}) = \sum_s \left(\sum_m h_{sm}(\boldsymbol{z}) + \sum_n g_{sn}(\boldsymbol{z}) \right) \tag{3.18}$$

Treatment plan optimization is aided by the use of dose-volume histograms (DVHs) that indicate the cumulative histogram data for each structure in the treatment plan optimization. For a coordinate (X,Y) on the curve of a given structure, the interpretation is "Y% of the structure receives at least X Gy" Planning constraints can be visualized as coordinates on the DVH graph (see Fig. 3.1).

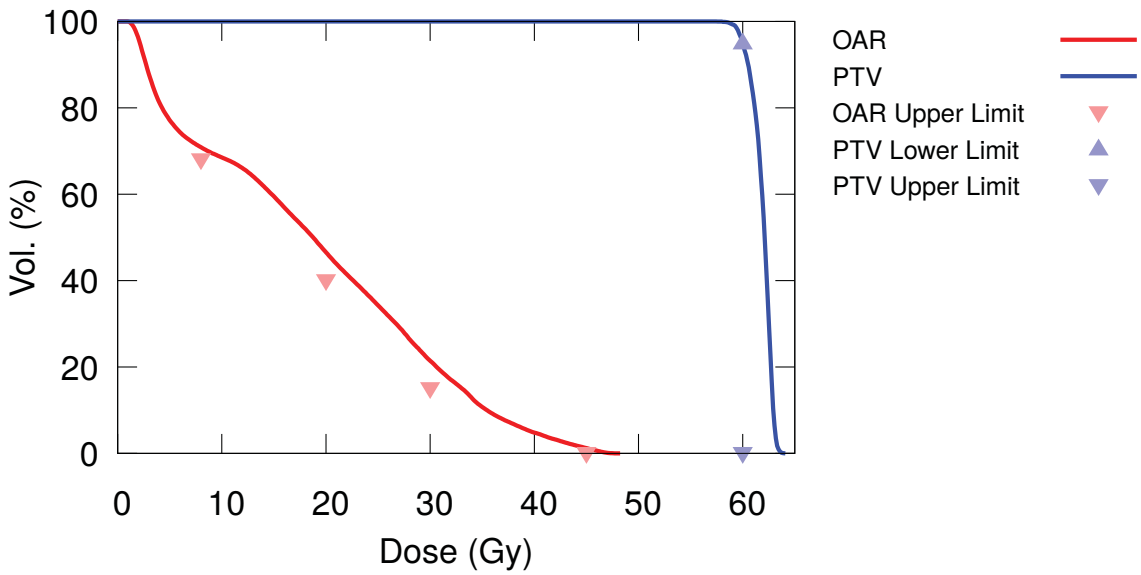

Figure 3.1 Dose-volume histogram illustrating the total structure volume receiving a given dose. Example dose-volume constraints for the OAR and PTV are indicated by triangles, with the triangle orientation indicating lower or upper dose limits.

3.3 Treatment Delivery Modalities

3.3.1 Intensity Modulated Radiation Therapy

With intensity modulated radiation therapy optimization, there are two distinct approaches. The first is fluence map optimization (FMO), where a fluence map is generated for each beam orientation by optimizing the intensity of each individual beamlet. There is a necessary leaf-sequencing step for each beam orientation to generate deliverable MLC-defined apertures to achieve the fluence map intensities, which perturbs the treatment plan quality. This can be performed by discretizing the intensity levels of the fluence map, and then determining a manageable number of single-intensity apertures to deliver the optimized fluence [47–50]. Alternatively, a dynamic MLC delivery can be determined that achieves the optimized fluence map by programming the MLC leaves to sweep across the radiation field [51–53].

The second approach to IMRT optimization is the direct aperture optimization (DAO) method, in which deliverable apertures rather than beamlets are optimized. A novel DAO method was proposed by Shepard *et al.*, and used a simulated annealing optimization approach to randomly adjust the leaf positions and optimization weights for each aperture in the treatment plan [54].

At the start of the optimization, the aperture shapes are initialized to the beam's eye view of the target. DAO methods using other optimization strategies have been presented in the literature, such as using the column generation approach [55].

3.3.2 Volumetric Modulated Arc Therapy

For the optimization of volumetric modulated arc therapy treatment plans, it is convenient to define control points as representations of the state of the linear accelerator throughout the treatment arc. Control points are defined sequentially as functions of the cumulative monitor unit output, and specify the gantry rotation angle, MLC leaf positions, and other components of the linear accelerator. As a result of the arc-based delivery, there is spatial continuity imposed between the MLC aperture shapes at adjacent control points, and restrictions on the maximum delivery time or dose rate may affect the allowed MLC positions. This is commonly achieved by specifying a minimum gantry rotation speed, and using the arclength spacing between adjacent control points and the nominal maximum leaf translation speed to determine the allowed range of leaf motion. In contrast to IMRT, which features many intensity levels from a single beam orientation, VMAT treatment plans deliver a single intensity at each control point [56].

A clinically viable solution for VMAT optimization was introduced by Otto in 2007, and was later adopted as the RapidArc treatment planning approach (Varian Medical Systems, Palo Alto, CA, USA). The optimization approach is based on simulated annealing, stochastically altering the MLC leaf positions and aperture weights during the optimization, but manages the number of active variables by implementing a progressively increasing sampling of the control point spacing along the arc. When the optimization starts, a small number of equally-spaced control points around the treatment arc are initialized to have their apertures match the beam's eye view of the target. Once the simulated annealing step converges, control points are inserted between the existing control points, with their aperture shapes linearly interpolated between its adjacent neighbours, following which the simulated annealing step restarts. This process continues until a control point spacing of approximately 2° per control point is achieved [17].

Other VMAT optimization techniques were developed analogously to the FMO approach in IMRT. For a set of beam orientations equally spaced along an arc, an FMO solution is calculated and followed by an arc-sequencing step [57]. In some implementations, the arc-sequenced delivery is used as the initial solution to a direct aperture optimization step using a gradient-based optimization to modify the leaf positions [58, 59]. The column generation approach has also been applied for VMAT optimization [60, 61].

3.4 Column Generation

The column generation approach is an optimization heuristic that is well-suited for large-scale programming problems when a large number of the variables are presumed to be near zero. For radiation therapy treatment plan optimization, the number of possible aperture shapes has been estimated to be on the order of 10^{17}, but it is hypothesized that a more manageable subset of apertures can yield a near-optimal solution. The column generation approach for treatment plan optimization has been applied for both IMRT and VMAT delivery [55, 60–62]. This section will first introduce the IMRT optimization methodology, and then discuss additional restrictions imposed for VMAT optimization.

For an IMRT optimization, there are a number of predefined beam orientations, each with an associated grid of beamlets. As indicated in an earlier section, the optimization problem is defined as:

$$\text{minimize: } f(\boldsymbol{z}) \tag{3.19}$$

$$\text{subject to: } z_j = \sum_k y_k D_{kj} \tag{3.20}$$

$$y_k \geq 0 \tag{3.21}$$

In this case, the D_{kj} refer to the voxel-based dose deposition coefficient for an aperture k. Let the beamlets forming an aperture k belong to the set A_k, then the aperture dose D_{kj} can be further decomposed into individual beamlet dose deposition coefficients:

$$D_{kj} = \sum_i^{|A_k|} D_{ij} \tag{3.22}$$

The master problem (MP) is formulated as the optimization of all possible aperture shapes that can be constructed given the initial treatment plan parameters. The restricted master problem (RMP) is formulated as the optimization of an aperture subset $\hat{K} \in K$, and the column generation approach provides a methodology to select "good" apertures to add to the RMP.

Evaluating the KKT conditions for the treatment plan optimization yields:

$$\lambda_j = \frac{\partial f}{\partial z_j} \qquad j = 1, \ldots, |V| \tag{3.23}$$

$$\mu_k = \sum_j^{|V|} \sum_i^{A_k} D_{ij} \lambda_j \qquad k \in K \tag{3.24}$$

$$y_k \geq 0 \qquad k \in K \tag{3.25}$$

$$z_j = \sum_k^{|A_k|} \sum_i y_k D_{ij} \qquad j = 1, \ldots, |V| \tag{3.26}$$

$$\mu_k \geq 0 \qquad k \in K \tag{3.27}$$

$$\mu_k y_k = 0 \qquad k \in K \tag{3.28}$$

where the KKT multipliers are λ_j (corresponding to the equality constraints) and μ_k (corresponding to the inequality constraints). To determine if a minimum solution to the RMP is also a minimum of the MP, the KKT conditions must be satisfied. In formulating the RMP, for all $k \notin \hat{K}$, the optimization weights y_k are implicitly set to zero, but in general, these weights are not guaranteed to be zero for the optimization of the MP. As a result, the RMP solution cannot satisfy the complementary slackness condition for the MP (Eq. 3.28) if y_k and the corresponding μ_k are both nonzero. This property provides a strategy to iteratively add apertures into $\hat{K}$ of the RMP; the μ_k are referred to as prices, and the magnitude of the price associated with an aperture indicates the benefit of adding that aperture to the RMP. This subproblem is known as the "pricing problem".

Combining Eq. 3.23 and Eq. 3.24, the price of an individual beamlet i is given by:

$$\mu_i = \sum_j^{|V|} D_{ij} \frac{\partial f}{\partial z_j} \tag{3.29}$$

Eq. 3.27 indicates that a solution can be optimal with a positive price, as long as the corresponding y_k is equal to zero. However, if μ_k is negative, then this indicates that the solution is not optimal, and the objective function of the MP will be further minimized with the inclusion of the associated aperture k. This property provides the basis for the "pricing problem", in which beamlet prices are evaluated to construct an aperture on a row-by-row basis, corresponding to the translational motion of the MLC leaves. Respecting physical leaf constraints (namely that the left leaf boundary cannot overlap the right leaf boundary), the sequence of open beamlets with the largest negative price can be determined for each row (or if no beamlets exist with a negative price,

the leaf pairs are closed). After determining the open beamlet sequence for each row to select the beamlets in A_k, the resulting candidate aperture price can be calculated as: $\mu_k = \sum_i \mu_i, \forall i \in A_k$.

The strategy for adding candidate apertures to $\hat{K}$ varies depending on the implementation, but commonly the candidate apertures for each beam orientation are ranked according to their price, and the single highest ranking aperture (largest negative price) is added to the RMP [62].

The main iterative loop for the column generation optimization is as follows:

1. Evaluate the RMP for apertures $\hat{K}$, determining optimization weights y_k. The optimal dose distribution $\boldsymbol{z}$ for the RMP is calculated.
2. For each beam orientation, solve the pricing problem to determine new candidate apertures.
3. Add the best aperture to $\hat{K}$.
4. Go to 1.

It is important to note that with each iteration, the optimization of the RMP results in an updated dose distribution, and the apertures that are constructed by the pricing problem will be based on improving this dose distribution with respect to the objective function. For IMRT, the optimization is halted when either there are no apertures that can be constructed with a negative price, or when a user-specified number of apertures is reached.

The implementation of column generation for VMAT treatment plan optimization imposes further restrictions due to the arc-based delivery. The treatment arc is predetermined and arranged into a sequence of predefined control points. For VMAT treatment delivery, only a single aperture shape can be specified per control point. Modern linear accelerators have the ability to deliver a variable dose rate, but setting a maximum treatment delivery time enforces restrictions on the allowed leaf positions for a control point due to the aperture shapes at adjacent control points [61]. In general, VMAT optimization can be applied to any arc-based deliveries, including noncoplanar trajectories that include gantry and couch rotation.

3.5 Conclusion

The culmination of the topics presented in this chapter is the description of the column generation approach for treatment plan optimization, which plays an important role throughout this thesis work. In the application to radiotherapy treatment planning, the column generation approach relies on the Karush-Kuhn-Tucker conditions for optimality to define a method to generate a

treatment plan through the iterative addition of apertures constructed through the pricing problem. The VMAT implementation of the column generation approach is used to optimize treatment plans in Chapters 5 and 8, while a novel application of the column generation approach is used to implement a trajectory-based optimization methodology in Chapter 6.

4

Review of Trajectory-based Treatment Planning

Preface

Trajectory-based delivery refers to the coordinated motion of the mechanical components of the linear accelerator with arc-based radiation delivery. The coordinated mechanical components can include a combination of couch rotation, couch translation, and collimator rotation, in addition to features of conventional arc-based treatment such as gantry rotation and MLC leaf motion. The introduction of the Varian TrueBeam linear accelerator (Varian Medical Systems, Palo Alto, CA, USA) and its optional research mode provided the capability for user-defined trajectories to be delivered in a non-clinical context, spurring recent interest into investigations and implementations into trajectory-based radiotherapy. This chapter introduces early research involving the potential of dynamic trajectories prior to the TrueBeam linear accelerator, and then presents the current state of trajectory-based treatment planning research.

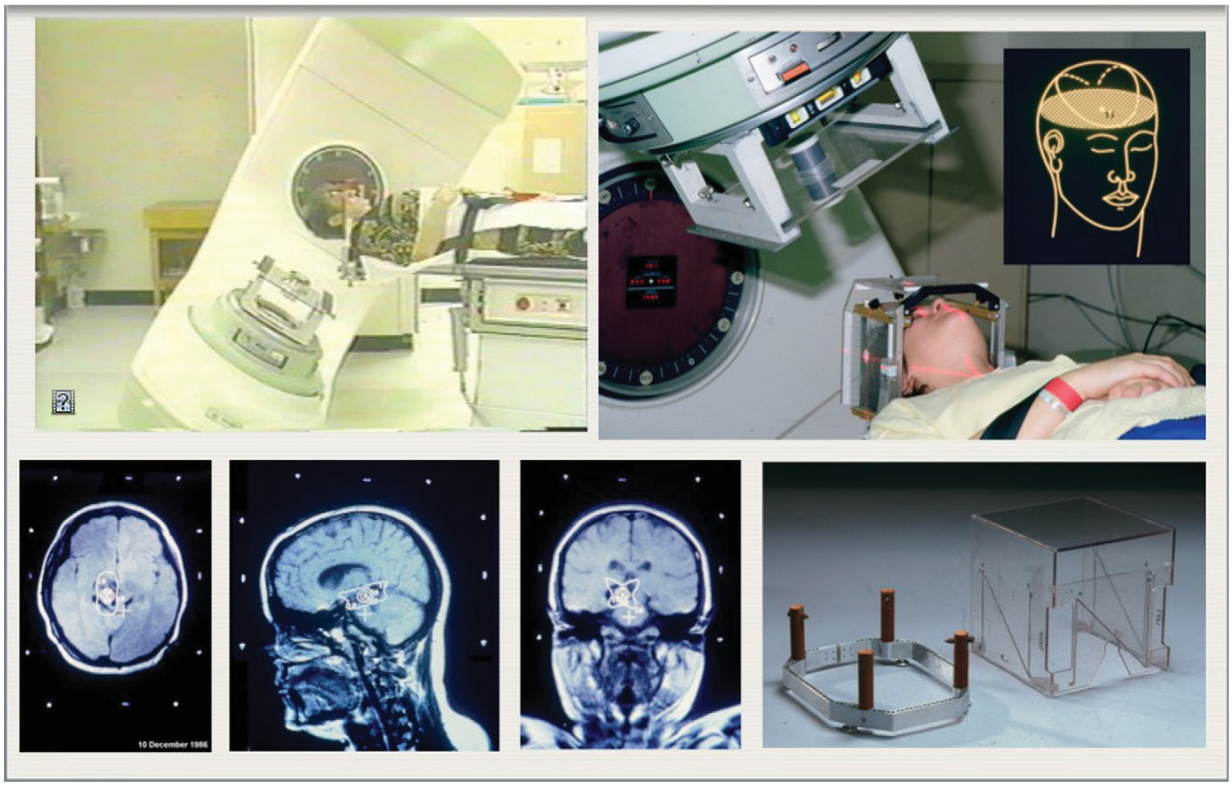

Figure 4.1 The dynamic stereotactic radiosurgery technique traces a “baseball-stitch” pattern on the patient anatomy. Reproduced from ICRU Report 91 [7].

4.1 Early Research

4.1.1 Dynamic Stereotactic Radiosurgery

An early treatment involving coordinated dynamic couch and gantry motion was demonstrated with the dynamic stereotactic radiosurgery treatment technique by Podgorsak *et al.* [63]. A trajectory was defined that combined a 150° gantry rotation with a simultaneous 75° couch rotation, resulting in a “baseball stitch” pattern when applied to patients with cranial targets (see Fig. 4.1). This trajectory path was applied for stereotactic radiosurgery, where the steeper dose falloff due to the noncoplanar beam arrangement is desired for high dose fractionation. The treatment was aided by a stereotactic frame for target determination, treatment setup, and patient immobilization, as well as fixed circular collimators to define the radiation field.

4.1.2 Accelerated Partial Breast Irradiation

The benefit from incorporating couch motion into arc-based treatment delivery was hypothesized for accelerated partial breast irradiation (APBI), in which a partial breast volume is irradiated following surgical lumpectomy over a short timespan, in contrast to the whole breast irradiation approach. Research performed by Shaitelman *et al.* demonstrated improved OAR sparing without compromising target coverage through an arrangement of fields spaced at 10° couch rotation intervals and optimized with an IMRT technique to simulate arc-based treatment [64]. Fahimian *et al.* developed arc-based delivery with couch rotation and translation to ensure a wide-angular irradiation while maintaining the target volume within the MLC apertures. The plan optimization involved subsampling the trajectory into 40 delivery points upon which a dynamic MLC IMRT optimization was instantiated [65]. Although these methods involved a static gantry rotation angle, the delivery of couch-arc treatments had previously not been investigated.

The research performed by Popescu *et al.* combined simultaneous couch and gantry rotation in their approach towards APBI treatment. Based on trial and error, they determined a series of couch arcs combined with a maximum gantry rotation of 20° for each arc. Plan optimization involved a series of dynamic IMRT fields with 10° couch angle separation [66].

Although these APBI treatment techniques were based on the implementation of nonconventional arc delivery (either couch rotations or combined gantry/couch rotations during radiation delivery), the optimizations remained approximations of arc treatment optimization using IMRT optimization techniques.

4.2 Trajectory Optimization

4.2.1 Gantry-Couch Trajectories

There have been several investigations into the combination of couch and gantry rotation to define noncoplanar trajectories that can achieve steeper dose gradients outside the target volume and sparing of critical structures. The nonconvex nature of the trajectory optimization problem necessitates the use of heuristic methods to generate a viable treatment plan [67]. The optimization strategies presented in the literature have followed either a two-step approach, where the trajectory is determined independently from the VMAT optimization, or iterative approaches, where determination of the trajectory path is informed using dosimetric data.

Two-Step Trajectory Optimization

The heuristics used to determined the trajectory path can be broadly categorized as: (1) cost map/geometry approach; (2) travelling salesman; (3) patient-generalized trajectories.

1. **Cost Map**: The geometry of the target volume and critical structures is assessed and assigned a score for each gantry-couch angle combination, representing the benefit of the inclusion of that beam orientation in the treatment plan. Yang *et al.* provided a metric representing the non-overlapping PTV area and the relative overlap with the critical structures from each beam's eye view (BEV) [68]. MacDonald *et al.* expanded on this metric by first including a foreground/background factor that considers the relative position of the target and OAR from the BEV, then in a later publication, amending this factor based on the dose deposition to the patient [69, 70]. Smyth *et al.* defined their geometry scoring through raytracing, including 3D information by tallying the number of OAR voxels intersected by rays originating at the beam source and travelling through the target volume [71]. Fix *et al.* calculated the fractional overlap volume through the use of triangular meshes for each of the OARs and PTV.

   Following generation of the cost map, the gantry-couch trajectory is determined. The method used by Yang *et al.* involved several steps to identify the lowest scoring coordinates, connect these beam orientations into sub-arcs, and then extend into longer trajectories. The score map, and resulting trajectories from the approach of Yang *et al.* are shown in Fig. 4.2. MacDonald *et al.* similarly identified low-scoring beam orientations, but connected them into 10 sub-arcs, each with a static couch position, in order to comply with restrictions for optimization in the Eclipse treatment planning system.

   Alternatively, the work performed by Smyth *et al.* and Fix *et al.* relied on pathfinding algorithms (Dijkstra's algorithm [72], A* algorithm [73]) to identify the shortest path through the gantry-couch coordinate space, with the cost map score defining the distance between adjacent nodes.

2. **Travelling Salesman**: This methodology relies on beam angle optimization literature to identify a set of favorable beam orientations on which the trajectory is based. The beam orientations define anchor points as an instance of the travelling salesman problem. The shortest angular path that traverses each of the anchor points defines the gantry-couch trajectory. The BAO method used by Papp *et al.* evaluated the quality of the potential beam orientation based on the gradient of the objective function for the beam [74], while Wild *et*

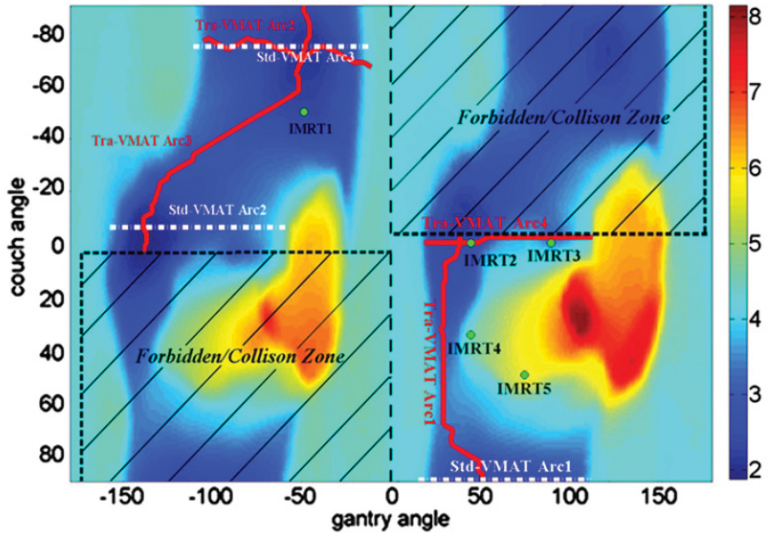

Figure 4.2 Example of the cost map approach for gantry-couch trajectory optimization. The selected trajectories are shown as red lines. Forbidden zones were categorically outlined based on the quadrant of the gantry-couch coordinate system. Reproduced from Yang *et al.* [68].

al. used a genetic algorithm to identify the set of beam orientations [75]. An example of the trajectory determined using the travelling salesman approach of Wild *et al.* is shown in Fig. 4.3.

The research performed by Langhans *et al.* used a hybrid approach, combining the travelling salesman and cost map methods. To identify the anchor points, they first computed a 4π IMRT solution to the optimization problem, comprised of up to 600 apertures distributed at beam orientations covering the entire 4π solid angle of a sphere, then iteratively reduced the number of included beams based on their total fluence until a maximum of 20 beams remained. Next, a cost map was calculated with the score accounting for (1) conformity of the dose deposition to the PTV boundaries; (2) patient geometry, similar to Yang *et al.*; (3) integral dose score that provides for the cumulative dose delivered to the patient along the beam path. For each possible pair of beam orientations in the BAO set, the cost map was used to determine the shortest connecting path. Finally, the trajectory was determined as an instance of the travelling salesman problem based on these computed cost map distances between the nodes [67].

3. **Patient-Generalized**: The presentation of the target disease in the patient anatomy provides the possibility to define a patient-generalized trajectory, independent of the specific patient

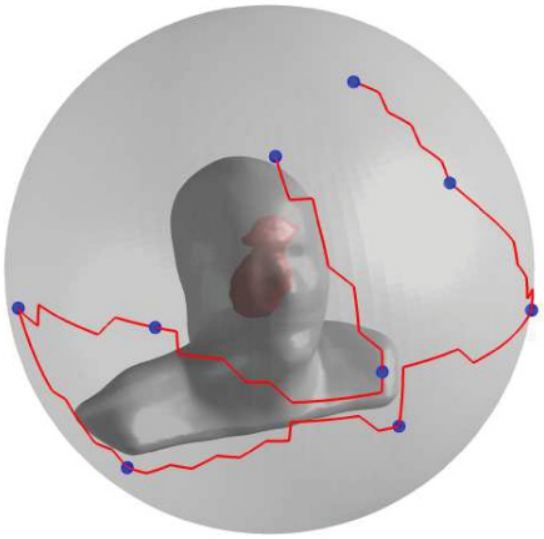

Figure 4.3 Example of the travelling salesman approach. Anchor points were determined using beam angle optimization (blue points), and the shortest path connecting the anchor points was determined using a genetic algorithm (red lines). Reproduced from Wild *et al.* [75].

anatomy, that adequately samples the angular solution space to generate a clinically viable treatment plan. An early approach by Krayenbuehl *et al.* involved a 360° gantry rotation separated into 8 segments with couch rotations between ±5 - 15°, and applied to patients with head-and-neck cancer, although the plan optimization involved 16 static IMRT fields to approximate arc-based delivery [76]. The previously mentioned research by Popescu *et al.* for accelerated partial breast irradiation provides another example of a patient-generalized approach [66]. More recently, Wilson *et al.* extended the concept of the baseball stitch trajectory to include a variable number of gantry sub-arcs combined with a monotonically increasing couch rotation, and applied the generalized trajectory to patients presented with cranial targets. An example of the patient-generalized trajectories employed by Wilson *et al.* is shown in Fig. 4.4. In their research, they investigated the compromise between plan quality and treatment delivery time based on the number of gantry sub-arcs in the patient-generalized trajectory [77].

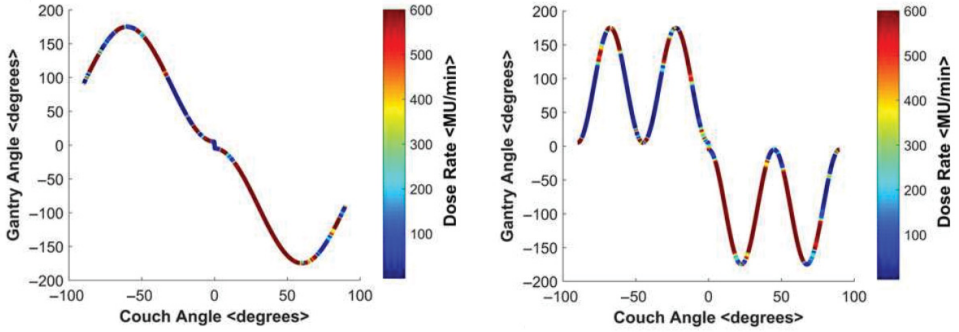

Figure 4.4 Patient-generalized trajectories for cranial targets. The number of gantry sub-arcs is set manually through a parameter N, with $N = 3$ for the left image, and $N = 8$ for the right image. Reproduced from Wilson *et al.*[77].

4.2.2 Iterative Approaches

There exists trajectory-based optimization algorithms in the literature that actively use dosimetric information during the trajectory-VMAT optimization to make adjustments to the trajectory path, and can be considered distinct from the two-step approaches mentioned previously.

Smyth *et al.* developed an algorithm based on a local fluence-based search to modify a trajectory obtained with a geometry cost map heuristic. The trajectory obtained from the cost-map approach was downsampled into a 15 field IMRT plan, and the effect of incremental changes to the couch rotation angle for each of the 15 beam orientations on the objective functions was measured in an iterative process, retaining any changes that improved the objective function. The repositioned IMRT fields were incorporated into the original trajectory to finalize the trajectory and VMAT plan optimization [78].

Lyu *et al.* developed an iterative algorithm that alternated between a direct aperture optimization step and a beam trajectory selection step. During the DAO, the 4π angular space was reduced to a limited number of feasible beam orientations, which was used as a cost map for the beam trajectory selection step to determine a shortest path trajectory. This trajectory was used as prior knowledge for the next iteration of DAO, heavily penalizing beam orientations not found on that trajectory. The optimization was found to converge to a final trajectory-based treatment plan [79].

Dong *et al.* performed a similar iterative approach in which the trajectory-based treatment plan at the conclusion of one iteration was used to guide the trajectory selection in future iterations. The trajectory path was determined with a Monte Carlo tree search, where the probability of extending a trajectory to a given beam orientation was based on a continuously updating average

objective function value for that beam orientation node. Over many iterations, the trajectory optimization would converge to a final trajectory-based treatment plan [80].

4.2.3 Collimator Trajectories

In addition to dynamic gantry-couch trajectories, there has been interest in employing dynamic collimator rotation during arc-based delivery. The orientation of the MLC leaves with the target volume may result in reduced dose to OARs and improved conformity. Zhang *et al.* performed principal component analysis to determine the primary lengthwise orientation of the target volume to align the direction of multileaf collimator leaf travel along that direction, while respecting collimator rotation speed restrictions during the treatment [81]. MacDonald *et al.* performed a cost map approach, where each collimator and gantry angle combination was given a "whitespace" score that represented the ability of the MLC to shield healthy tissue and irradiate the target volume. The gantry-collimator trajectory was determined based on a bidirectional gradient search [82]. Fix *et al.* followed the whitespace methodology, but instead used an A* shortest path algorithm to determine the gantry-collimator trajectory [83].

4.3 Clinical Implementation

The implementation of trajectory-based delivery in a clinical context requires validation of the optimization algorithms used to generate treatment plans, as well as the demonstration of safe and accurate radiation delivery.

4.3.1 Algorithm Validation

Planning Comparison

The purported benefits of noncoplanar delivery through gantry-couch trajectories include steep dose gradients outside the target volume and the avoidance of critical structures. Thus, in the literature, the justification for trajectory-based algorithms have often included comparisons to clinical treatment plans or conventional radiotherapy representing the standard of care through dosimetric criteria such as: gradient indices, mean and maximum dose to OARs, and specific dose-response endpoints. Other considerations in evaluating treatment plans may include delivery time or cumulative MU output that also impacts the clinical viability of a treatment plan. There are a wide variety of treatment sites and therapeutic objectives that have commonly been investigated

Table 4.1 Gantry-couch trajectory-based optimization methodologies and plan comparisons.

Reference		Treatment Sites (number of patients)	Plan Comparison
Yang *et al.* 2010	[68]	head and neck (10)	coplanar VMAT, IMRT
Smyth *et al.* 2013	[71]	partial breast (1), brain (1), prostate (1), prostate and pelvic nodes (1)	coplanar VMAT
MacDonald *et al.* 2015	[69]	brain (30)	VMAT with noncoplanar arcs
Papp *et al.* 2015	[74]	lung (1), brain (1)	4π IMRT (ideal), coplanar IMRT, noncoplanar IMRT, coplanar VMAT
Wild *et al.* 2015	[75]	head and neck (3)	4π IMRT (ideal), coplanar IMRT, noncoplanar IMRT, coplanar VMAT, noncoplanar VMAT, other
Smyth *et al.* 2016	[78]	brain (15)	coplanar VMAT
Wilson *et al.* 2017	[77]	brain (10)	dynamic conformal arc, VMAT with noncoplanar arcs
Fix *et al.* 2018	[83]	head and neck (2), lung (1), esophagus (1), prostate (1)	coplanar VMAT
Langhans *et al.* 2018	[67]	lung (1), brain (1), liver (1)	4π IMRT (ideal), noncoplanar IMRT, coplanar VMAT, trajectory VMAT
Lyu *et al.* 2018	[79]	brain (3), lung (3), prostate (3)	coplanar VMAT
Dong *et al.* 2018	[80]	chest wall (1), brain (1)	coplanar VMAT

as beneficiaries of non-coplanar delivery. Target volumes in the head-and-neck region provide additional collision-free beam orientations superior to the patient. Due to the dose fractionation for stereotactic treatments, the steeper dose gradients outside the target volume with non-coplanar delivery can reduce the dose to normal tissue [18]. Table 4.1 lists the treatment sites investigated and the treatment plan comparisons for each trajectory-based VMAT methodology.

Optimization Comparison

An alternate means of comparing trajectory-based optimization techniques independent of dosimetric comparisons involves using the objective function to evaluate the adherence to the treatment planning constraints. The algorithm validation performed by Papp *et al.*, Wild *et al.*, and Langhans *et al.* included the optimization of a 4π IMRT plan comprised of a large number of fields that represented an upper limit for the plan quality based on the user-defined treatment planning constraints, providing contextual information in evaluating the trajectory-based optimization and other treatment delivery techniques based on their respective objective function value.

4.3.2 Treatment Plan Delivery

Trajectory-based treatment plans involving motion of the patient couch introduces an additional dynamic component to the treatment delivery compared to conventional VMAT plans, necessitating the validation of the radiation delivery accuracy as well as the patient safety and comfort prior to clinical implementation. Specific concerns include: collisions between patient/couch and gantry; positional uncertainty of the mechanical axes during the trajectory, especially with changes in the rotation direction for the couch; patient comfort during dynamic couch motion. The dynamic stereotactic radiosurgery technique employed stereotactic frames affixed to the patient, but less invasive immobilization methods such as thermoplastic masks are desirable.

The approaches to defining restricted gantry-couch-patient collision zones have included: predefined collision indicator charts [74, 67, 80], broad exclusion of potential collision regions [68, 71, 77, 78], physical assessment of collisions with the linear accelerator and a phantom situated on the treatment couch [69], or three-dimensional modelling of the patient, couch, and gantry to probe for invalid gantry-couch angle combinations [79, 83].

The dose delivery accuracy and positional accuracy of the mechanical axes has been investigated in the literature. In several studies, a monotonically increasing couch rotation angle during delivery was enforced to prevent inertial forces from acting on the patient, affecting both patient comfort and the accuracy of the dose delivery [77, 79]. The work of Wilson *et al.* evaluated the delivery accuracy for trajectory-based delivery through dose measurements, with radiochromic film gamma index pass rates (criteria: 2 mm, 2%) greater than 96%, and point dose ionization chamber measurements within 2%. The APBI approach by Fahimian *et al.* with couch trajectories and a static gantry angle yielded radiochromic film pass rates (3 mm, 3%) of 93%, and ionization chamber agreement of -2.4%. Quality control procedures were developed to evaluate the couch positional accuracy during dynamic trajectories with radiographic film or electronic portal imaging measurements, resulting in couch translational accuracy within 0.06 cm for dynamic tracking of a target [84]. Finally, trajectory log files that record the position of the dynamic linear accelerator axes during delivery have been analyzed for their agreement with the planned positions, yielding translational couch positional accuracy within 1 mm (root mean square error) [85], and both gantry and couch rotation accuracy on the order of 0.05° [77]. When considered collectively, these studies indicate that trajectory-based delivery can be a viable clinical option for accurate treatment, but these evaluations have only been performed in controlled conditions on simple trajectories.

Patient comfort during trajectory-based delivery with dynamic couch rotation remains a concern for the clinical viability. In a phase I trial involving 4π static beam IMRT treatments,

dynamic couch rotation and translation was programmed in between radiation delivery at different beam orientations, with the patients reporting the motion as "well-tolerated" through a survey following treatment. Further evaluations of patient comfort during trajectory-based treatment delivery are prohibitive without approval of regulatory organizations (such as the Food and Drug Administration of the United States of America) [86].

4.4 Conclusion and overview of thesis

The research presented in this thesis addresses unexplored aspects of trajectory delivery, with a focus on gantry-couch trajectories. The conventions for the gantry-couch coordinate system used throughout this thesis are illustrated in Fig. 4.5. Chapter 5 investigates the use of translational couch motion to reduce the effective treatment distance and the associated benefits, which has not been explored beyond their application to APBI treatments. In Chapter 6, a novel gantry-couch trajectory optimization algorithm is developed and implemented that addresses limitations of the two-step optimization approaches by simultaneously constructing the trajectory path during the VMAT treatment plan optimization. The dose delivery accuracy for complex gantry-couch trajectories is assessed in Chapter 7, as well as the implementation of a trajectory smoothing procedure. The research presented in Chapter 8 investigates the consequences of the conventional gantry-couch coordinate system that unevenly samples the angular space compared to a spherical coordinate system.

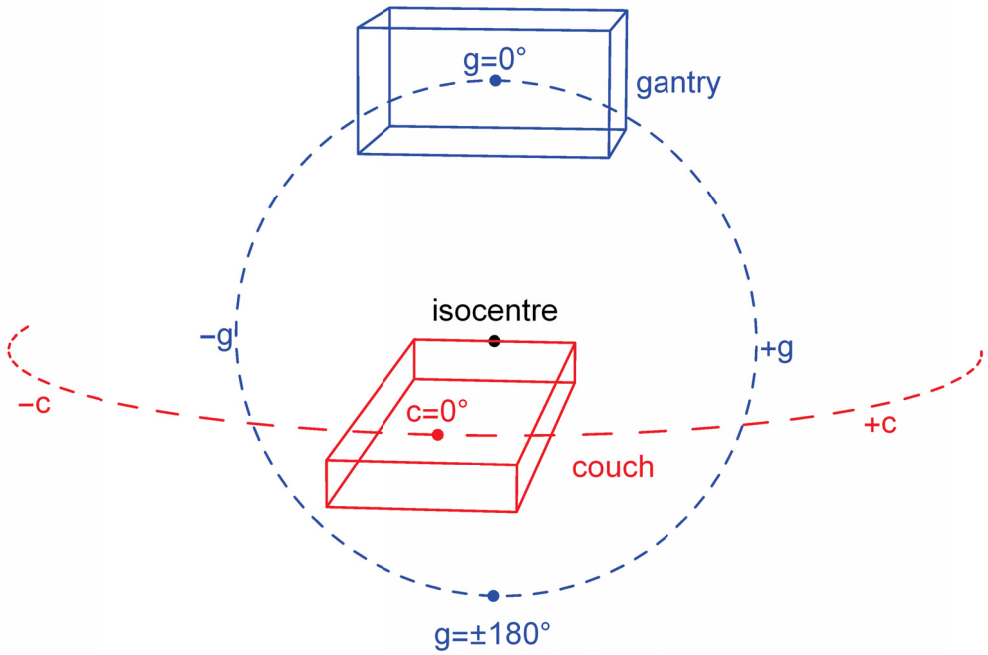

Figure 4.5 Coordinate system defining the gantry and couch rotations around the isocentre. The 0° gantry coordinate is vertically above the treatment isocentre, and the gantry can rotate 180° in either direction. The 0° coordinate for the treatment couch is positioned such that longitudinal motion of the couch is orthogonal to the rotation plane of the gantry. The allowed angle range for the treatment couch is ±90°.

5

Trajectory-based VMAT for cranial targets with delivery at shortened SAD

Joel Mullins, Marc-André Renaud, Veng Heng, Russell Ruo, François DeBlois, and Jan Seuntjens

Article published in: *Medical Physics, vol. 47, pp. 3103-3112, 2020.* [19]

Preface

The initial research performed for this thesis was on the implementation of translational couch motion to reduce the effective treatment distance, which had not been previously investigated in the literature. This approach was based on the perceived benefits of delivery with a reduced projected MLC leaf width for patients presented with cranial targets. The additional collision-free angular space for cranial targets led to the use of a patient-generalized noncoplanar trajectory. As

the research proceeded, the advantages of the increased effective dose rate at a shortened treatment distance and the effect on the treatment delivery time were also observed.

5.1 Abstract

Introduction: Trajectory-based volumetric modulated arc therapy (tr-VMAT) treatment plans enable the option for noncoplanar delivery yielding steeper dose gradients and increased sparing of critical structures compared to conventional treatment plans. The addition of translational couch motion to shorten the effective source-to-axis distance (SAD) may result in improved delivery precision and an increased effective dose rate. In this work, tr-VMAT treatment plans using a noncoplanar "baseball stitch" trajectory were implemented, applied to patients presented with cranial targets, and compared to the clinical treatment plans.

Methods: A treatment planning workflow was implemented: (1) beamlet doses were calculated for control points defined along a baseball stitch trajectory using a collapsed-cone convolution-superposition algorithm; (2) VMAT treatment plans were optimized using the column generation approach; (3) a final dose distribution was calculated in Varian Eclipse using the anisotropic analytical algorithm by importing the optimized treatment plan parameters. Tr-VMAT plans were optimized for ten patients presented with cranial targets at both standard and shortened SAD, and compared to the clinical treatment plans through isodose distributions, dose-volume histograms, and dosimetric indices. The control point specifications of the optimized tr-VMAT plans were used to estimate the delivery time.

Results: The optimized tr-VMAT plans with both shortened and standard SAD delivery yielded a comparable plan quality to the clinical treatment plans. A statistically significant benefit was observed for dose gradient index and monitor unit efficiency for shortened SAD tr-VMAT plans, while improved target volume conformity was observed for the clinical treatment plan ($p \leq 0.05$). A clear dosimetric benefit was not demonstrated between tr-VMAT delivery at shortened SAD compared to standard SAD, but shortened SAD delivery yielded a fraction-size dependent reduction in the estimated delivery time.

Conclusion: The implementation of "baseball stitch" tr-VMAT treatment plans to patients presented with cranial targets demonstrated comparable plan quality to clinical treatment plans. The delivery at shortened SAD produced a fraction size dependent decrease in estimated delivery time.

5.2 Introduction

Recent developments in linear accelerator design have enabled trajectory-based treatment, in which simultaneous motion of the gantry, treatment couch, and other components can be paired with volumetric modulated arc therapy (VMAT) optimization to improve treatment plan quality. Trajectory-based VMAT (tr-VMAT) provides the option for noncoplanar treatment with many potential advantages, including increased sparing of critical structures and steeper dose falloff outside the target volume [1]. Compared to intensity modulated radiation therapy (IMRT), tr-VMAT retains advantages characteristic of conventional coplanar arc delivery, such as decreased linear accelerator monitor unit output and reduced treatment time [2].

The generation of tr-VMAT treatment plans has commonly been separated into two steps: (1) the selection of a couch-gantry trajectory, succeeded by (2) a VMAT optimization performed on that trajectory. Initial approaches assessed the patient geometry for each gantry-couch angle combination in order to define a cost map that estimates the benefit of radiation delivery from that beam orientation. Shortest path algorithms or heuristic methods were then used to select a sequence of couch-gantry control points to be used during the optimization process [3–7]. A second method involves an initial step to identify anchor points using beam-angle optimization techniques. The trajectory is defined by the shortest path that traverses these anchor points, which minimizes the treatment time [7–9]. Inherent to this approach is the assumption that even though the final trajectory may include suboptimal beam orientations, the VMAT optimization algorithm will appropriately modify the delivery through aperture shaping and dose rate modulation to limit dose to critical structures.

The 4π technique has extended noncoplanar IMRT delivery to consider the entirety of the solution space during treatment plan optimization, demonstrating improved plan quality compared to conventional IMRT and VMAT treatments [10, 11]. With the goal of increased angular sampling approaching the 4π geometry, a study by Wilson *et al.* used patient-generalized trajectories applied to patients with cranial targets. The trajectories were variations of the "baseball stitch" delivery originating from the dynamic stereotactic radiosurgery method, but included an adjustable number of partial gantry arcs in order to assess the advantages of angular sampling [12, 13]. Both the 4π and the patient-generalized trajectory approaches demonstrated diminishing returns on the improvement of treatment plan quality with increased angular sampling, particularly with consideration of the effect on treatment delivery time.

Two studies have been presented that use iterative approaches to converge to a gantry-couch trajectory rather than adopting a two-step approach. The first uses a Monte Carlo tree search

to define trajectories, where the objective function following an optimization at the end of each iteration was used to guide the semi-random selection of trajectories in later iterations [14]. The second study alternated between a direct aperture optimization and beam orientation optimization step (DAO/BOO), and a beam trajectory selection step. The beam trajectory selection used a shortest path algorithm based on the results of the DAO/BOO to define the trajectory, and the beam orientations comprising that trajectory are used to adjust weighting of the DAO/BOO step in future iterations [15]. A comprehensive review of trajectory-based treatment planning is presented by Smyth *et al.* [1].

An unexplored aspect of trajectory-based treatment involves the use of translational couch motion in synchrony with gantry rotation in order to emulate isocentric treatment at a shortened source-to-axis (SAD) distance, which offers potential advantages including improved delivery precision due to the reduced width of the projected multileaf collimator (MLC) leaves at treatment isocenter, an increased effective dose rate by virtue of the reduced SAD, and steeper dose gradients [16].

The purpose of this work was to apply a generalized baseball stitch trajectory to clinical patients presented with cranial targets with the inclusion of translational couch motion to emulate shortened SAD delivery, with an emphasis on efficient treatment delivery. Tr-VMAT treatment plans at both shortened and conventional SAD were generated for ten patients and compared to clinically delivered treatment plans through isodose distributions, dose-volume histograms, and dosimetric indices.

5.3 Materials and Methods

5.3.1 Treatment planning workflow

The treatment planning process consisted of three major steps:

Beamlet dose calculation

Prior to optimization, beamlet doses were calculated for each patient using a collapsed-cone convolution-superposition (CC-CS) algorithm. The clinical CT data was downsampled into a 2 mm $\times$ 2 mm $\times$ 2 mm voxelized phantom, with voxels within the body defined as water with density scaled according to a piecewise linear Hounsfield unit-to-density conversion curve. The energy deposition kernel used for the CC-CS dose calculations was derived from the fluence spectrum of a Varian Truebeam 6 MV flattening-filter-free (FFF) beam using the EGSnrc EDK

code for cones separated into 3.75° segments extending to distances between 0.05 cm and 60 cm from the interaction point located in water [17].

Control points were defined along a baseball-stitch trajectory as follows:

$$\text{couch angle} = (270^\circ + n) \bmod 360^\circ \tag{5.1}$$

$$\text{gantry angle} = (180^\circ - 2n) \tag{5.2}$$

where n is the control point index ($0 \leq n \leq 180$). The target isocenter was calculated as the geometric center of the PTV.

A rectangular grid of non-diverging beamlets was arranged for each control point. Beamlet doses were calculated only for beamlets intersecting the target volume with a one beamlet margin. A uniform fluence was assumed for all beamlets belonging to a control point. To limit the beamlet file size, a dose threshold was applied for each beamlet calculation to omit voxels receiving less than 0.1% of the maximum dose. The beamlet dimensions were defined by the MLC width at target isocenter: 2.5 mm × 2.5 mm beamlets for 100 cm SAD delivery; 2.0 mm × 2.0 mm beamlets for 80 cm SAD delivery. The distance from the target isocenter to the radiation source was also adjusted according to the SAD.

VMAT Treatment Plan Optimization

The VMAT optimization algorithm used in this work follows the column generation approach [18–20]. The objective function is represented as the sum of user-defined dose-volume (DV) constraints in which voxels that violate the specified DV constraint are penalized by the square of the dose difference with a weighting factor. As applied to VMAT optimization, the column generation approach is a greedy heuristic in which apertures are iteratively added to the treatment plan from a pool of candidate apertures. At each iteration, the optimal weights of the apertures currently comprising the treatment plan are determined through minimization of the objective function, yielding a patient dose distribution on which the formation of subsequent candidate apertures is based. Fig. 5.1 provides an illustration of the column generation approach, and the process can be summarized as follows:

1. A candidate aperture for each undefined control point (without an associated aperture shape) is formed by solving the pricing problem. For each row in the rectangular beamlet grid for each control point, an optimal series of consecutive open beamlets are determined by

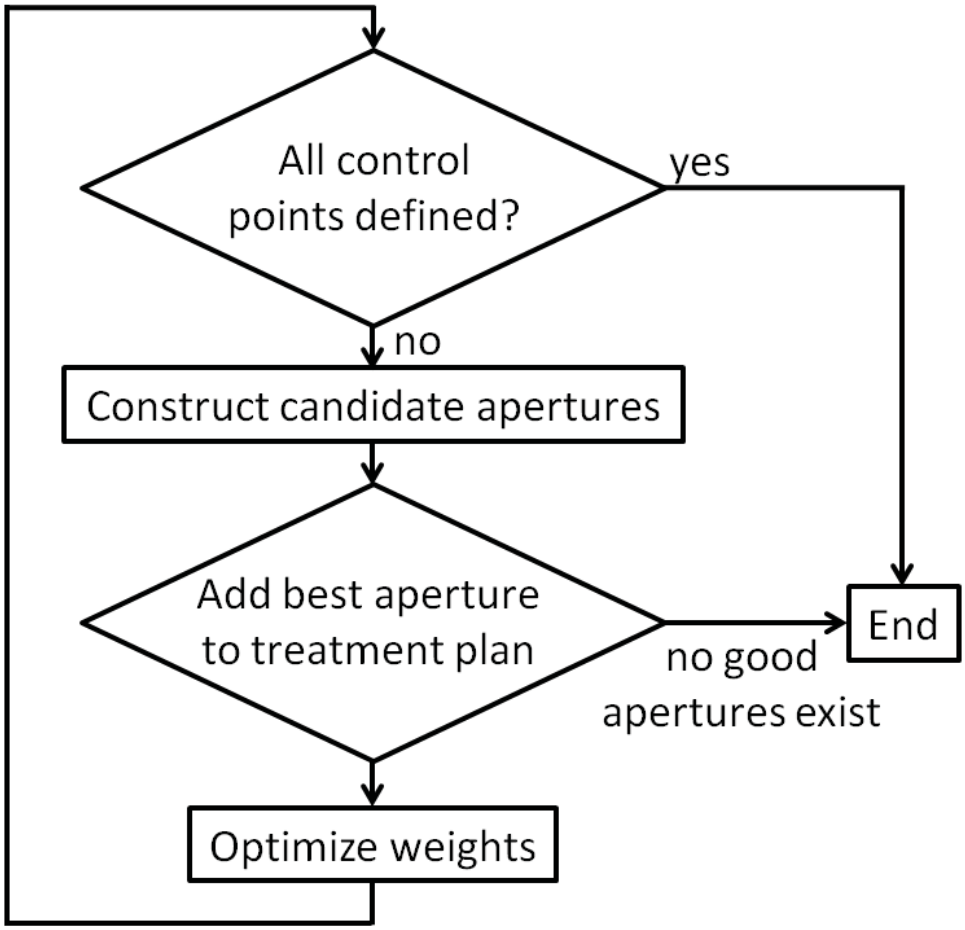

Figure 5.1 Flowchart summarizing the column generation approach applied to VMAT optimization.

calculating the first-order perturbation for each beamlet on the cost function. The resulting aperture has an associated price representing its value in minimizing the cost function.

2. The set of candidate apertures are ranked according to their price, and the single best aperture is added to the treatment plan.

3. The weights of all apertures comprising the current treatment plan are reoptimized, and a new dose distribution is calculated for the subsequent iteration.

This process is repeated until either no remaining undefined control points exist or no apertures can be constructed that will improve the treatment plan. If undefined control points remain at the end of the optimization, no radiation dose will be delivered at those beam orientations, and optionally, the MLC leaf pairs will be closed during delivery. The optimization of the aperture weights was driven by the interior-point optimizer (IPOPT) library [21]. A rigorous formulation of the column generation approach used in this work can be found in Renaud *et al*. [19]. For the purpose of VMAT optimization, an additional restriction was applied that only a single aperture may be defined per control point.

Machine delivery constraints were implemented during optimization based on a user-specified lower limit for the gantry rotation speed, which defines the maximum amount of time between adjacent control points while also imposing corresponding minimum speeds for the couch rotation and translation. The bounds on the allowed MLC leaf positions during the optimization are based on the maximum time between adjacent control points and their corresponding aperture shapes. For this study, the minimum gantry speed was set to 2°/s, corresponding to a maximum treatment time of 3 minutes for a 360° gantry arc based on the mechanical components of the linear accelerator. No restrictions were placed on the dose rate, which could result in a longer treatment time should the dose deposition specified at a control point not be achievable in the maximum allowed time defined by the minimum gantry rotation speed.

Final Dose Calculation

The final output of the optimization process is a series of aperture shapes with an associated weight, gantry angle, and couch angle, which is used to construct a DICOM RP file with each control point assigned a static MLC field with monitor unit (MU) weight proportional to the optimization weight. For the shortened 80 cm SAD plans, the treatment isocenter is shifted as a function of the couch and gantry angle in order to achieve the correct treatment distance. To apply the isocenter shift in the treatment planning system (Varian Eclipse), a transformation from the

Table 5.1 Selected clinical cases, clinical treatment modality, prescription dose, and fractionation scheme.

ID	Clinical Case	Treatment Modality	Pres. Dose (Gy)	Frac. Size (Gy)
acst1	acoustic neuroma	IMRT	50	2
avm1	arteriovenous malformation	CyberKnife	20	20
avm2	arteriovenous malformation	CyberKnife	20	20
eye1	whole eye irradiation	IMRT	30	3
met1	brain metastasis	CyberKnife	15	15
met2	brain metastasis	CyberKnife	12	12
met3	brain metastasis	CyberKnife	25	5
met4	brain metastasis	CyberKnife	21	21
met5	brain metastasis	CyberKnife	15	15
sin1	sinus meningioma	2-arc VMAT	50.4	1.8

gantry and couch rotation angles (g, c) into spherical (ϕ, θ) coordinates was applied [22]:

$$\phi = \tan^{-1} \frac{-\cos g}{\sin g \cos c} \tag{5.3}$$

$$\theta = \cos^{-1}(\sin g \sin c) \tag{5.4}$$

The desired isocenter shift s for delivery at 80 cm SAD (r = 20 cm) can be calculated as:

$$s = (-r\cos\phi\sin\theta, -r\sin\phi\sin\theta, r\cos\theta) \tag{5.5}$$

These input files are imported into the Eclipse treatment planning system and are applied to the original patient CT data. The final dose is given as the sum of the individual static MLC field doses calculated on a TrueBeam STx linear accelerator using the Eclipse analytic anisotropic algorithm (AAA, v11.0.31), using a calculation grid spacing of 1.5 mm with heterogeneity corrections.

5.3.2 Clinical cases

The patient cases selected for this study featured various cranial targets and clinical objectives. The target disease classification, clinical treatment modality, prescription dose, and fractionation scheme for each patient case are shown in Table 5.1.

The goal of the trajectory-based VMAT treatment planning process for each patient was to generate a comparable plan quality to the clinical treatment with regard to PTV coverage and OAR sparing. The optimization of the shortened and standard SAD treatment plans used the same dose-volume constraints.

5.3.3 Plan Evaluation Metrics

The comparisons between the quality of the clinical treatment plans and the tr-VMAT plans were made using dose distributions, dose-volume histograms, and dosimetric indices including Paddick's conformity index (pCI), gradient index (r50), homogeneity index (HI), and the max dose-to-prescription dose ratio (MDPD) [23, 24]:

$$\text{pCI} = \frac{TV_{\text{PIV}}^2}{TV \times PIV} \tag{5.6}$$

$$\text{r50} = \frac{V_{50\%}}{TV} \tag{5.7}$$

$$\text{HI} = \frac{D_{5\%} - D_{95\%}}{D_{\text{P}}} \tag{5.8}$$

$$\text{MDPD} = \frac{D_{\max}}{D_{\text{P}}} \tag{5.9}$$

where TV is the treatment volume, PIV is the prescription isodose volume, TV_{PIV} is the overlapping volume of the treatment volume and the prescription isodose volume, $V_{\text{X}\%}$ is the volume receiving at least X% of the prescription dose, $D_{Y\%}$ is the dose received by Y% of the PTV volume, D_{P} is the prescription dose, and $D_{\max}$ is the maximum dose delivered to the patient.

5.3.4 Nonstandard SAD AAA Dose Validation

Dose calculations using the Eclipse AAA have been extensively validated for static and modulated deliveries against both measurement and Monte Carlo simulations under standard treatment conditions [25–28], and agreement with measurement is expected to be within 3% under most circumstances [29]. To verify the fidelity of Eclipse AAA dose calculations at nonstandard treatment distances, the standard and shortened SAD tr-VMAT treatment plans for five patients (`acst1`, `avm1`, `met2`, `met3`, `met5`) were delivered on a TrueBeam STx linear accelerator (Varian Medical Systems, Palo Alto, CA) with collapsed gantry, couch, and collimator rotation angles (set to 0°) to a 30 × 30 × 30 water tank (Standard Imaging, Madison, WI). The cumulative monitor unit output for each plan was scaled to 1000 MU. Ionization chamber measurements (Exradin

Table 5.2 Nominal maximum values for Truebeam STx linear accelerator components.

Linear Accelerator Component	Nominal Maximum Value
MLC leaf translation	2.5 cm/s at machine isocenter
Gantry rotation	6°/s
Couch rotation	3°/s
Couch translation, vertical	2 cm/s
Couch translation, lateral	4 cm/s
Couch translation, longitudinal	8 cm/s
Dose rate (6X-FFF)	1400 MU/s

A1SL ionization chamber; Standard Imaging, Madison, WI) were recorded at a depth of 3.4 cm, with an SSD of 80 cm for the shortened SAD tr-VMAT plans, and an SSD of 100 cm for the standard SAD tr-VMAT plans. The ionization chamber measurements were scaled by the linear accelerator output measured following TG-51 [30], and compared to corresponding Eclipse AAA dose calculations under equivalent experimental conditions, with the mean dose scored over a contoured ionization chamber measurement volume.

5.3.5 Delivery Time

For each of the tr-VMAT treatment plans, an estimate of the delivery time was calculated using the control point information for each of the mechanical components and the radiation output of the Truebeam STx linear accelerator (Varian Medical Systems, Palo Alto, CA). A post-processing step was included to reposition closed leaf pairs in order to minimize the leaf travel distance between control points. During treatment delivery, the Truebeam STx linear accelerator will identify the limiting component for each control point and actively adjust the speed of the other components and the dose rate to compensate. An estimate of the delivery time for a treatment can be obtained by summing the required time for the limiting component at each control point of the treatment. This method ignores acceleration of the individual components and the time spent in accelerator ramp up and ramp down, but is meant as a relative time estimate to allow comparison of the different deliveries. Nominal maximum values for the linear accelerator components used for the delivery time calculations are shown in Table 5.2.

To validate the delivery time estimate based on the limiting component at each control point, standard SAD tr-VMAT plans for five patients (`acst1`, `avm1`, `met2`, `met3`, `met5`) were delivered on the TrueBeam STx linear accelerator, with the total time during the radiation delivery recorded.

5.3.6 Collision Avoidance

Deliverable trajectories with a uniform 80 cm SAD for the shortened SAD tr-VMAT plans are dependent on the patient anatomy and location of the target volume, and may not be achievable. To determine the clearance for an 80 cm SAD treatment, a convex hull was generated for each slice of the patient body contour and placed upon a trapezoidal prism representing the treatment couch. The shortest distance from the beam source to the patient was obtained through rotations of the patient-couch coordinates around the target isocenter corresponding to each beam orientation in the baseball stitch trajectory.

5.4 Results

5.4.1 Nonstandard SAD AAA Dose Calculation

The Eclipse AAA dose calculations and corresponding ionization chamber measurements for the collapsed tr-VMAT treatment plans are shown in Fig. 5.2. Points indicate the ionization chamber measurements, with the limits shown for the point dose minimum and maximum, as well as the mean dose calculated for the chamber volume in Eclipse at 80 cm SSD (red) and 100 cm SSD (blue) illustrating the dose gradient across the measurement volume. The average percentage difference for the dose calculations relative to the measurement were $0.08 \pm 0.96\%$ and $1.7 \pm 0.6\%$ for the standard SAD and shortened SAD delivery, respectively.

5.4.2 Plan Evaluation

The results for this study are shown for two cases, representing a conventional fractionation and a stereotactic fractionation: sinus meningioma (`sin1`, fraction size: 1.8 Gy), and brain metastasis (`met1`, fraction size: 15 Gy).

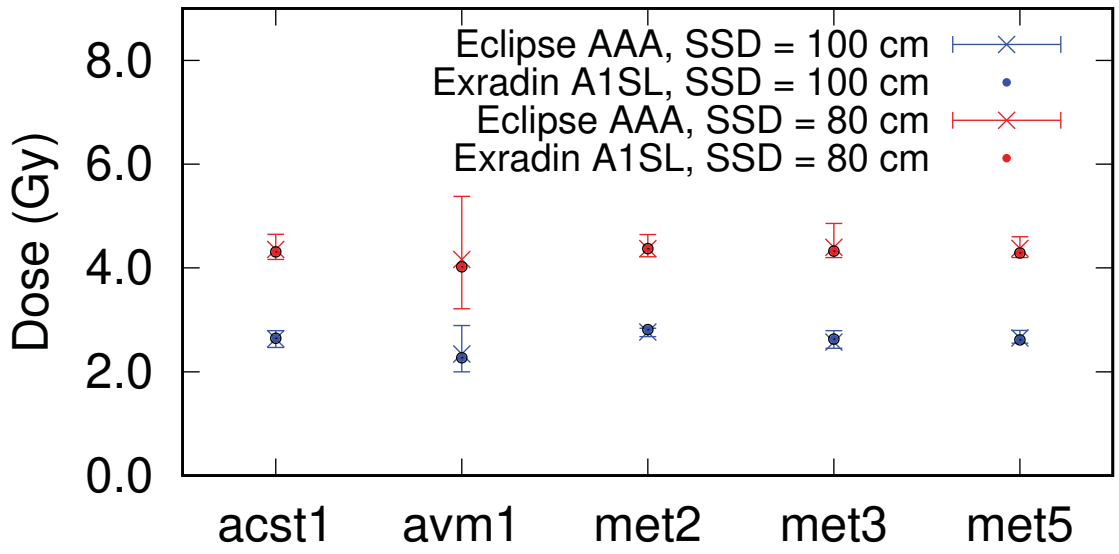

Figure 5.2 Eclipse AAA dose calculations relative to Exradin A1SL ionization chamber measurements for tr-VMAT plans with collapsed couch, collimator, and gantry rotation angles. The point dose minimum and maximum calculated by Eclipse for the chamber volume are shown as horizontal lines, with the Eclipse mean dose shown as $\times$s, and the points indicating the ionization chamber measurements. Red: shortened (80 cm) SSD; blue: standard (100 cm) SSD.

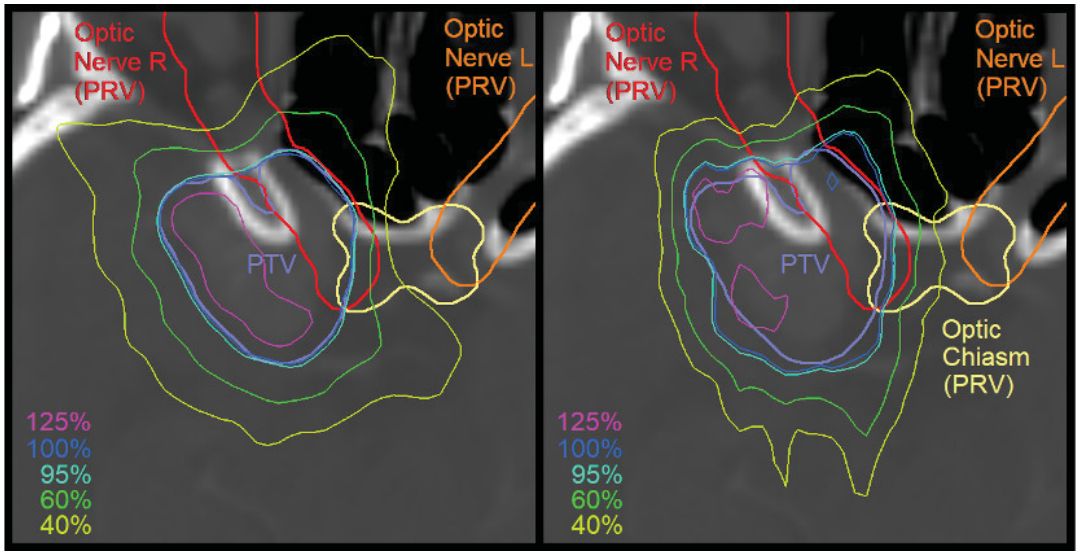

Figure 5.3 Comparison of clinical (left) and shortened SAD tr-VMAT (right) dose distributions for a sinus meningioma patient. The percentage of the prescription dose for the isodose lines is indicated for each dose distribution.

Sinus Meningioma

The treatment planning objective for the sinus meningioma case (`sin1`) specified a prescription of 50.4 Gy to 95% of the target volume, with a homogeneous dose desired for the region overlapping with the right optic nerve and optic chiasm and allowing for hot spots in the non-overlapping target volume. The clinical plan was a VMAT treatment featuring a 360° arc in addition to a partial arc with a 90° couch rotation. Isodose distributions comparing the clinical treatment plan to the shortened SAD tr-VMAT treatment plan are shown in Fig. 5.3. Dose-volume histograms are shown for the clinical, shortened SAD, and standard SAD treatment plans in Fig. 5.4.

The plan quality of the tr-VMAT plans for the sinus meningioma case closely match the noncoplanar two-arc VMAT clinical plan, with marginal improvements observed in the coverage of the target volume and intermediate dose sparing of the right and left optic nerve. The clinical plan demonstrates improved sparing of the optic chiasm, but a higher maximum dose to the PTV. The dosimetric indices indicate improved homogeneity for the tr-VMAT treatment plans, while the clinical treatment plan demonstrated improved dose gradients and conformity to the target volume. The shortened SAD tr-VMAT treatment plan required fewer MU to achieve the dose prescription.

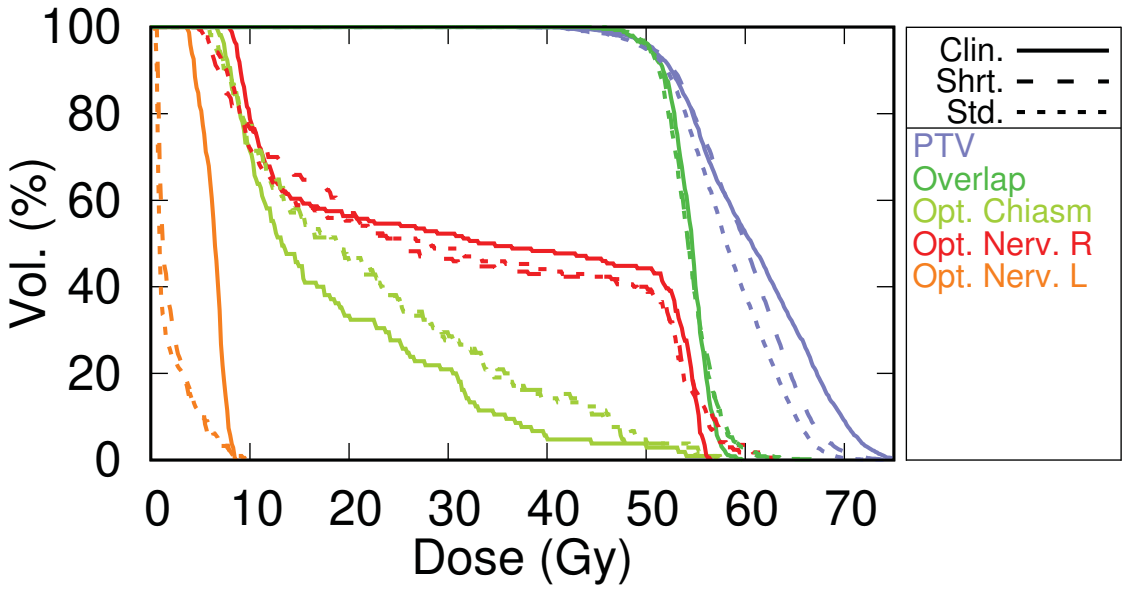

Figure 5.4 Dose-volume histogram comparing the clinical treatment plans (solid) to the trajectory-based VMAT treatment plans at shortened SAD (dashed) and standard SAD (dotted) for a sinus meningioma case.

Brain Metastasis

The treatment planning objective for the brain metastasis case (`met1`) specified 15 Gy to 99.9% of the target volume while limiting doses to critical structures. The clinical treatment plan was delivered using CyberKnife (Accuray, Sunnyvale, CA). Isodose distributions comparing the clinical treatment plan to the shortened SAD tr-VMAT treatment plan are shown in Fig. 5.5. Dose-volume histograms for the clinical, shortened SAD, and standard SAD treatment plans are shown in Fig. 5.6.

The tr-VMAT treatment plans demonstrate improved coverage the target volume compared to the clinical treatment plan, while also achieving sparing of the brainstem and chiasm. The dosimetric indices indicate improved dose gradients and homogeneity for the tr-VMAT plans, while the clinical treatment plan demonstrated improved conformity to the target volume. The shortened SAD tr-VMAT treatment plan required fewer MU to achieve the dose prescription.

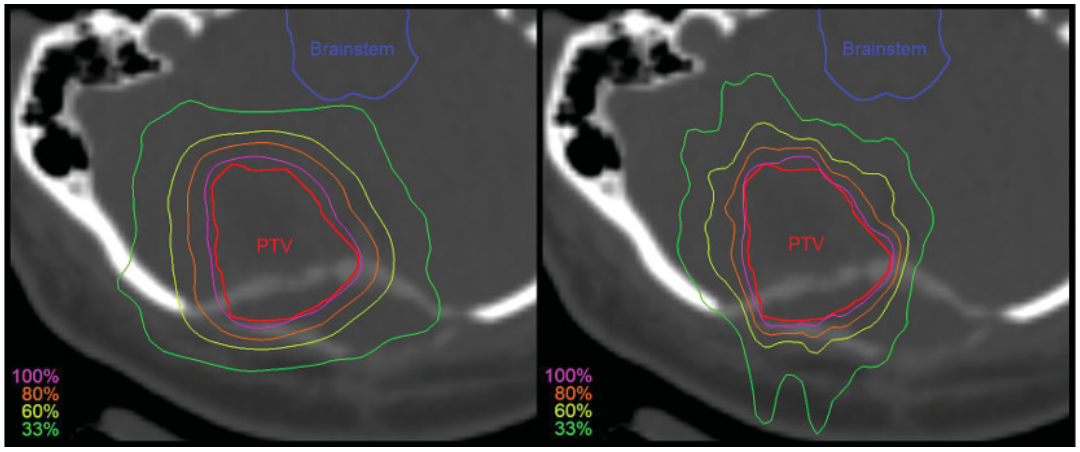

Figure 5.5 Comparison of clinical (left) and shortened SAD tr-VMAT (right) dose distributions for a brain metastasis case. The percentage of the prescription dose for the isodose lines is indicated for each dose distribution.

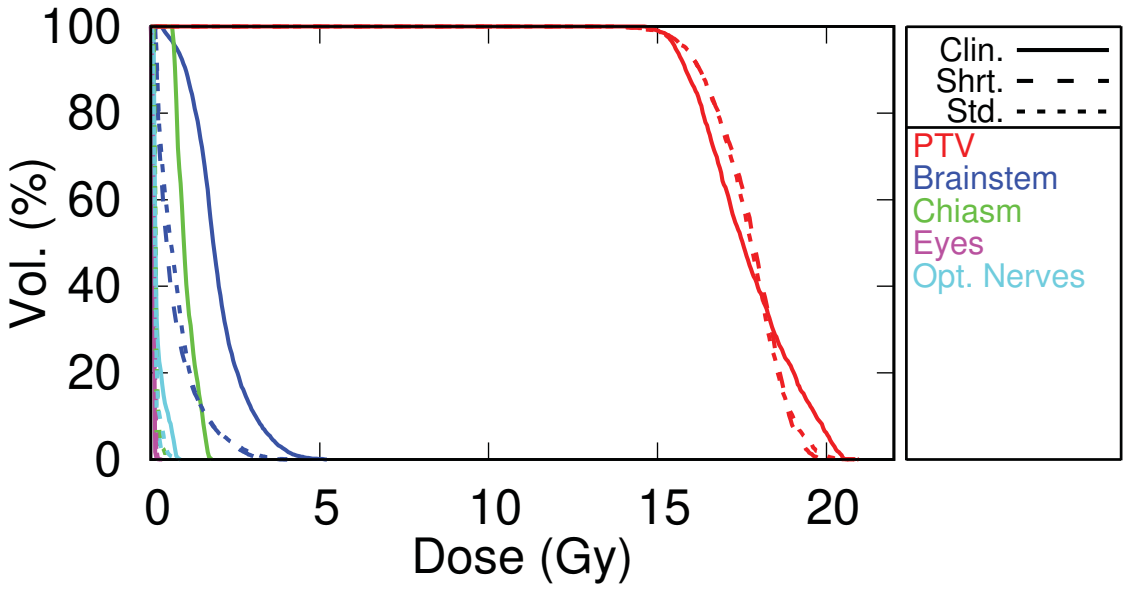

Figure 5.6 Dose-volume histogram comparing the clinical treatment plans (solid) to the trajectory-based VMAT treatment plans at shortened SAD (dashed) and standard SAD (dotted) for a brain metastasis case.

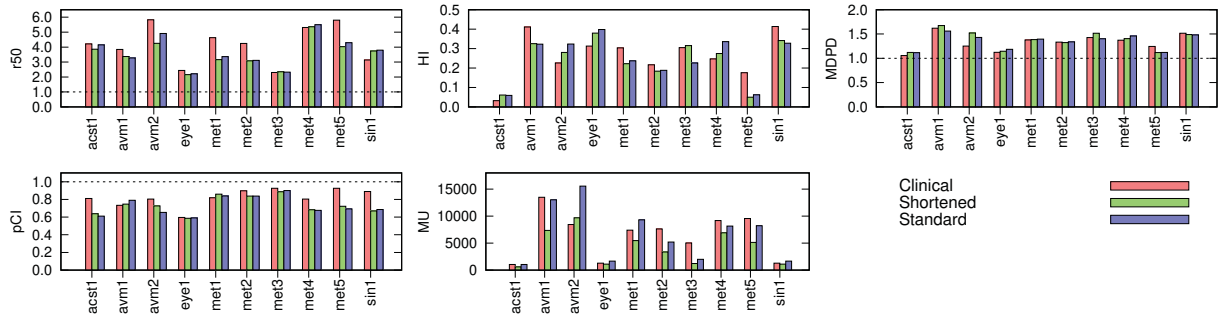

Figure 5.7 Comparison of clinical treatment plans to tr-VMAT treatment plans with shortened and standard SAD, using gradient index, homogeneity index, max dose to prescription dose (MDPD) ratio, conformity index, and cumulative monitor unit output. Dashed lines, if shown, indicate the ideal value for the index.

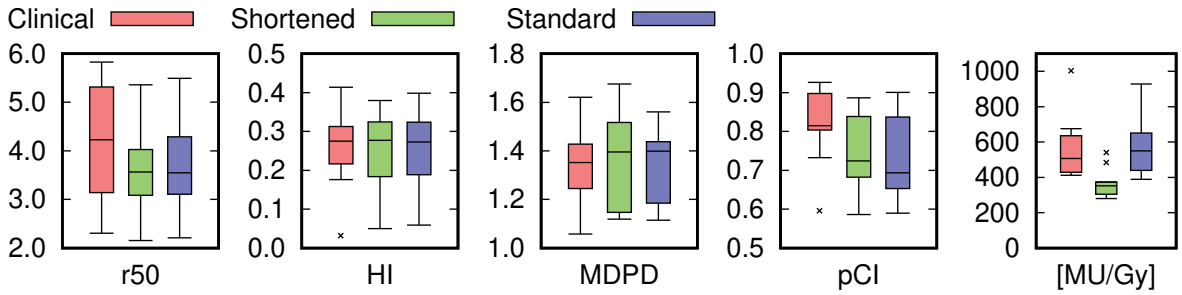

Figure 5.8 Boxplot representation of the data shown in Fig. 5.7. Limits indicate the quartile ranges of the data. The MU output data was divided by the fraction size for the treatment plan. Outliers are denoted as individual points.

5.4.3 Patient Cohort Statistics

Fig. 5.7 shows a comparison of the dosimetric indices and MU output for the clinical, shortened SAD, and standard SAD treatment plans individually for each patient case, and also depicted as a boxplot in Fig. 5.8, indicating the distribution of values for each treatment plan type. In Fig. 5.8, the MU delivered normalized to the fraction size was calculated and shown as an assessment of the radiation delivery efficiency. The dosimetric indices for the tr-VMAT treatment plans were assessed for statistical significance compared to the clinical treatment plan using the Wilcoxon signed rank test. With a criterion of $p \leq 0.05$, statistical significance was observed for (1) the gradient index for the shortened SAD tr-VMAT plan compared to the standard SAD tr-VMAT plan; (2) the MU/fraction size data comparing the shortened SAD tr-VMAT plan to the clinical plan; (3) the conformity index comparing the clinical plan to both shortened and standard SAD tr-VMAT plans. No statistically significant difference was demonstrated for homogeneity index or MDPD.

5.4.4 Delivery Time

An estimate of the delivery time for each of the components of a treatment plan as a function of control point is shown in Fig. 5.9 for the sinus meningioma and brain metastasis cases for both shortened and standard SAD delivery. The fraction size of the treatment plan was observed to impact the benefit of delivery at shortened SAD. For the sinus meningioma case with a fraction size of 1.8 Gy, the translational leaf speed was the limiting factor at both SADs for nearly every control point. As a result, the increased effective dose rate at shortened SAD did not yield a reduction in the cumulative delivery time. For the brain metastasis case with a fraction size of 15 Gy, a decrease in delivery time of over 2 minutes was observed with treatment at shortened SAD. The delivery time was estimated for each of the tr-VMAT plans in Table 5.3 by summing the time-limiting component at each control point. For the patient cases included in this study, the achievable decrease in treatment time when delivering a tr-VMAT treatment plan at a shortened SAD compared to standard SAD delivery as a function of the fraction size is shown in Fig. 5.10.

For the delivery of the five standard SAD tr-VMAT treatment plans on the TrueBeam STx linear accelerator, the measured time exceeded the estimated delivery time by 5.2 ± 1.5 s on average.

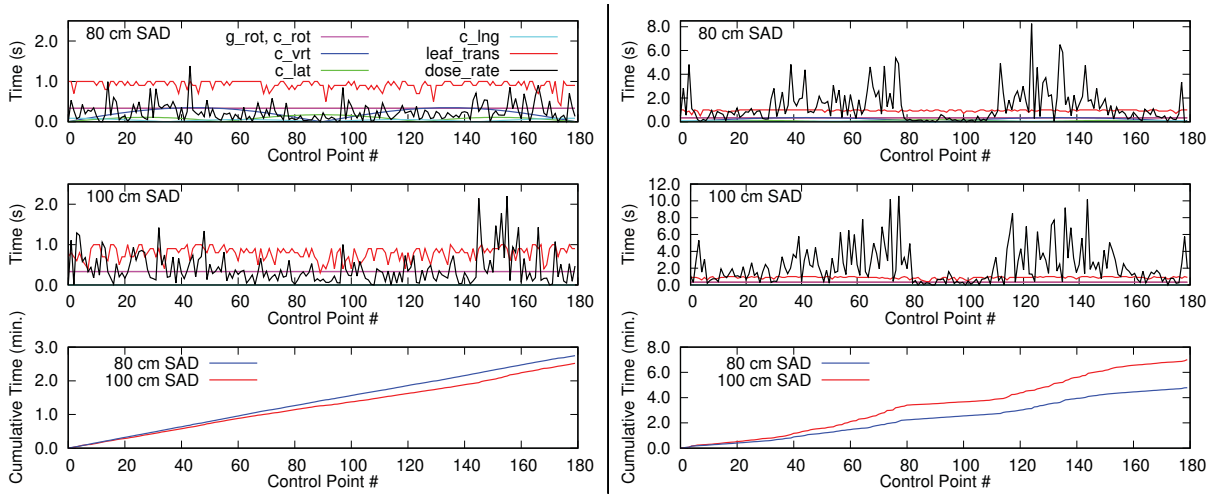

Figure 5.9 Estimated delivery time for individual treatment plan components as a function of control point index. Top: shortened SAD delivery; Middle: standard SAD delivery; Bottom: delivery time comparison of shortened and standard SAD by taking the time-limiting component for each control point of the above graphs. Left: sinus meningioma case, 1.8 Gy fraction size; Right: brain metastasis case, 15 Gy fraction size.

Table 5.3 Delivery time estimates for the tr-VMAT treatment plans. The potential benefit of delivery at shortened SAD was observed to depend on the fraction size of the treatment.

Plan	Delivery Time (min:sec)		Fraction Size (Gy)
	Shortened SAD	Standard SAD	
acst1	2:55	2:50	2
avm1	5:53	9:23	20
avm2	7:19	11:16	20
eye1	2:44	2:22	3
met1	4:48	7:03	15
met2	3:36	4:50	12
met3	3:00	3:00	5
met4	5:38	6:31	21
met5	4:15	6:11	15
sin1	2:46	2:32	1.8

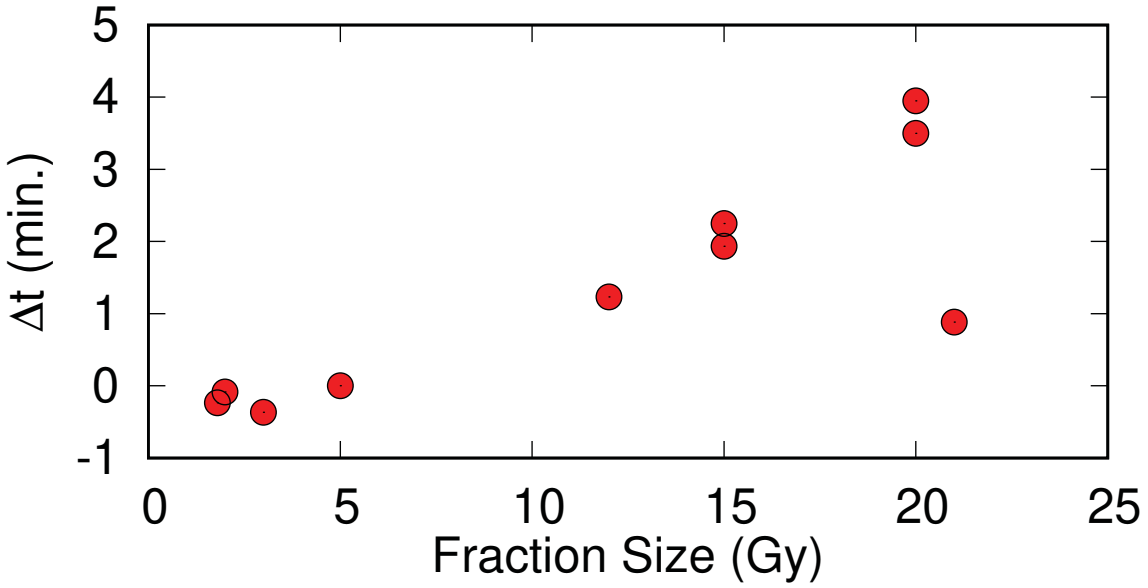

Figure 5.10 Estimated time difference between tr-VMAT treatments delivered at standard and shortened SAD, as a function of the fraction size of the treatment.

5.4.5 Collision Avoidance

Fig. 5.11 depicts the closest achievable SAD for the brain metastasis (`met1`) and sinus meningioma (`sin1`) patients. Due to the position of the target volume on the right side of the body for both cases, a segment with the gantry rotation angle near 90° in each baseball stitch trajectory is not deliverable at 80 cm SAD. Only two of the tr-VMAT treatment plans were deliverable throughout the entire trajectory at 80 cm SAD. The average closest SAD varied between 71-78 cm across all patients.

5.5 Discussion

Delivery of the tr-VMAT treatment plans showed an average ionization chamber agreement within 2% for both shortened (80 cm) and standard (100 cm) SSD delivery, validating the use of Eclipse AAA dose calculations commissioned at 100 cm SSD for shortened SAD static MLC field delivery. This dose calculation accuracy is assumed to extend to arc-based delivery with conventional 2° gantry angle spacing between adjacent control points [20, 31].

With respect to plan quality, although the tr-VMAT treatment plans did not demonstrate statistical significance in the gradient index compared to the clinical treatment plans across the entire

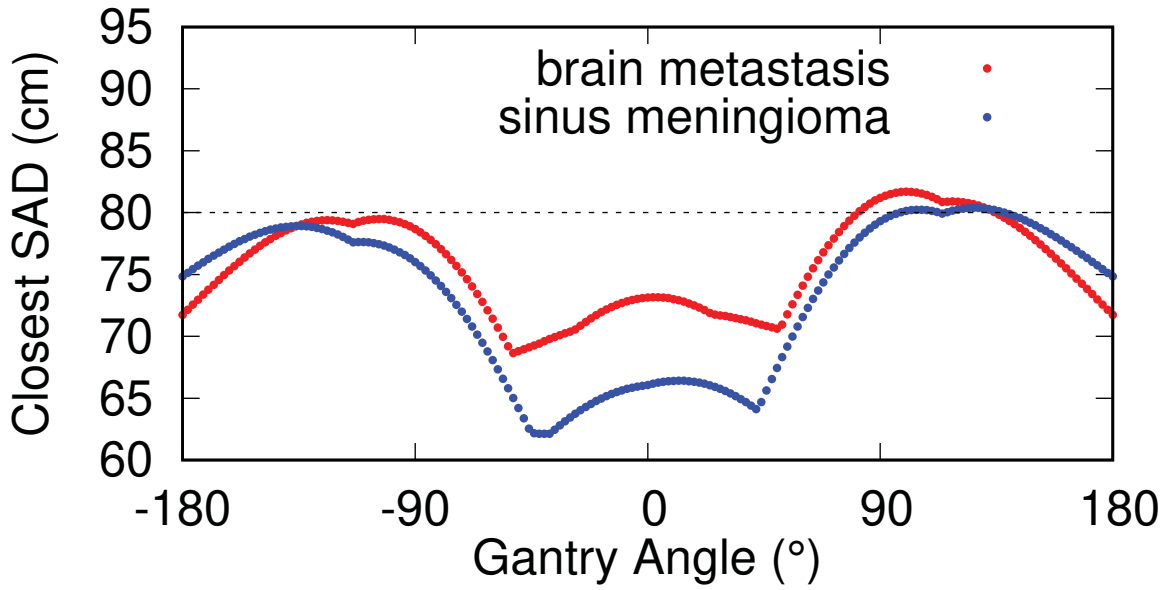

Figure 5.11 Closest achievable SAD for each beam orientation in a baseball stitch trajectory for brain metastasis (`met1`) and sinus meningioma (`sin1`) patients. Points shown above the dashed line are not deliverable with a uniform 80 cm shortened SAD.

patient cohort, the Wilcoxon signed rank test indicated statistical significance with the exclusion of the `sin1` patient, which was treated clinically with two-arc VMAT including a couch rotation. The clinical treatment plans demonstrated a statistically significant improvement in conformity index. The Paddick conformity index combines a factor representing the coverage of the target volume by the prescription dose and a factor that represents spillage of the prescription dose into surrounding healthy tissue. The optimized trajectory-based plans demonstrated comparable or better PTV coverage to the clinical treatment plans, but the conformity index was deteriorated due to spillage of dose outside the target volume. The decreased conformity index for the tr-VMAT plans is partially attributed to degradation of the optimized dose distribution following the final dose calculation using AAA. A potential source of the dose degradation may be the discrepancy between the voxel size used for the beamlet dose calculations (2.0 mm $\times$ 2.0 mm $\times$ 2.0 mm) and the grid spacing used in the final dose calculation (1.5 mm). Due to the size of the target volumes in the patient cohort, these dimensions were each chosen to be as small as possible given computational considerations such as memory and optimization time. Tr-VMAT treatment plans were able to closely match the dose-volume objectives indicated by the DVH of the clinical dose distribution and demonstrated a comparable plan quality to the clinical treatment plans.

Although delivery at a shortened SAD with a decreased effective leaf width has been observed to result in physical improvements of the dose distribution [32], tr-VMAT delivery at shortened SAD did not exhibit clear dosimetric benefits compared to standard SAD delivery. The beamlet-based optimization approach may limit the potential improvements with a smaller projected leaf size, as the permitted leaf positions are at discrete rather than continuous locations. Delivery at shortened SAD yielded a decrease in MU for 9 out of 10 patient cases, both compared to the standard SAD delivery and the clinical treatment plan, which will reduce out-of-field dose to the patient and reduce the risk of secondary malignancies [33, 34].

The potential reduction in delivery time when delivering at a shortened SAD was observed to be dependent on the fraction size of the treatment. For conventional fractionation (1.8-2 Gy), the translational leaf motion limited the efficiency of the treatment delivery. For larger fraction sizes, however, the increased dependence of the delivery time on the maximum dose rate yielded substantial reductions in delivery time of up to 4 minutes at a shortened SAD. The delivery time estimates were calculated under the assumption of a 1400 MU/min dose rate delivered with a flattening-filter-free treatment beam. The measured treatment times for five standard SAD treatment plans compared to the corresponding estimates differed by an average of 5.2 ± 1.5 s, supporting the time limiting component methodology for estimating the treatment time. For delivery with flattening filter at lower maximum dose rates, leaf motion will be less of a constraint and a decrease in delivery time might be achieved even for treatment plans with conventional fractionation. With translational couch motion during delivery, patient comfort may limit the couch movement speed to below its maximum value, but for large fraction sizes, this restriction is unlikely to impact the delivery time. For patients immobilized with thermoplastic masks, the potential reduction in treatment time may improve the accuracy of the radiation delivery, as studies have shown a dependence of the magnitude of intrafraction motion on the elapsed time since initial patient positioning [35, 36].

The choice of a uniform 80 cm SAD for the shortened SAD delivery was based on estimates of the maximum achievable reduction in SAD for the treatment of cranial targets. The geometrical assessment of the patients throughout the baseball trajectory revealed undeliverable segments that would necessitate an increase in the SAD to avoid collisions. With the implementation of a uniform 85 cm SAD delivery that would avoid the collision risk for all patients in the study, the effective dose rate relative to the 80 cm SAD delivery would be 88.6% under an inverse square law approximation. Recalculating the treatment delivery time for the shortened SAD treatment plans with this reduced dose rate yielded an average increase of 20 s, with the largest increase observed for the `avm2` patient of 53 s. In clinical practice, stereotactic frames and other immobilization

devices may limit the achievable SAD reduction, and the implementation of a safety margin should be considered. However, although the SAD was chosen to be a uniform distance in this work, a closest SAD trajectory could be delivered that would provide the greatest benefit to the patient. The average achievable closest SAD for all patients ranged between 71 cm and 78 cm SAD, suggesting further increases in effective dose rate are achievable compared to the uniform 80 cm SAD used in this study.

The use of extended SAD trajectories has been shown to increase the collision-free angular space [11, 37], but the use of a patient-generalized baseball stitch trajectory for cranial targets in this work precludes the necessity of additional viable beam orientations. The demonstrated advantages of this work with respect to reductions in MU output and treatment time are dependent on the use of a shortened SAD trajectory.

During the treatment planning process, the inflexibility of the patient-generalized trajectory limited the generation of clinically viable plans for a small number of patients not included in this study. The unfavorable arrangement of critical structures relative to the target volume position for the baseball stitch beam orientations prevented the adherence to both lower limit target volume and upper limit critical structure dose-volume constraints simultaneously. The patient-specific approaches presented in the literature could be combined with shortened SAD delivery, and would represent a compromise between improved dosimetric outcomes and the benefits associated with decreased treatment delivery time.

The effect of patient comfort throughout a treatment involving rotational and translational couch on the dose delivery accuracy remains a concern for the clinical viability of trajectory-based treatments, although patients in a phase I trial have been shown to tolerate well 4π static beam IMRT treatments involving couch rotation and translation in between radiation delivery [11]. The positional accuracy of the treatment couch during translational couch motion has been previously evaluated through trajectory log file analysis for test treatment plans, measuring a root-mean-square-error (RMSE) within 1 mm [38]. A similar analysis was performed for patient-generalized trajectories with a monotonically increasing couch rotation angle (in the absence of translational couch motion), measuring RMSE on the order of 0.05° for both the gantry and couch rotation angles. In addition, delivery validation was performed for the patient-generalized trajectories, with ionization chamber measurements within 2% and radiochromic film measurements with a gamma pass rate above 98% (criteria: 2 mm/2%) [12]. These results suggest that it is achievable to accurately deliver trajectory-based treatment plans involving both translational and rotational couch motion in a clinical setting.

5.6 Conclusion

Trajectory-based VMAT treatment plans along a noncoplanar baseball stitch trajectory were optimized using a column generation optimization approach and compared to clinically delivered dose distributions. Trajectory-based VMAT treatment plans with shortened SAD delivery yielded comparable plan quality to the clinical treatment plans, with improvements in dose gradients outside the PTV volume and PTV coverage, and demonstrating comparable or improved OAR sparing with a decrease in cumulative MU. A fraction size dependent reduction in the estimated treatment delivery time was observed when comparing tr-VMAT delivery at a shortened SAD of 80 cm compared to conventional SAD treatment.

References

[1] G. Smyth, P. M. Evans, J. C. Bamber, and J. L. Bedford, "Recent developments in non-coplanar radiotherapy," Br J Radiol **92** (2019).

[2] M. Teoh, C. H. Clark, K. Wood, S. Whitaker, and A. Nisbet, "Volumetric modulated arc therapy: a review of current literature and clinical use in practice," Br J Radiol **84**, 967–996 (2011).

[3] Y. Yang, P. Zhang, L. Happersett, J. Xiong, J. Yang, M. Chan, K. Beal, G. Mageras, and M. Hunt, "Choreographing couch and collimator in volumetric modulated arc therapy," Int. J. Radiat. Oncol., Biol., Phys. **80**, 1238–1247 (2011).

[4] G. Smyth, J. C. Bamber, P. M. Evans, and J. L. Bedford, "Trajectory optimization for dynamic couch rotation during volumetric modulated arc therapy," Phys. Med. Biol. **58**, 8163–8177 (2013).

[5] R. L. MacDonald and C. G. Thomas, "Dynamic trajectory-based couch motion for improvement of radiation therapy trajectories in cranial SRT," Med. Phys. **42**, 2317–2325 (2015).

[6] M. K. Fix, D. Frei, W. Volken, D. Terribilini, S. Mueller, O. Elicin, H. Hemmatazad, D. M. Aebersold, and P. Manser, "Part 1: Optimization and evaluation of dynamic trajectory radiotherapy," Med. Phys. **45**, 4201–4212 (2018).

[7] M. Langhans, J. Unkelbach, T. Bortfeld, and D. Craft, "Optimizing highly noncoplanar vmat trajectories: the NoVo method," Phys. Med. Biol. **63**, 025023 (2018).

[8] D. Papp, T. Bortfeld, and J. Unkelbach, "A modular approach to intensity-modulated arc therapy optimization with noncoplanar trajectories," Phys. Med. Biol. **60**, 5179–5198 (2015).

[9] E. Wild, M. Bangert, S. Nill, and U. Oelfke, "Noncoplanar VMAT for nasopharyngeal tumors: Plan quality versus treatment time," Med. Phys. **42**, 2157–2168 (2015).

[10] P. Dong, P. Lee, D. Ruan, T. Long, E. Romeijn, Y. Yang, D. A. Low, P. Kupelian, and K. Sheng, "4π non-coplanar liver SBRT: a novel delivery technique," Int. J. Radiat. Oncol., Biol., Phys. **85**, 1360–1366 (2013).

[11] V. Y. Yu, A. Landers, K. Woods, D. Nguyen, M. Cao, D. Du, R. K. Chin, K. Sheng, and T. B. Kaprealian, "A prospective 4π radiation therapy clinical study in recurrent high-grade glioma patients," Int. J. Radiat. Oncol., Biol., Phys. **101**, 144–151 (2018).

[12] B. Wilson, K. Otto, and E. Gete, "A simple and robust trajectory-based stereotactic radiosurgery treatment," Med. Phys. **44**, 240–248 (2017).

[13] E. B. Podgorsak, A. Olivier, M. Pla, P.-Y. Lefebvre, and J. Hazel, "Dynamic stereotactic radiosurgery," Int. J. Radiat. Oncol., Biol., Phys. **14**, 115–126 (1988).

[14] P. Dong, H. Liu, and L. Xing, "Monte Carlo tree search-based non-coplanar trajectory design for station parameter optimized radiation therapy (SPORT)," Phys. Med. Biol. **63**, 135014 (2018).

[15] Q. Lyu, V. Y. Yu, D. Ruan, R. Neph, D. O'Connor, and K. Sheng, "A novel optimization framework for VMAT with dynamic gantry couch rotation," Phys. Med. Biol. **63**, 125013 (2018).

[16] K. Bratengeier, K. Holubyev, and S. Wegener, "Steeper dose gradients resulting from reduced source to target distance—a planning system independent study," J. Appl. Clin. Med. Phys. **20**, 89–100 (2019).

[17] E. Mainegra-Hing, D. W. Rogers, and I. Kawrakow, "Calculation of photon energy deposition kernels and electron point dose kernels in water," Med. Phys. **32**, 685–699 (2005).

[18] H. E. Romeijn, R. K. Ahuja, J. F. Dempsey, and A. Kumar, "A column generation approach to radiation therapy treatment planning using aperture modulation," SIAM J. Optim. **15**, 838–862 (2005).

[19] M.-A. Renaud, M. Serban, and J. Seuntjens, "On mixed electron-photon radiation therapy optimization using the column generation approach," Med. Phys. **44**, 4287–4298 (2017).

[20] F. Peng, X. Jia, X. Gu, M. A. Epelman, H. E. Romeijn, and S. B. Jiang, "A new column-generation-based algorithm for VMAT treatment plan optimization," Phys. Med. Biol. **57**, 4569–4588 (2012).

[21] A. Wachter and L. T. Biegler, "On the Implementation of a Primal-Dual Interior Point Filter Line Search Algorithm for Large-Scale Nonlinear Programming," Mathematical Programming **106**, 25–57 (2006).

[22] J. Thebaut and S. Zavgorodni, "Coordinate transformations for BEAM/EGSnrc Monte Carlo dose calculations of non-coplanar fields received from a DICOM-compliant treatment planning system," Phys. Med. Biol. **51**, N441–9 (2006).

[23] I. Paddick, "A simple scoring ratio to index the conformity of radiosurgical treatment plans," J. Neurosurg. **93**, 219–222 (2000).

[24] T. Kataria, K. Sharma, V. Subramani, K. P. Karrthick, and S. S. Bisht, "Homogeneity index: An objective tool for assessment of conformal radiation treatments," J. Med. Phys. **37**, 207–213 (2012).

[25] A. Van Esch, L. Tillikainen, J. Pyykkonen, M. Tenhunen, H. Helminen, S. Siljamäki, J. Alakuijala, M. Paiusco, M. Iori, and D. P. Huyskens, "Testing of the analytical anisotropic algorithm for photon dose calculation," Med. Phys. **33**, 4130–4148 (2006).

[26] A. Fogliata, G. Nicolini, A. Clivio, E. Vanetti, and L. Cozzi, "Accuracy of Acuros XB and AAA dose calculation for small fields with reference to RapidArc stereotactic treatments," Med. Phys. **38**, 6228–6237 (2006).

[27] M. W. K. Kan, L. H. T. Leung, R. W. K. So, and P. K. N. Yu, "Experimental verification of the Acuros XB and AAA dose calculation adjacent to heterogeneous media for IMRT and RapidArc of nasopharyngeal carcinoma," Med. Phys. **40**, 031714 (2013).

[28] E. Sterpin, M. Tomsej, B. De Smedt, N. Reynaert, and S. Vynckier, "Monte Carlo evaluation of the AAA treatment planning algorithm in a heterogeneous multilayer phantom and IMRT clinical treatments for an Elekta SL25 linear accelerator," Med. Phys. **34**, 1665–1677 (2007).

[29] G. A. Ezzell, J. M. Galvin, D. Low, J. R. Palta, I. Rosen, M. B. Sharpe, P. Xia, Y. Xiao, L. Xing, and C. X. Yu, "Guidance document on delivery, treatment planning and clinical implementation of IMRT: Report of the IMRT subcommittee of the AAPM radiation therapy committee," Med. Phys. **30**, 2089–2115 (2003).

[30] P. R. Almond, P. J. Biggs, B. M. Coursey, W. F. Hanson, M. S. Huq, R. Nath, and D. W. O. Rogers, "AAPM Task Group 51: protocol for clinical reference dosimetry of high energy photon and electron beams," Med. Phys. **26**, 1847–1870 (1999).

[31] K. Otto, "Volumetric modulated arc therapy: IMRT in a single gantry arc," Med. Phys. **35**, 310–317 (2008).

[32] T. Bortfeld, U. Oelfke, and S. Nill, "What is the optimum leaf width of a multileaf collimator?," Med. Phys. **27**, 2494–2502 (2000).

[33] E. J. Hall and C. S. Wuu, "Radiation-induced second cancers: the impact of 3D-CRT and IMRT," Int. J. Radiat. Oncol., Biol., Phys. **56**, 83–88 (2003).

[34] S. F. Kry, M. Salehpour, D. S. Followill, M. Stovall, D. A. Kuban, R. A. White, and I. I. Rosen, "The calculated risk of fatal secondary malignancies from intensity-modulated radiation therapy," Int. J. Radiat. Oncol., Biol., Phys. **62**, 1195–1203 (2005).

[35] M. S. Hoogeman, J. J. Nyuttens, P. C. Levendag, and B. J. Heijmen, "Time dependence of intrafraction patient motion assessed by repeat stereoscopic imaging," Int. J. Radiat. Oncol., Biol., Phys. **70**, 609–618 (2007).

[36] D. Amelio, M. Winter, D. Habermehl, O. Jäkel, J. Debus, and S. E. Combs, "Analysis of inter- and intrafraction accuracy of a commercial thermoplastic mask system used for image-guided particle radiation therapy," J. Radiat. Res. **54**, i60–i76 (2013).

[37] J. Liang, T. Atwood, R. von Eyben, B. Fahimian, E. Chin, K. Horst, K. Otto, and D. Hristov, "Trajectory modulated arc therapy: A fully dynamic delivery with synchronized couch and gantry motion significantly improves dosimetric indices correlated with poor cosmesis in accelerated partial breast irradiation," Int. J. Radiat. Oncol. Biol. Phys. **92**, 1148–1156 (2015).

[38] A. Rodrigues, F.-F. Yin, and Q. Wu, "Dynamic electron arc radiotherapy (DEAR): a feasibility study," Phys. Med. Biol. **59**, 327–345 (2014).

5.7 Clarifications after manuscript publication

- The software used in this work includes both in-house developed and commercial software. The collapsed-cone convolution-superposition was written by a colleague and implemented for a graphics processing unit (GPU) using the Nvidia CUDA compiler. Calculation of the beamlet dose distributions was also aided by an in-house treatment planning system called Radify, which included scripts for arranging the beamlet grids and defining the dose calculation parameters. The VMAT optimization software using the column generation approach was implemented in C++ using the IPOPT library. Final dose calculations were performed in the Varian Eclipse treatment planning system using the Analytic Anisotropic Algorithm (AAA, v11.0.31).

- In the discussion of machine delivery constraints (section 5.3.1), it was stated that treatment times could be longer than predicted based on the imposed lower gantry rotation speed, as a consequence of not considering the maximum dose rate in the optimization. Under these conditions, the treatment plan delivery would be achieved through a proportional decrease of the mechanical linear accelerator component speeds as the dose deposition rate is at a maximum for the affected control points.

- For the nonstandard SAD AAA dose validation (section 5.3.4), the cumulative monitor units for each delivered treatment plan were scaled to 1000 MU. This was performed for efficiency, as the clinical cases delivered included fraction sizes as high as 20 Gy, with 13000 MU at the standard SAD for the `avm1` patient. For a collapsed treatment plan delivery with static MLC apertures, the measured dose and monitor unit output will be proportional, with no expected change to the conclusions of this measurement due to the MU scaling.

- For the discussion of selected clinical cases (section 5.4.2), the sinus meningioma tr-VMAT plans were noted as having improved sparing of the left and right optic nerves, but worsened sparing of the optic chiasm compared to the clinical treatment plan. This is in part due to the patient-generalized trajectory approach. For this patient, segments of the tr-VMAT arc resulted in overlaps between the chiasm and PTV from the perspective of these beam orientations, compromising the sparing of the chiasm. For the clinical treatment plan, the

second VMAT arc with a 90° couch rotation permitted increased sparing of the chiasm in addition to the benefits of the noncoplanar delivery.

- Conventional clinical practice for patients presented with cranial targets may involve the use of a CyberKnife treatment unit, which features a 6 MV miniaturized linear accelerator mounted on a robotic arm, and fixed collimating cones or a multileaf collimator as beam-shaping devices. In the literature, noncoplanar VMAT treatments (multiple arcs at various static couch rotation angles) have demonstrated improved dose conformity with worsened dose falloff compared to CyberKnife treatment plans, with a decrease in treatment delivery time and monitor unit output [1, 2]. The achievable dose rate with the CyberKnife treatment unit is 1000 MU / min, specified at the nominal SAD of 80 cm [3] (compared to the approximate 2000 MU / min that would be achieved at a shortened SAD on a conventional linear accelerator with a nominal dose rate of 1400 MU / min). In the work presented by Zhang *et al.*, CyberKnife treatment plans required 29 000 MU and a beam-on time of 30 min on average for brain metastasis treatments [1], substantially greater than the treatment delivery times estimated for the tr-VMAT plans generated for this manuscript. Additionally, this work featured seven clinical CyberKnife treatment plans, with the tr-VMAT treatments demonstrating a comparable plan quality.

5.7.1 References

[1] S. Zhang, R. Yang, C. Shi, J. Li, H. Zhuang, S. Tian, J. Wang, "Noncoplanar VMAT for brain metastases: a plan quality and delivery efficiency comparison with coplanar VMAT, IMRT, and CyberKnife," Technol. Cancer Res. Treat. **18** (2019).

[2] N. Kadoya, Y. Abe, T. Kajikawa, K. Ito, T. Yamamoto, R. Umezawa, T. Chiba, Y. Katsuta, Y. Takayama, T. Kato, Y. Kikuchi, K. Jingu, "Automated noncoplanar treatment planning strategy in stereotactic radiosurgery of multiple cranial metastases: HyperArc and CyberKnife dose distributions," Med. Dosim. **44** (2019).

[3] A. Conti, P. Romanello, E. Pantelis, S. G. Soltys, Y. H. Cho, M. Lim, *CyberKnife NeuroRadiosurgery.* Springer, (2020).

6

Simultaneous trajectory and volumetric modulated arc therapy optimization

Joel Mullins, Marc-André Renaud, Monica Serban, and Jan Seuntjens
Article published in: *Medical Physics, vol. 47, pp. 3078-3090, 2020.* [20]

Preface

Following the implementation of the shortened SAD trajectories, the focus was shifted to the implementation of a novel trajectory optimization algorithm using gantry and couch rotation. The conventional approach to trajectory optimization in the literature followed a two-step approach where the VMAT optimization was considered independently of the determination of the trajectory path, which was identified as potentially suboptimal. The iterative nature of the column generation approach, and the properties of its pricing problem, provided a methodology to simultaneously determine the trajectory path during treatment plan optimization.

6.1 Abstract

Purpose: Trajectory-based treatment planning involves the combination of a gantry-couch trajectory with volumetric modulated arc therapy (VMAT) treatment plan optimization. This work presents the implementation of an optimization methodology that generates a trajectory simultaneous with treatment plan optimization (simTr-VMAT).

Methods: The optimization algorithm is based on the column generation approach, in which a treatment plan is iteratively constructed through the solution of a subproblem called the "pricing problem". The property of the pricing problem to rank candidate apertures based on their associated price is leveraged to select an optimal aperture while simultaneously determining the trajectory path. A progressively increasing gantry-couch grid resolution is used to provide an initial coarse sampling of the angular solution space while maintaining fine control point spacing with the final treatment plan. The trajectory optimization was applied and compared to coplanar VMAT treatment plans for a lung patient, a glioblastoma patient, and a prostate patient. Algorithm validation was performed through the generation of 5000 random trajectories and optimization using column generation VMAT for each patient case, representing the solution space for the trajectory optimization problem. The simTr-VMAT trajectories were compared against these random trajectories based on a quality metric that prefers trajectories with few control points and low objective function value over long, inefficient trajectories.

Results: For the lung patient, the simTr-VMAT plan resulted in a decrease of the mean dose of 1.5 Gy and 1.0 Gy to the heart and ipsilateral lung, respectively. For the glioblastoma patient, the simTr-VMAT plan resulted in improved PTV coverage with a decrease in mean dose to the eyes, lens, nose, and contralateral temporal lobe between 2 and 7 Gy. The prostate patient showed no clinically-relevant dosimetric improvement. The simTr-VMAT treatment plans ranked at the 99.6, 96.3, and 99.4 percentiles compared to the distribution of randomly generated trajectories for the lung, glioblastoma, and prostate patients, respectively.

Conclusion: The simTr-VMAT optimization methodology resulted in treatment plans with equivalent or improved dosimetric outcomes compared to coplanar VMAT treatment plans, with the trajectories resulting from the optimization ranking among the optimal trajectories for each patient case.

6.2 Introduction

Trajectory-based radiation therapy combines concurrent gantry and treatment couch rotation with volumetric modulated arc therapy (VMAT) treatment plan optimization. The trajectories involved in these treatments are often noncoplanar, yielding steeper dose gradients outside the target volume, and may be customized to the patient anatomy or based on treatment planning objectives in order to avoid irradiation of critical structures. The nonconvex nature of the trajectory-based VMAT optimization problem necessitates the use of heuristic solutions that reduce the complexity and size of the solution space to generate clinically acceptable treatment plans while maintaining computational tractability.

In the literature, trajectory-based VMAT (tr-VMAT) optimization techniques have often followed a two-step approach, involving the selection of a gantry-couch trajectory followed by a VMAT optimization performed on that trajectory. The methods used to define a trajectory may be categorized under one or more of the following:

1. Cost Map: An assessment of viable beam delivery orientations is performed, assigning a score based on a geometric analysis of the target volume and critical structures from each beam's eye view. From the resulting cost map, heuristic or graph-search optimization methods are used to select a gantry-couch trajectory that preferentially includes beam orientations with beneficial overlap scores [1–5].

2. Travelling Salesman: Initial anchor points (beam orientations) are selected using beam angle optimization, and are connected by solving for the shortest possible trajectory that traverses all anchor points as an instance of the travelling salesman problem [5–7].

3. Patient-generalized trajectory: A predefined trajectory is designed, and applied in general to patients with a similar disease site. The trajectory adequately samples the angular space in order to ensure good treatment plan quality [8].

Following the selection of a gantry-couch trajectory using one of these methods, a VMAT optimization characterizes multileaf collimator (MLC) aperture shapes and weights to arrive at a final treatment plan. The benefits cited by the above studies include reductions in mean and maximum doses received by critical structures, improved dosimetric indices such as dose falloff or target conformity, and gains in treatment delivery efficiency. However, treating trajectory-based VMAT optimization as a two-step process is potentially suboptimal [9]. With cost map methods, the beam orientations that comprise a trajectory are being considered independently during

the formation of a trajectory. For example, parallel-opposed beam orientations might share a beneficial geometric overlap score, but the inclusion of both orientations could result in undesired dose buildup in normal tissue that could have been avoided with a noncoplanar delivery angle, despite a less desirable overlap score. The travelling salesman methods (without supplementary cost map data, as in Langhans *et al.*) and patient-generalized methods form trajectories without consideration of the patient anatomy, and rely on oversampling of the angular space to generate acceptable treatment plans at the expense of efficient treatment delivery. Without combining the VMAT optimization and the trajectory formation into a single step, the potential of tr-VMAT may not be fully realized.

Two studies have been presented that take consideration of the patient dose distribution during formation of the trajectory-based treatment plan. The first study used a Monte Carlo tree search technique to guide the selection of a trajectory with an iterative approach. With each iteration, a trajectory-based treatment plan was optimized, and the resultant objective function was used to update an average score for each beam orientation comprising that trajectory, guiding the formation of semi-random trajectories in future iterations [10]. The second study alternated between generating a fluence map for each beam orientation, and using a direct aperture optimization and beam orientation optimization method. A trajectory was selected from the fluence map using a shortest path algorithm. Unselected beam orientations were penalized during subsequent fluence map optimizations as the solution iteratively converged to a final trajectory-based treatment plan [11]. Both studies enforced a monotonically increasing couch rotation angle for the beam orientations comprising their trajectories, helping to ensure patient comfort and safety while maintaining computational tractability, and performed a full VMAT optimization with each iteration.

In the present work, the formation of a trajectory and the treatment plan optimization are performed simultaneously. The column generation approach is used to define a set of candidate apertures at different beam orientations, and iteratively select one aperture to add to the trajectory. The recalculation of the patient dose distribution with each iteration ensures that subsequent beam orientations added to the trajectory are chosen for their relevance to the treatment planning objectives. Candidate apertures are not restricted to monotonically increasing couch rotation angles, allowing improved assessment of the angular solution space.

6.3 Materials and Methods

6.3.1 Optimization Methodology

Column Generation

An aperture-based formulation for treatment plan optimization is given as:

$$\text{minimize: } f(\mathbf{z}) \tag{6.1}$$

$$\text{subject to: } \mathbf{z} = \sum_k \mathbf{A}_k w_k, k = 1, \ldots, K \tag{6.2}$$

$$w_k \geq 0 \tag{6.3}$$

where $f(\mathbf{z})$ is the objective function that encodes the treatment planning constraints, and is a function of $\mathbf{z}$, the voxel-based patient dose distribution. The dose distribution is calculated as the sum of the aperture doses $\mathbf{A}_k$ multiplied by their (non-negative) optimization weight w_k.

The column generation approach is a heuristic in which the set of aperture doses $A = \{\mathbf{A}_1, \ldots, \mathbf{A}_K\}$ is iteratively built through the solution of a subproblem (called "the pricing problem"). For a given set of beam orientations S, beamlet-based apertures are constructed row-by-row by evaluating the first-order perturbation for each beamlet on the objective function. The resulting candidate apertures have an associated price, and in our implementation, the highest ranking aperture is added to the treatment plan at each iteration.

With the addition of each new aperture to A, $f(\mathbf{z})$ is minimized, resulting in new optimization weights $\{w_k\}$ and patient dose distribution $\mathbf{z}$. Future iterations of the pricing problem are performed based on the updated dose distribution. Additional details on the column generation approach for treatment plan optimization can be found in the literature [12–14].

The set A is a subset of all possible apertures at all possible beam orientations, and the purpose of the column generation approach is to iteratively populate A by selecting apertures that will yield an acceptable treatment plan. For intensity modulated radiation therapy (IMRT) or VMAT optimization, the set of beam orientations S from which apertures can be formed are predetermined and fixed throughout the optimization, either at specific delivery angles (IMRT) or at discrete checkpoints along a continuous arc (VMAT). In this work, rather than a predetermined set, the beam orientations under consideration vary dynamically during the optimization based on the current state of the trajectory-based treatment plan. The property of the pricing problem to rank a set of candidate apertures is leveraged to simultaneously select the optimal aperture and

determine the trajectory path throughout the treatment plan optimization, which we designate "simTr-VMAT".

Notation and conventions

Trajectories are constructed based on a $n \times n$ gantry-couch coordinate system, in which gantry angles range between -180° and 180°, and couch angles range between -90° and 90°. The spacing between coordinates on the grid is given as:

$$\Delta g_i = \frac{360^\circ}{n_i - 1} \tag{6.4}$$

$$\Delta c_i = \frac{180^\circ}{n_i - 1} \tag{6.5}$$

where the index i refers to the iteration number of the progression of the grid resolution, which will be expanded upon in a later section. The grid coordinates define the set of allowable beam orientations during the optimization.

A control point is an object with an associated gantry angle, couch angle, aperture dose, and optimization weight. For trajectory-based delivery, each control point contains references to the previous and next control points in the arc, which may be undefined during the optimization.

$$\text{Control Point } k\text{:} \begin{cases} g_k & \text{gantry angle} \\ c_k & \text{couch angle} \\ \mathbf{A}_k & \text{aperture dose} \\ \rightarrow k+1 & \text{next control point} \\ \rightarrow k-1 & \text{previous control point} \end{cases} \tag{6.6}$$

The treatment plan is represented in intermediary stages of the optimization as an ordered list of trajectory segments. Each trajectory segment is comprised of one or more spatially connected control points, which implies that adjacent control points are separated by no more than one unit of gantry rotation and one unit of couch rotation (as defined by Δg_i and Δc_i). Therefore, for the grid resolution progression denoted by the index i, the treatment plan is given by $T_i = \{t_0, \ldots, t_m\}$, where m is the number of trajectory segments t, and $t_j = \{k_0, \ldots k_J\}$ represents a trajectory segment with J spatially connected control points. Of particular importance for trajectory segments are the

control points at the head (k_0) and tail (k_J) of the list, as these are used to define the candidate beam orientations before instantiating the pricing problem.

Upon completion of the optimization, the treatment plan will contain a single trajectory segment comprised of K control points. The following sections will delineate the identification of candidate beam orientations, the merging of adjacent trajectory segments, the progression of the gantry-couch grid resolution, the instantiation of the treatment plan optimization, and other implementation details.

Candidate Beam Orientation Identification

With each column generation iteration, a new set of beam orientations S is generated by evaluating each trajectory segment in the treatment plan for potential additions to the trajectory path. For each t_j, the position of its tail control point relative to the head control point of t_{j+1} defines beam orientations to add to S, as shown in Fig. 6.1a. The position of the head of t_j relative to the tail of t_{j-1} defines additional beam orientations. The candidate beam orientations feature an incremental rotation of the gantry angle (Δg_i), couch angle (Δc_i), or both, and are defined such that trajectory segments can be consistently connected.

Through the pricing problem, candidate apertures are constructed for each beam orientation in the set S. The highest-ranking candidate aperture is selected and its associated dose is added to A, and a control point object is instantiated and connected to the relevant trajectory segment endpoint. With each control point added to a trajectory segment, the potential to merge with the adjacent trajectory segment is assessed to determine if the new beam orientation is located an incremental rotation from the adjacent trajectory segment. The trajectory for grid resolution index i is finalized when it is comprised of a single trajectory segment and S is empty.

Gantry-Couch Grid Resolution

To encourage improved angular sampling during the optimization process, and to maintain a fine spacing between control points for the final treatment plan, a progressively increasing gantry-couch grid resolution is implemented. Following the finalization of a trajectory with grid resolution index i, each individual control point comprising the trajectory is redefined as a new trajectory segment (Fig. 6.1b). The grid resolution index is incremented, allowing the candidate beam orientation identification procedure to continue at the increased resolution. The grid dimensions used in this work were $n = \{5, 13, 37, 145\}$, corresponding to a progression of the grid resolution of: (Δg, Δc) = (90°, 45°) $\rightarrow$ (30°, 15°) $\rightarrow$ (10°, 5°) $\rightarrow$ (2.5°, 1.25°). The final grid resolution

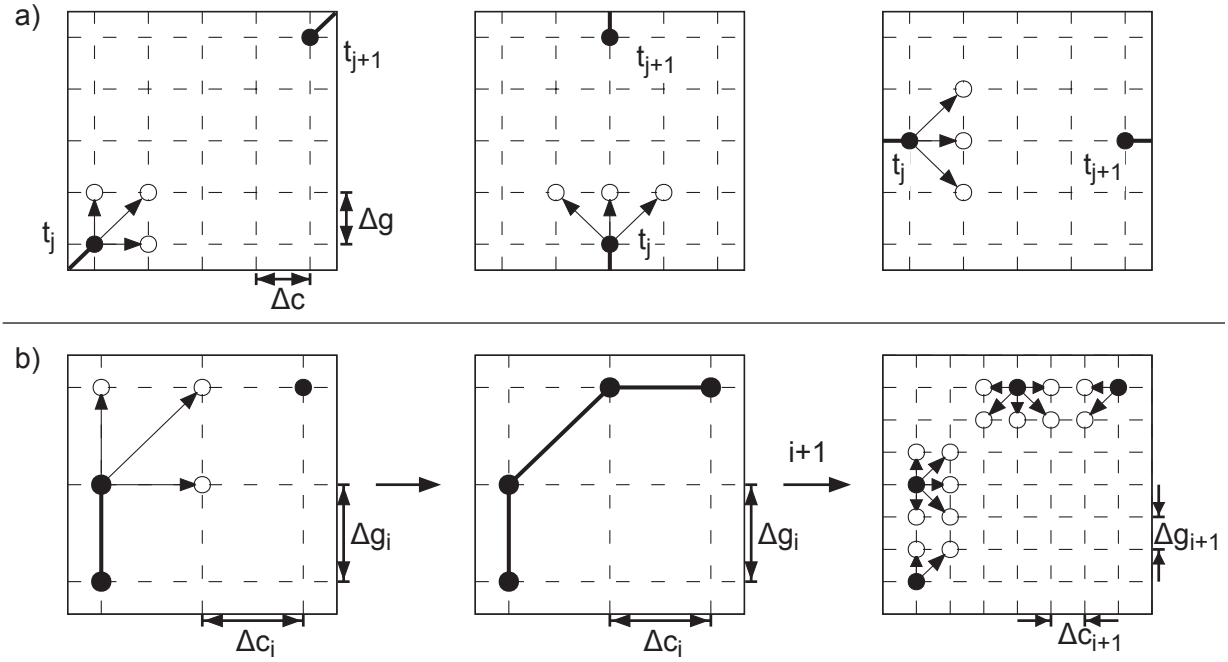

Figure 6.1 a) Candidate beam orientations are identified based on the relative position of the endpoints of adjacent trajectory segments t_j and t_{j+1}; b) With the completion of a trajectory with grid resolution index i, each control point forming that trajectory is redefined as a trajectory segment and the grid resolution is increased.

of $(\Delta g, \Delta c) = (2.5^\circ, 1.25^\circ)$ was chosen to yield final treatment plans comprised of a comparable number of control points to conventional multi-arc VMAT treatment plans.

The addition of candidate beam orientations to S is modified at the final grid resolution to include only beam orientations that linearly connect between adjacent trajectory segment endpoints. This prevents abrupt changes in the direction of couch/gantry rotations that may compromise patient comfort and dose delivery accuracy during treatment.

Optimization Instantiation

At the start of the treatment plan optimization, a beam orientation is required to define the initial trajectory segment. From this coordinate, candidate beam orientations are added to S that direct the trajectory segment endpoints to a gantry angle of $\pm 180^\circ$, at an arbitrary couch rotation angle. Beam orientations that feature couch-only rotations in either clockwise or counterclockwise directions are also added to S. When a beam orientation is added with a gantry angle of $\pm 180^\circ$, the addition of further candidate beam orientations to S is restricted, as any further couch rotations are equivalent to a rotation of the linear accelerator collimator with no change in beam orientation.

The initial beam orientation is selected from a predefined set of coordinates on the gantry-couch grid (see Eq. 6.7) through the pricing problem. The pricing of candidate apertures prior to a nonzero patient dose distribution results in adherence to all upper dose limit constraints by definition, therefore the constructed apertures through the pricing problem will be conformal to the target volume from the beam's eye view due to the lower dose limit constraints.

$$\begin{aligned} \{(g,c)_{u,v}\} = \{(-90^\circ + 90^\circ u, -45^\circ + 45^\circ v)\} \\ u, v \in \{0,1,2\} \end{aligned} \tag{6.7}$$

Collision Zones

The angular space was assessed for restricted collision regions through modelling of the patient, couch, and gantry. A convex hull of the patient body contour was placed upon a trapezoidal prism representing the treatment couch, and was assessed for intersection with a plane representing the treatment head of the gantry at each gantry-couch angle coordinate. For patients with target volumes located in the torso or abdomen where the CT scan does not cover the extent of the anatomy, the convex hull was extended axially. Raytracing from the linear accelerator source to a beamlet grid enclosing the target volume was performed to exclude oblique beam orientations that

entered the patient inside the body contour of the first or last axial CT slice. The resulting collision regions were consistent with those of other published works [3, 11, 15]. During treatment plan optimization, any candidate beam orientation that was located in a restricted collision region was removed from S.

Delivery constraints

Machine delivery constraints were implemented similarly to Peng *et al.*, where the defined lower limit for the gantry rotation speed defines the maximum time difference between adjacent control points in the treatment arc, and in turn, the allowable limits for MLC leaf motion with respect to the adjacent aperture shapes (based on a maximum leaf translation speed). For trajectory-based delivery that may include couch-only rotations between adjacent control points k and $k+1$, the maximum time difference is given as:

$$\tau_{k,k+1} = \max\left(\frac{|g_k - g_{k+1}|}{\dot{g}_{\min}}, \frac{|c_k - c_{k+1}|}{\dot{c}_{\min}}\right) \tag{6.8}$$

where $\dot{g}_{\min}$ and $\dot{c}_{\min}$ are the defined lower limits for the gantry and couch rotation speed, respectively.

For control point k, $\tau_{k-1,k}$ and $\tau_{k,k+1}$ define the limits for allowable leaf positions, which are observed during the pricing problem as apertures are constructed. Further details on the implementation of delivery constraints using the column generation approach can be found in Peng *et al.*[13]. In this work, no restrictions were placed on the dose rate, which may increase the treatment delivery time should the dose to be delivered over a control point range $k \rightarrow k+1$ not be achievable in $\tau_{k,k+1}$, requiring a compensatory adjustment of the speed of the mechanical linear accelerator components.

Implementation Details

Beamlet doses used during the optimization were precalculated using a collapsed-cone convolution-superposition algorithm. The energy deposition kernel was derived from the fluence spectrum of a Varian Truebeam 6 MV flattening-filter-free beam [16]. The optimization of aperture weights was driven by the interior-point optimizer (IPOPT) library [17]. Following completion of the beamlet-based optimization, full aperture doses were recalculated using a BeamNRC-based Monte Carlo beam model [18], and the weights were optimized to obtain a final dose distribution. Throughout all stages of the optimization, the patient dose calculation grid resolution was 2.5 mm $\times$ 2.5 mm $\times$ 3 mm, matching the grid resolution for the clinical patients.

6.3.2 Patient Cases

The simTr-VMAT optimization algorithm was applied to a lung, a brain, and a prostate case (dose-volume constraints are included in a supplementary file; Tables 6.3, 6.4, 6.5). The lung patient was diagnosed with an upper left lobe tumour, situated in close proximity to the heart and received stereotactic body radiation therapy (SBRT) treatment with 48 Gy in 3 fractions to the PTV. The brain patient was diagnosed with a glioblastoma tumour in the right frontotemporal lobe, with the PTV partially overlapping the right optic nerve, brainstem, cochlea, chiasm and situated in close proximity to the right eye and pituitary gland. The patient received an IMRT treatment with 60 Gy in 30 fractions to the PTV. The prostate patient received a VMAT treatment with 60 Gy delivered to the prostate gland (PTV60) and 44 Gy to the pelvic lymph nodes (PTV44) in 20 fractions. The prostate gland and nodal PTVs were partially overlapping the rectum, bladder and bowel. For each patient, a coplanar VMAT-field arrangement treatment plan (2 to 3 arcs) was optimized using the Eclipse treatment planning system (Varian Medical Systems, Palo Alto, California, USA). For the glioblastoma patient, the gantry angle range for the treatment arcs was limited to -180° and 45°, to avoid delivery through the contralateral temporal lobe.

6.3.3 Algorithm Validation

As a nonconvex optimization problem, the viability of a particular heuristic solution to trajectory-based treatment planning can be difficult to demonstrate. The generation of a clinically acceptable treatment plan does not guarantee that the gantry-couch trajectory obtained will rank highly among all possible trajectories in the solution space.

To validate the simTr-VMAT optimization algorithm, trajectory paths were generated following the methodology described above (including the increasing resolution of the coordinate grid), but with the beam orientations forming the trajectory path chosen randomly prior to treatment plan optimization. The random trajectories were optimized using conventional column generation VMAT, with a predetermined set S of beam orientations. For this analysis, the final gantry-couch grid resolution was $(\Delta g, \Delta c) = (10°, 5°)$, resulting in a 37×37 grid (totalling 1369 coordinates), with the randomly generated trajectories ranging between 35 and 130 control points in length.

For each of the patient cases in the study, 5000 random trajectories were generated and optimized using the column generation approach for VMAT optimization. For each random trajectory, the trajectory path and final objective function value were recorded. An additional treatment plan optimization was performed for each patient case representing a coplanar VMAT treatment plan. To attain an appropriate number of control points comprising the treatment plan

for comparisons to the randomly generated trajectories, the coplanar VMAT plans featured two 360° gantry arcs, with a total of 73 control points. The objective function value and trajectory path of simTr-VMAT treatment plans finalized at the same 37×37 gantry-couch grid resolution were also recorded.

6.4 Results

6.4.1 Patient Cases

The final simTr-VMAT optimized treatment plans are shown in Fig. 6.2 (lung), Fig. 6.3 (glioblastoma), and Fig. 6.4 (prostate), featuring the trajectory shown on the gantry-couch grid, dose-volume histograms comparing to the coplanar VMAT treatment plans, a 3D visualization of the trajectory, and a characteristic axial CT slice depicting the relevant anatomy with delineated targets and organs-at-risk (OARs). The trajectory map shows the simTr-VMAT trajectory as a blue line, with forbidden collision zones shaded in red. For the 3D rendering of the trajectory, the colour scale is shown only to guide the eye along the trajectory. Tables 6.1, 6.2 list relevant dosimetric statistics for the target volume and critical structures in each patient case.

Fig. 6.5 shows the progression of the trajectory optimization at each gantry-couch grid resolution for the glioblastoma patient. Green points indicate the beam orientations defined at the previous grid resolution acting as trajectory segment endpoints for the current grid resolution, with the control points added to the trajectory path shown as blue points. The beam orientations considered by the pricing problem during the trajectory optimization but that were not added to the treatment plan are shown as black points. The shaded blue regions illustrate the range of potential trajectories for each gantry-couch grid resolution based on the previously defined beam orientations.

Lung

The trajectory resulting from the simTr-VMAT optimization features a circuitous path for the first half of the trajectory with couch rotation angles between -45° and 5° and the corresponding beam orientations positioned on the ipsilateral side of the patient. In the second half of the trajectory, the gantry angle is near 0°, with beam delivery angles positioned anterior to the patient. Relative to the coplanar VMAT treatment plan, the simTr-VMAT dose optimization yielded, for similar target coverage, a large decrease in the mean heart dose (by 1.2 Gy lower), as well as decreases in

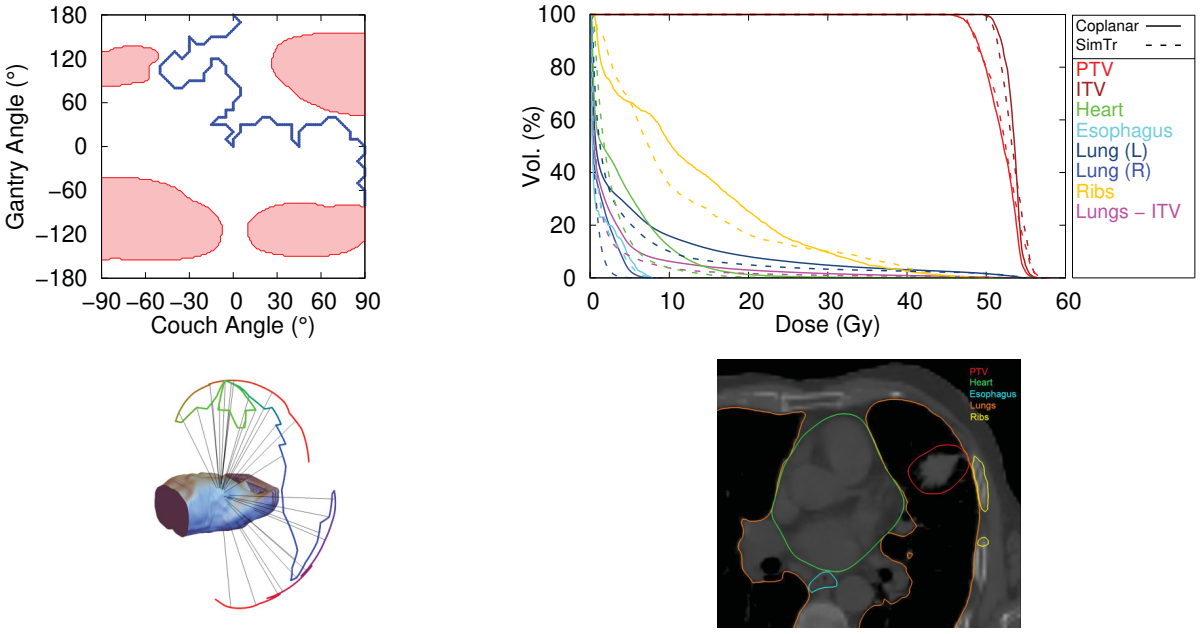

Figure 6.2 SimTr-VMAT treatment plan optimization for a lung patient. Top left: the final optimized trajectory is shown in blue, and collision zones are shaded in red; top right: dose-volume histogram comparison between the coplanar VMAT plan (solid) and the simTr-VMAT plan (dashed); bottom left: 3D visualization of the patient anatomy and the final optimized trajectory. The colour scale is shown only to guide the eye; bottom right: patient anatomy.

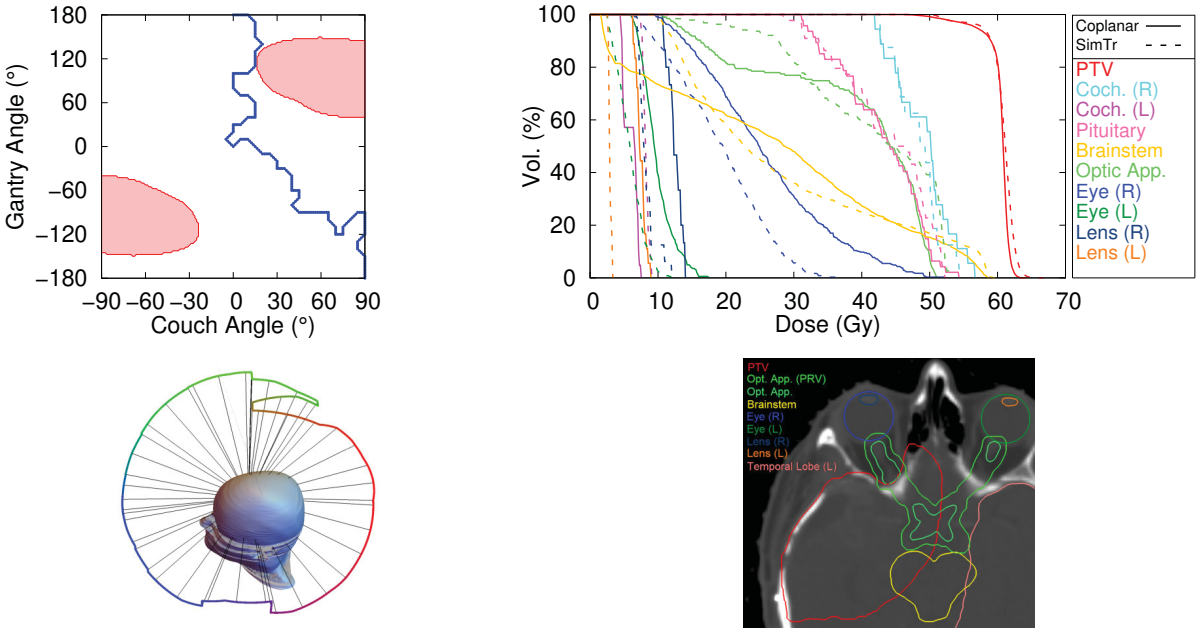

Figure 6.3 SimTr-VMAT treatment plan optimization for a glioblastoma patient. Top left: the final optimized trajectory is shown in blue, and collision zones are shaded in red; top right: dose-volume histogram comparison between the coplanar VMAT plan (solid) and the simTr-VMAT plan (dashed); bottom left: 3D visualization of the patient anatomy and the final optimized trajectory. The colour scale is shown only to guide the eye; bottom right: patient anatomy.

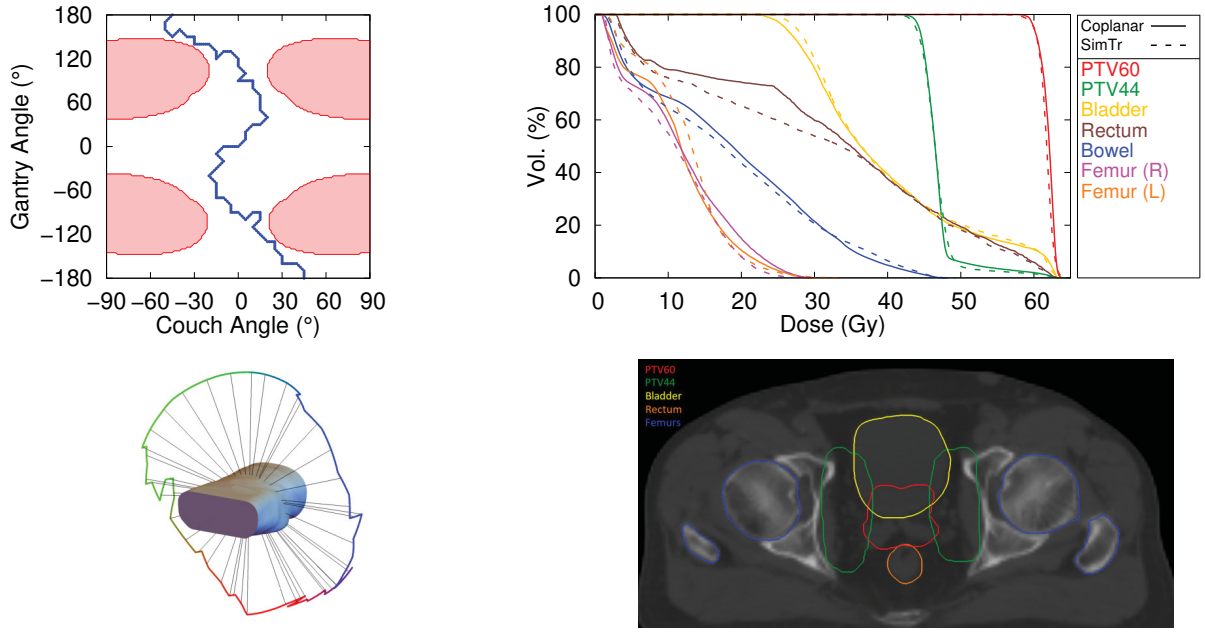

Figure 6.4 SimTr-VMAT treatment plan optimization for a prostate patient. Top left: the final optimized trajectory is shown in blue, and collision zones are shaded in red; top right: dose-volume histogram comparison between the coplanar VMAT plan (solid) and the simTr-VMAT plan (dashed); bottom left: 3D visualization of the patient anatomy and the final optimized trajectory. The colour scale is shown only to guide the eye; bottom right: patient anatomy.

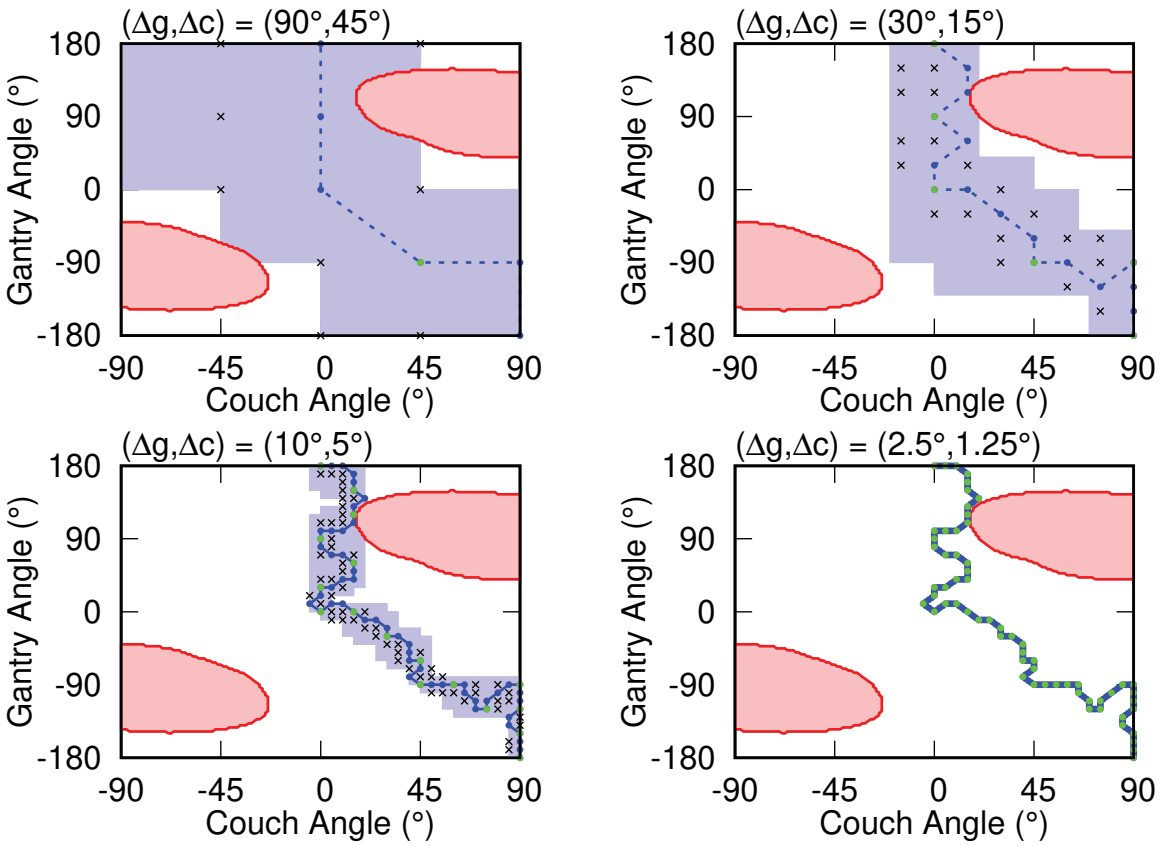

Figure 6.5 Trajectory optimization progression for the glioblastoma patient. The beam orientations from the previous grid resolution act as new trajectory segment endpoints and are shown as green dots. Beam orientations added to the trajectory path are shown as blue dots, forbidden collision regions are shaded red, and beam orientations considered but not selected through the pricing problem are shown as black points. The shaded blue area depicts the extent of the potential trajectories based on the endpoints defined at the previous grid resolution.

Table 6.1 Dose-volume parameters for target and critical structures for each of the simTr-VMAT treatment plans and the corresponding coplanar VMAT treatment plans. $D_{X\%}$: dose delivered to X% of the structure volume; D_{max}: maximum point dose delivered to structure; D_{mean}: mean dose delivered to structure; V_{YGy}: percentage of structure volume receiving at least Y Gy; $V_{Z\%}$: percentage of structure volume receiving at least Z% of the prescription dose.

Lung	simTr-VMAT			Coplanar VMAT		
Structure	$D_{95\%}$ (Gy)	$D_{98\%}$ (Gy)	D_{max} (Gy)	$D_{95\%}$ (Gy)	$D_{98\%}$ (Gy)	D_{max} (Gy)
PTV	48.00	47.54	58.01	48.00	47.20	56.41
	D_{mean} (Gy)	D_{max} (Gy)	V_{5Gy} (%)	D_{mean} (Gy)	D_{max} (Gy)	V_{5Gy} (%)
Heart	2.84	56.03	14.38	4.04	52.15	31.70
Esophagus	1.27	8.39	5.14	1.23	7.92	7.44
Ribs	11.36	50.63	66.90	12.97	50.84	66.75
	D_{mean} (Gy)	V_{20Gy} (%)	V_{5Gy} (%)	D_{mean} (Gy)	V_{20Gy} (%)	V_{5Gy} (%)
Lung (L)	4.45	4.94	20.79	5.47	8.09	26.72
Lung (R)	0.69	0.00	0.05	1.20	0.00	2.84
Lungs-ITV	2.06	1.67	8.38	2.78	3.00	12.50
Glioblastoma	simTr-VMAT			Coplanar VMAT		
Structure	$D_{95\%}$ (Gy)	$V_{95\%}$ (%)	D_{max} (Gy)	$D_{95\%}$ (Gy)	$V_{95\%}$ (%)	D_{max} (Gy)
PTV	58.16	96.38	66.96	57.07	95.11	64.25
	D_{mean} (Gy)	D_{max} (Gy)		D_{mean} (Gy)	D_{max} (Gy)	
Optic Apparatus	41.72	53.35		39.02	51.23	
Cochlea (R)	48.64	54.62		49.29	56.80	
Cochlea (L)	8.23	9.14		6.02	7.47	
Pituitary	43.90	52.40		43.28	54.54	
Eye (L)	5.94	12.34		9.87	17.49	
Eye (R)	19.34	36.59		26.00	52.40	
Lens (L)	2.93	3.29		7.47	8.99	
Lens (R)	8.38	12.12		12.52	14.08	
Brainstem	28.61	59.95		27.42	58.97	
Temporal Lobe (L)	13.61	27.69		15.63	33.39	
Nose	12.33	35.28		14.55	41.02	
Prostate	simTr-VMAT			Coplanar VMAT		
Structure	$D_{95\%}$ (Gy)	D_{max} (Gy)		$D_{95\%}$ (Gy)	D_{max} (Gy)	
PTV60	60.00	64.46		60.00	64.03	
PTV44	43.86	64.46		44.30	63.85	
	V_{60Gy} (%)	V_{52Gy} (%)	V_{48Gy} (%)	V_{60Gy} (%)	V_{52Gy} (%)	V_{48Gy} (%)
Bladder	11.13	18.42	22.71	10.74	16.85	21.06
Rectum	5.31	15.78	20.93	5.96	16.30	22.38
	D_{max} (Gy)			D_{max} (Gy)		
Femur (L)	34.43			30.21		
Femur (R)	29.69			29.35		

Table 6.2 Dose-volume parameters for target and critical structures for each of the simTr-VMAT treatment plans and the corresponding coplanar VMAT treatment plans. $D_{X\%}$: dose delivered to X% of the structure volume; D_{max}: maximum point dose delivered to structure; D_{mean}: mean dose delivered to structure; V_{YGy}: percentage of structure volume receiving at least Y Gy; $V_{Z\%}$: percentage of structure volume receiving at least Z% of the prescription dose.

Lung		Difference	
Structure	$\Delta D_{95\%}$ (Gy)	$\Delta D_{98\%}$ (Gy)	ΔD_{max} (Gy)
PTV	0.00	0.34	1.60
	ΔD_{mean} (Gy)	ΔD_{max} (Gy)	ΔV_{5Gy} (%)
Heart	-1.20	3.88	-17.32
Esophagus	0.04	0.47	-2.30
Ribs	-1.61	-0.21	0.15
	ΔD_{mean} (Gy)	V_{20Gy} (%)	ΔV_{5Gy} (%)
Lung (L)	-1.02	-3.15	-5.93
Lung (R)	-0.51	0.00	-2.79
Lungs-ITV	-0.72	-1.33	-4.12
Glioblastoma		Difference	
Structure	$\Delta D_{95\%}$ (Gy)	$\Delta V_{95\%}$ (%)	ΔD_{max} (Gy)
PTV	1.09	1.27	2.71
	ΔD_{mean} (Gy)	ΔD_{max} (Gy)	
Optic Apparatus	2.70	2.12	
Cochlea (R)	-0.65	-2.18	
Cochlea (L)	2.21	1.67	
Pituitary	0.62	-2.14	
Eye (L)	-3.93	-5.15	
Eye (R)	-6.66	-15.81	
Lens (L)	-4.54	-5.70	
Lens (R)	-4.14	-1.96	
Brainstem	1.19	0.98	
Temporal Lobe (L)	-2.02	-5.70	
Nose	-2.22	-5.74	
Prostate		Difference	
Structure	$\Delta D_{95\%}$ (Gy)	ΔD_{max} (Gy)	
PTV60	0.00	0.43	
PTV44	-0.44	0.61	
	ΔV_{60Gy} (%)	ΔV_{52Gy} (%)	ΔV_{52Gy} (%)
Bladder	0.39	1.57	1.65
Rectum	-0.65	-0.52	-1.45
	ΔD_{max} (Gy)		
Femur (L)	4.22		
Femur (R)	0.34		

the contralateral lung mean dose of 0.5 Gy and in the ipsilateral lung mean dose and V_{20Gy} of 1 Gy and 3%, respectively.

Glioblastoma

The trajectory optimization yielded a 360° gantry arc. The first half of the trajectory includes delivery through the left (contralateral) lobe, followed by an increasing couch rotation from 0° to 90° over the final 180° of gantry rotation, resulting in approximately orthogonal delivery angles to the target volume for the two halves of the trajectory arc. Compared to the coplanar VMAT treatment plan, the simTr-VMAT dose distribution exhibits improved coverage of the PTV ($D_{95\%}$ increased by 1 Gy), and increased sparing of most critical structures. Notably, a substantial decrease in D_{max} to the ipsilateral right eye, lens and cochlea of 16 Gy, 2 Gy, and 2 Gy, was achieved, respectively. Similarly, D_{max} to the contralateral left eye and lens was reduced by 5 Gy. The mean and maximum dose to the contralateral temporal lobe was reduced by 2 Gy and 5.7 Gy, respectively. Overall, a large reduction in the mean dose of 2 Gy to 7 Gy to the anterior area of the patient including the eyes and nose was observed.

Prostate

The resultant simTr-VMAT trajectory consisted of a 360° gantry rotation with a couch rotation angle varying between ±45°. The simTr-VMAT dose distribution demonstrated only minor reductions in OAR dose compared to the clinical plan.

6.4.2 Random Trajectories

Quality Assessment

The final objective function value following a treatment plan optimization is a measure of the adherence to the planning constraints by the treatment plan. For optimizations using the column generation approach, the objective function value will exhibit a dependence on the number of apertures included in the treatment plan; due to the nature of the pricing problem, only apertures with a positive price that will result in a decrease in the objective function value can be constructed. Comparing the random trajectories based solely on the objective function value is insufficient because some treatment plans may have a decreased objective function value as a result of a long, inefficient trajectory that is clinically impractical. Fig. 6.6 shows the average objective function value as a function of the number of control points that comprise the trajectory, for the 5000

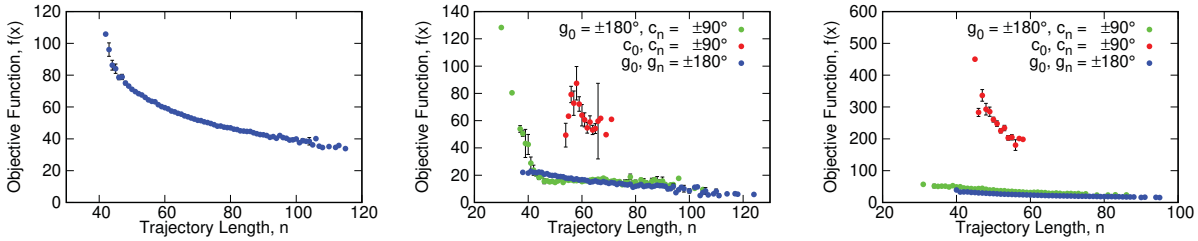

Figure 6.6 Average objective function value as a function of trajectory length for 5000 randomly generated trajectories. Error bars indicate the standard error of the mean. Left: glioblastoma patient; middle: lung patient; right: prostate patient. For the lung and prostate patient, the trajectories were separated into three different forms: i) endpoints with gantry angle at ±180°; ii) endpoints with couch angle at ±90°; iii) one endpoint at gantry angle of ±180° and one endpoint at couch angle of ±90°.

randomly generated trajectories for each of the patient cases. For the lung and prostate patients, due to the locations of the forbidden regions on the gantry-couch grid, three distinct trajectory forms were observed, with the trajectory endpoints at i) gantry angles of ±180°, ii) at couch angles of ±90°, or iii) with one endpoint at a gantry angle of ±180° and the other endpoint at a couch angle of ±90°. For these patient cases, the average behaviour for each trajectory form is depicted in Fig. 6.6, each exhibiting a distinct dependence on the trajectory length, especially for trajectories with endpoints at couch angles of ±90°.

To quantify the quality of a trajectory, the following equation was used:

$$Q = fL \tag{6.9}$$

where the quality Q for given a trajectory is given as the product of its objective function f and the trajectory length L (defined as the number of control points comprising the trajectory). The product of f and L is minimized for short trajectories with low objective function value while penalizing long, inefficient trajectories.

Fig. 6.7 shows the distribution of Q for each patient, as well as a colour map depicting the average Q for each beam orientation over all of the randomly generated trajectories. The Q values were shifted and normalized to have a minimum value of 0 and maximum value of 1. For some trajectories, the Q values were substantially greater than the rest of the random trajectories, either due to endpoints with couch angles at ±90° resulting in poor angular sampling, or traversal of unfavourable beam orientations. These trajectories were removed from the histogram data (222 trajectories were excluded for the lung patient, zero trajectories were excluded for the glioblastoma patient, and 218 trajectories were excluded for the prostate patient). The Q scores for the simTr-

VMAT and coplanar VMAT treatment plans (37×37 grid resolution) were calculated, with the corresponding bins indicated in the Q distribution. The simTr-VMAT trajectory is overlaid on the map and coloured to depict the optimization weight for the corresponding control point. The distribution of aperture optimization weights is shown below the colour map, with the colour of each column providing a reference for the trajectory segments.

For the lung patient, the randomly generated trajectories were binned based on their Q score, between 0.0 and 0.9 with bin width $\Delta Q = 0.1$. The gantry-couch coordinates for the trajectories in each bin were projected onto a downsampled 19×19 grid, with the frequency scored for trajectories traversing each grid coordinate. For each bin, a representative trajectory was randomly selected. Fig. 6.8 shows the frequency maps and representative trajectory for each bin. Each of the representative trajectories shown were reoptimized at an increased grid resolution (73×73 grid, corresponding to $(\Delta g, \Delta c) = (5.0^\circ, 2.5^\circ)$). The Q scores were recalculated, and compared against the previous Q scores in Fig. 6.9.

6.5 Discussion

In this work, the methodology for a simultaneous trajectory and VMAT optimization algorithm was delineated. The performance of this algorithm was validated through comparisons to randomly generated trajectories, representing the solution space for the trajectory optimization problem, as well as with comparisons to the coplanar VMAT treatment plans.

The simTr-VMAT treatment plans for the lung and brain patients demonstrated improvements compared to the coplanar VMAT treatment plans. These patients were included in the study for a combination of their complex geometrical arrangement of critical structures near the target volume, freedom for diverse gantry/couch beam orientations, and potential benefit from noncoplanar delivery. The use of simTr-VMAT optimization in the lung case substantially reduced the heart mean dose by 1.2 Gy for a similar target coverage as the coplanar VMAT treatment plan. Rates of major coronary heart events have been shown to increase linearly with increasing dose, by 7.4% per Gy, demonstrating the importance of reducing dose to the heart [19, 20]. The mean dose to the ipsilateral lung and Lungs-ITV was reduced by approximately 1 Gy, shown to be associated with reducing the risk of radiation pneumonitis [21, 22]. For the brain case, sparing of the frontal area (eyes and nose) and of the contralateral temporal lobe was achieved, showing a mean dose reduction between 2 Gy to 7 Gy to the eyes, lenses, nose and left temporal lobe. Due to the overlap between the brainstem and optic apparatus with the PTV, a minimum dose was required to these structures (60 Gy for brainstem and 54 Gy for optic apparatus). In the simTr-VMAT plan,

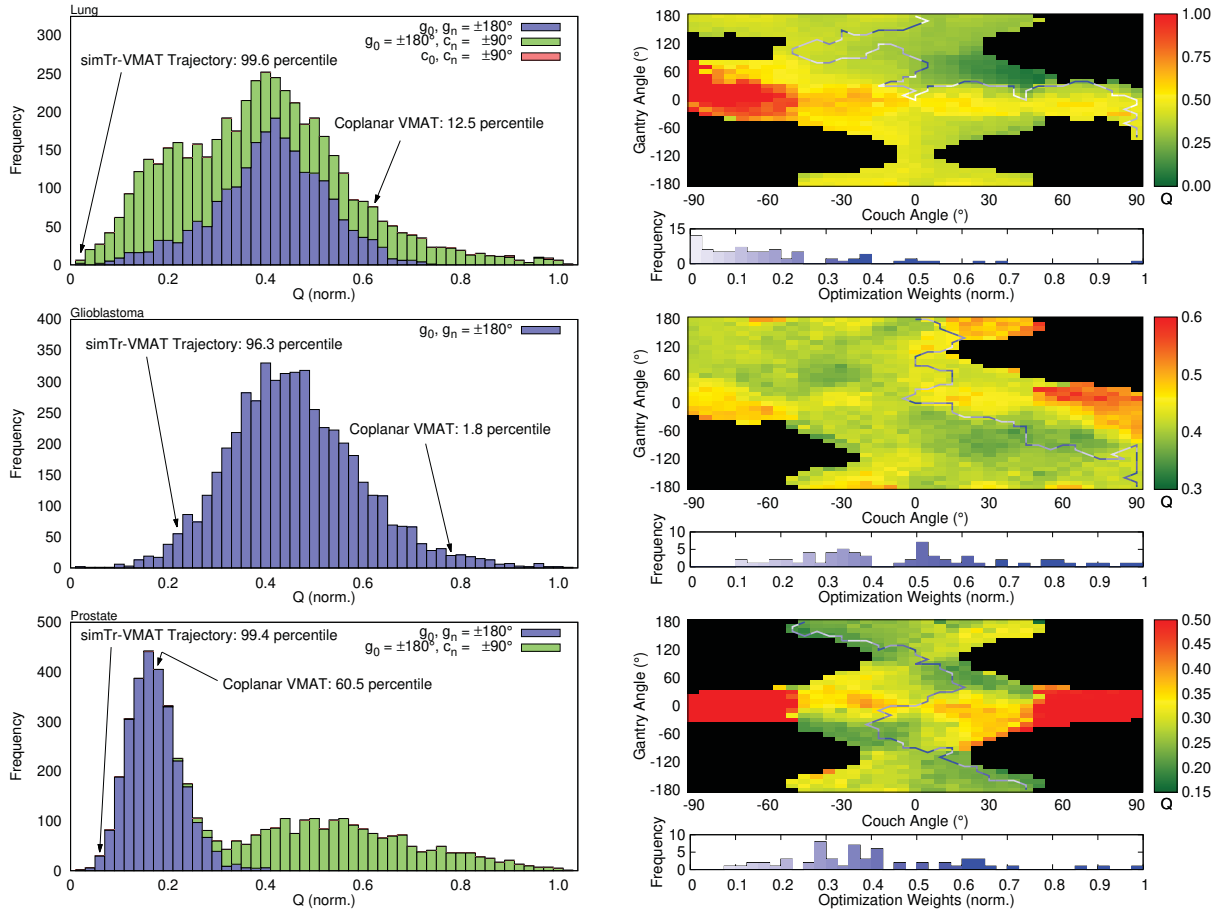

Figure 6.7 Left: histograms of normalized Q of 5000 randomly generated trajectories. Trajectories with different endpoints are denoted by their colour; right: For each beam orientation, the average Q over all randomly generated trajectories was calculated and shown in colour scale. The aperture optimization weight is indicated by the colour of each segment in order to emphasize any dependence with favourable regions of the colour map. The histogram below each colour map shows the distribution of optimization weights (normalized) for the simTr-VMAT treatment plan, and the colour of each column corresponds to the trajectory segments in the colour map. Top: lung, middle: glioblastoma; bottom: prostate. Black regions denote either forbidden collision zones or beam orientations that were not sampled in any of the random trajectories.

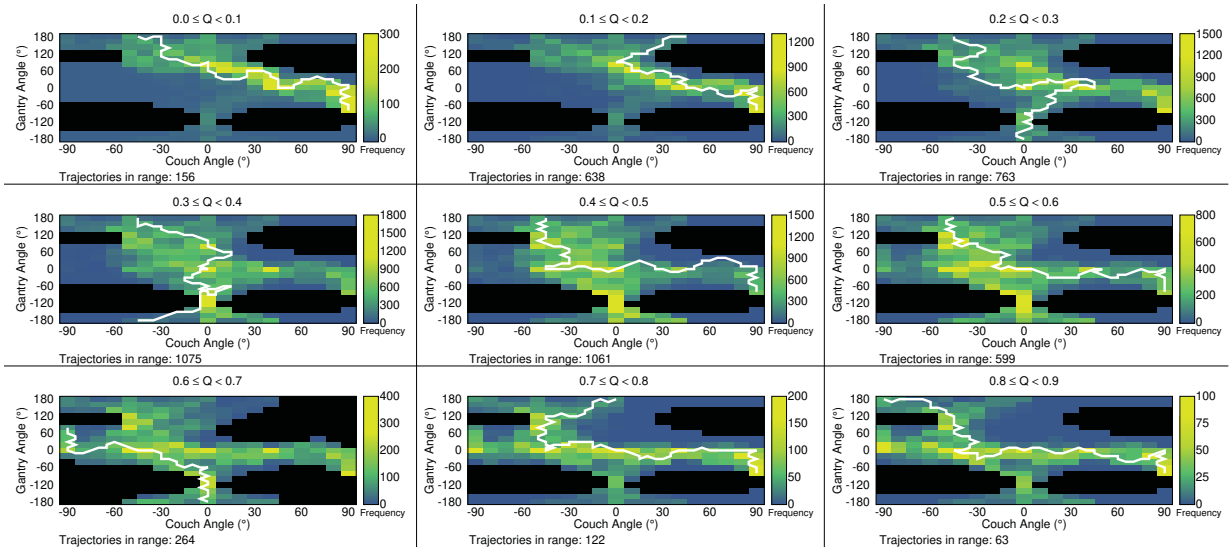

Figure 6.8 The distribution of Q scores for the lung patient were binned into ranges between $0.0 < Q < 0.9$, with bin width $\Delta Q = 0.1$. The beam orientations forming the trajectory path for the plans in each bin were projected onto a downsampled 19×19 gantry-couch coordinate grid, recording the frequency that each coordinate was traversed. The frequency maps are shown for each Q bin, with white lines showing a randomly selected representative trajectory.

the maximum dose to these structures was higher by 1 Gy to 2 Gy compared to the clinical plan, which allowed for better PTV coverage ($D_{95\%}$ higher by 1 Gy), while respecting the departmental maximum dose constraints to these OARs. Though the prostate patient features a complex geometry, the position of the target volume in the patient limits the angular freedom, and thus the potential benefit from noncoplanar delivery. The advantage of noncoplanar delivery for prostate treatments has been previously demonstrated in the literature [11, 23, 24], but the inclusion of pelvic lymph nodes in the target volume, combined with the single-arc simTr-VMAT trajectory, prevented dosimetric improvements compared to the three-arc coplanar VMAT treatment plan.

To quantify the performance of the simTr-VMAT optimized trajectories, a quality index Q for a given trajectory was defined to account for the dependence of the objective function value on trajectory length, in order to prefer shorter, efficient trajectories. Using this quality index, the simTr-VMAT optimized trajectories for lung, glioblastoma, and prostate patients ranked at the 99.6th, 96.3th, and 99.4th percentile when compared against 5000 randomly generated trajectories, respectively. The advantage of noncoplanar delivery for each patient case was demonstrated by the ranking of the two-arc coplanar VMAT treatment plans optimized on the 37×37 grid, at the 12.5th, 1.8th, and 60.5th percentiles for the lung, glioblastoma, and prostate patient, respectively.

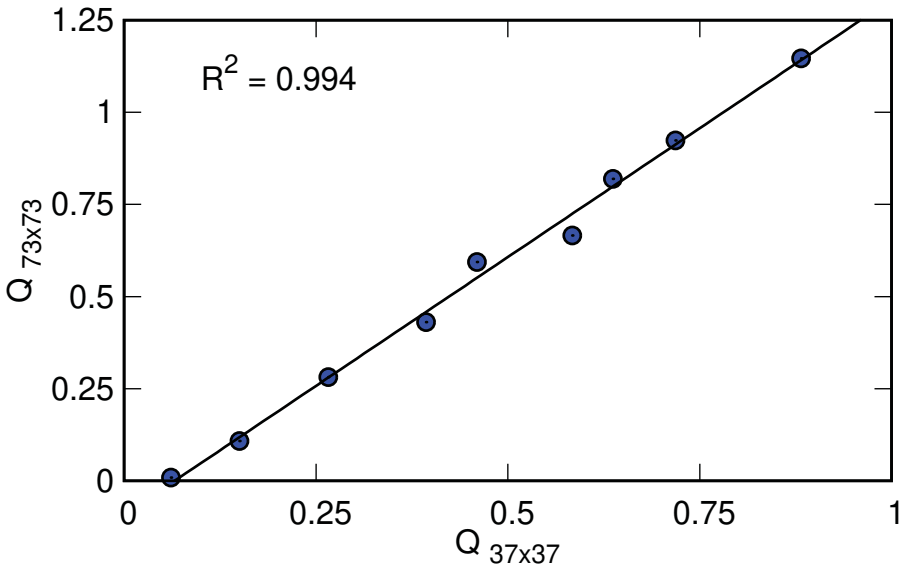

Figure 6.9 The representative trajectories shown in Fig. 6.8 were reoptimized at an increased gantry-couch grid spacing ((Δg, Δc) = (5.0°, 2.5°), corresponding to a 73×73 gantry-couch coordinate grid). The Q scores for the reoptimized plans were plotted against the previously calculated Q scores. The best fit line shown resulted in a coefficient of determination (R^2) equalling 0.994.

For the prostate patient, the low ranking of the coplanar VMAT plan (60.5th percentile) compared to the simTr-VMAT plan (99.4 percentile) was not consistent with the dosimetric comparison of the final treatment plans. This discrepancy is attributed to the increased number of control points for the three-arc coplanar VMAT plan (534 control points) compared to the simTr-VMAT plan (229 control points), as well as potential differences due to the optimization through the Eclipse treatment planning system. The regularity of the Q distributions, without substantial variability across histogram bins, suggests an adequate sample size. The distributions for the lung and prostate patients exhibited multimodal behaviour for the distinct trajectory forms. For the lung patient, the mixed gantry/couch angle endpoint form (one endpoint at a gantry angle of $\pm 180^\circ$ and the other endpoint at a couch angle of $\pm 90^\circ$) resulted in a broader distribution than the gantry angle endpoint trajectory form, but with a similar maximum. The distribution for the prostate patient illustrated the benefit of full 360° gantry rotations compared to the other trajectory forms.

Colour maps were generated for each patient indicating regional dependence of the objective function value for the randomly generated trajectories. Although the final trajectories do not exclusively traverse favourable regions of the colour maps shown in Fig. 6.7, this condition is not necessary to yield clinically beneficial treatment plans. For the lung patient, the incidence of low optimization weights for control points situated in unfavourable regions suggests their diminishing importance as the simTr-VMAT optimization proceeded. For each patient case, there may exist trajectories that are more efficient than the simTr-VMAT trajectories, but they would be challenging to identify without prior knowledge of the solution space. Fig. 6.8 depicts the behaviour of the trajectories within different Q bins for the lung patient, showing common trajectory path features, especially for trajectories at low or high Q values. The frequently traversed regions indicated by the $0.0 \leq Q < 0.1$ bin share similarities with the simTr-VMAT trajectory.

The random trajectories were generated on a 37×37 grid, with a final gantry-couch grid resolution of $(\Delta g, \Delta c) = (10^\circ, 5^\circ)$, under the assumption that progression to a higher grid resolution would not substantially alter the relative ranking of the simTr-VMAT plans compared to the set of random trajectories. The gantry/couch spacing between adjacent control points is consistent with Dong *et al.* and Lyu *et al.* [10, 11]. Performing a similar analysis at a higher grid resolution becomes computationally infeasible, requiring a large amount of precalculated beamlet doses for each patient (on the order of 4 million), and increasing the optimization time for each trajectory. The representative trajectories indicated in the different Q bins in Fig. 6.8 were reoptimized at an increased grid resolution to support the assumption that the random trajectory validation results would be maintained at a finer control point spacing. The correlation between the corresponding

Q scores in Fig. 6.9 provides evidence that the Q scores indicate the quality of a trajectory path independent of the number of control points comprising the trajectory.

The development of the simTr-VMAT algorithm required several seemingly *ad hoc* decisions regarding details of the optimization algorithm. The progression of the grid resolution was chosen in order to balance between sampling of the angular space, and maintaining computational feasibility. The extent of the angular sampling for the glioblastoma case is indicated by the blue shaded regions in Fig. 6.5. For the first three resolution levels, the trajectory paths between adjacent trajectory segment endpoints are determined on a grid no larger than 5×5. Though the trajectory determined at the initial resolution level dictates the overall shape of the final trajectory, control points at the subsequent resolution level are identified between trajectory segment endpoints spanning up to 90° in gantry angle, and 45° in couch angle.

The beam orientation selected to initialize the simTr-VMAT optimization influences the final treatment plan quality. The method adopted to make this selection is based on initial pricing of several candidate beam orientations with zero patient dose distribution. The first-order perturbation of beamlet doses on the upper dose limit constraints under these conditions have no net contribution to the price, resulting in an aperture shape dependent solely on the lower dose limit constraints (*i.e.* the target volume constraints). This procedure results in favouring the beam orientation with the greatest number of beamlets intersecting the target volume. Alternatively, an experienced physician or treatment planner could select an initial beam orientation deemed most beneficial. Comparisons of the simTr-VMAT dose distributions to the coplanar VMAT dose distributions for the cases studied as well as the correspondence with the highest-scoring randomly generated trajectories indicates that the initial beam orientation chosen as well as the determination of the trajectory at the coarse grid resolution level is justified.

The final iteration behaviour, linearly adding control points between existing trajectory segment endpoints at a resolution of $(\Delta g, \Delta c) = (2.5°, 1.25°)$, was decided upon as a consideration for computational tractability, dose delivery accuracy, and patient comfort. Linearly connecting during the final iteration ensures that couch and gantry rotations occur monotonically over a minimum range of 10° (gantry) and 5° (couch).

Conventional VMAT treatment plans often define control points every 2° of gantry rotation, resulting in a total of 180 control points for a full 360° coplanar delivery, with additional arcs increasing this total. With the final grid resolution shown in this work, the simTr-VMAT plans were comprised of 297, 245, and 229 control points for the lung, glioblastoma, and prostate patients, respectively, comparable to the coplanar VMAT treatment plans (212, 228, and 534 control points for the lung, glioblastoma, and prostate patients, respectively).

The treatment planning process, iteratively adjusting the dose-volume constraints based on the optimized dose distribution, was performed primarily at the $(\Delta g, \Delta c) = (10^\circ, 5^\circ)$ grid resolution prior to completing the full optimization at the final grid resolution of $(\Delta g, \Delta c) = (2.5^\circ, 1.25^\circ)$. The optimization time is dependent on the number of voxels comprising the dose calculation volume and the number of control points comprising the trajectory, and was measured for the initial treatment planning phase as 10 minutes for both the lung and prostate patients, and 2.5 minutes for the glioblastoma patient. The time to complete the optimization at the final grid resolution was 3 hours, 0.75 hours, and 6 hours for the lung, glioblastoma, and prostate patients, respectively. Beamlet doses required an initial calculation of approximately 3 hours, 1 hour, and 4 hours for the lung, glioblastoma, and prostate patients, respectively, prior to treatment planning. The treatment delivery time was estimated for the final treatment plans based on the nominal maximum dose rate and speeds for the relevant mechanical components of a TrueBeam linear accelerator, equalling: 4:56, 9:08, and 4:48 for the lung, glioblastoma, and prostate patients, respectively.

6.6 Conclusion

The work presented in this paper outlines the methodology for a trajectory-based treatment planning optimization algorithm that generates a gantry-couch trajectory simultaneous with VMAT treatment plan optimization. The optimization algorithm was applied to three patient cases and compared favourably against coplanar VMAT treatment plans, and validated through comparisons to randomly generated trajectories representing the solution space for the trajectory optimization problem. The performance of the simTr-VMAT optimization methodology under these conditions demonstrates the potential as a clinically-relevant treatment planning optimization framework.

6.7 Appendix: Supplementary Material

Table 6.3 Treatment plan optimization constraints used for lung patient.

Structure	Dose (Gy)	Volume (%)	Weight
Target Constraints			
PTV (lower)	50.0	100.0	5.0
PTV (upper)	56.8	0.0	5.0
ITV (lower)	53.0	100.0	5.0
ITV (upper)	56.8	0.0	5.0
OAR Constraints			
Lung (L)	1.0	33.0	5.0
	4.0	23.0	5.0
	6.0	15.0	8.0
	10.0	5.0	8.0
	20.0	2.0	7.0
	30.0	1.0	5.0
Lung (R)	1.0	17.0	5.0
	3.0	4.0	5.0
Heart	6.0	5.0	7.0
	10.0	3.0	7.0
	15.7	0.2	7.0
	27.2	0.0	7.0
Chest Wall	12.0	23.0	4.0
	26.0	1.0	4.0
Ribs	10.0	40.0	5.0
Esophagus	2.0	15.0	5.0
Spinal Cord	5.0	0.0	8.0
Ring	20.0	58.0	4.0
	43.0	0.0	4.0
Post Avoid	0.0	9.0	5.0

Table 6.4 Treatment plan optimization constraints used for glioblastoma patient.

Structure	Dose (Gy)	Volume (%)	Weight
Target Constraints			
PTV (lower)	60.0	0.0	16.0
PTV (upper)	60.0	100.0	16.0
PTV + Optic App (PRV) (upper)	50.5	100.0	14.0
PTV + Optic App (PRV) (lower)	50.5	0.0	14.0
PTV + Brainstem (PRV) (upper)	57.0	100.0	9.0
PTV + Brainstem (PRV) (lower)	57.0	0.0	9.0
OAR Constraints			
Brainstem (PRV)	15.0	55.0	8.0
	45.0	18.0	8.0
	56.0	0.0	8.0
Optic App (PRV) – PTV	30.0	55.0	20.0
	45.0	28.0	20.0
	50.5	0.0	20.0
Optic App (PRV)	50.5	0.0	20.0
Optic Chiasm	50.0	0.0	8.0
Optic Nerve (R)	50.5	0.0	7.0
Eye (R)	35.0	0.0	9.0
	40.0	8.0	9.0
Eye (L)	7.0	14.0	9.0
	12.0	0.0	9.0
Lens (R)	7.0	0.0	7.0
Lens (L)	2.0	0.0	7.0
Temporal Lobe (L)	17.5	13.0	10.0
	27.0	0.0	10.0
Cochlea (R)	50.0	0.0	8.0
Cochlea (L)	8.0	0.0	8.0
Pituitary	40.0	66.0	8.0
	43.0	50.0	8.0
	53.0	0.0	8.0
Ring 1	40.0	80.0	10.0
	50.0	60.0	10.0
	60.0	0.0	10.0
Ring 2	40.0	20.0	15.0
	43.0	9.0	10.0
	50.0	0.0	10.0
Avoid	10.0	0.0	7.0
Nose	20.0	0.0	5.0

Table 6.5 Treatment plan optimization constraints used for prostate patient.

Structure	Dose (Gy)	Volume (%)	Weight
Target Constraints			
PTV60 (lower)	60.0	100.0	12.0
PTV60 (upper)	60.0	0.0	12.0
PTV44 (lower)	45.0	100.0	9.0
PTV44 (upper)	46.0	100.0	9.0
OAR Constraints			
Femur (L)	10.0	60.0	5.0
	15.0	22.0	4.0
	16.0	12.0	4.0
Femur (R)	15.0	20.0	4.0
	20.0	10.0	4.0
Bladder	30.0	52.0	5.0
	35.0	29.0	5.0
	40.0	5.0	5.0
Rectum	10.0	68.0	5.0
	20.0	65.0	5.0
	30.0	45.0	5.0
	45.0	20.0	5.0
	50.0	6.0	5.0
Cauda Equina	20.0	0.0	3.0
Sigmoid - PTV	30.0	30.0	5.0
	30.0	0.0	5.0
Bowel - PTV	5.0	65.0	5.0
	20.0	30.0	5.0
	30.0	7.0	5.0
	38.0	0.0	5.0
Ring 60	55.0	10.0	5.0
	57.0	7.0	5.0
	58.5	0.0	5.0
Ring 44 (1)	40.0	40.0	5.0
	42.0	0.0	5.0
Ring 44 (2)	30.0	40.0	5.0
	40.0	0.0	5.0
Normal	10.0	20.0	5.0
	30.0	0.0	7.0

References

[1] Y. Yang, P. Zhang, L. Happersett, J. Xiong, J. Yang, M. Chan, K. Beal, G. Mageras, and M. Hunt, "Choreographing couch and collimator in volumetric modulated arc therapy," Int. J. Radiat. Oncol., Biol., Phys. **80**, 1238–1247 (2011).

[2] G. Smyth, J. C. Bamber, P. M. Evans, and J. L. Bedford, "Trajectory optimization for dynamic couch rotation during volumetric modulated arc therapy," Phys. Med. Biol. **58**, 8163–8177 (2013).

[3] R. L. MacDonald and C. G. Thomas, "Dynamic trajectory-based couch motion for improvement of radiation therapy trajectories in cranial SRT," Med. Phys. **42**, 2317–2325 (2015).

[4] M. K. Fix, D. Frei, W. Volken, D. Terribilini, S. Mueller, O. Elicin, H. Hemmatazad, D. M. Aebersold, and P. Manser, "Part 1: Optimization and evaluation of dynamic trajectory radiotherapy," Med. Phys. **45**, 4201–4212 (2018).

[5] M. Langhans, J. Unkelbach, T. Bortfeld, and D. Craft, "Optimizing highly noncoplanar VMAT trajectories: the NoVo method," Phys. Med. Biol. **63**, 025023 (2018).

[6] D. Papp, T. Bortfeld, and J. Unkelbach, "A modular approach to intensity-modulated arc therapy optimization with noncoplanar trajectories," Phys. Med. Biol. **60**, 5179–5198 (2015).

[7] E. Wild, M. Bangert, S. Nill, and U. Oelfke, "Noncoplanar VMAT for nasopharyngeal tumors: Plan quality versus treatment time," Med. Phys. **42**, 2157–2168 (2015).

[8] B. Wilson, K. Otto, and E. Gete, "A simple and robust trajectory-based stereotactic radiosurgery treatment," Med. Phys. **44**, 240–248 (2017).

[9] G. Smyth, P. M. Evans, J. C. Bamber, and J. L. Bedford, "Recent developments in non-coplanar radiotherapy," Br. J. Radiol. **92** (2019).

[10] P. Dong, H. Liu, and L. Xing, "Monte Carlo tree search-based non-coplanar trajectory design for station parameter optimized radiation therapy (SPORT)," Phys. Med. Biol. **63**, 135014 (2018).

[11] Q. Lyu, V. Y. Yu, D. Ruan, R. Neph, D. O'Connor, and K. Sheng, "A novel optimization framework for VMAT with dynamic gantry couch rotation," Phys. Med. Biol. **63**, 125013 (2018).

[12] H. E. Romeijn, R. K. Ahuja, J. F. Dempsey, and A. Kumar, "A column generation approach to radiation therapy treatment planning using aperture modulation," SIAM J. Optim. **15**, 838–862 (2005).

[13] F. Peng, X. Jia, X. Gu, M. A. Epelman, H. E. Romeijn, and S. B. Jiang, "A new column-generation-based algorithm for VMAT treatment plan optimization," Phys. Med. Biol. **57**, 4569–4588 (2012).

[14] M.-A. Renaud, M. Serban, and J. Seuntjens, "On mixed electron-photon radiation therapy optimization using the column generation approach," Med. Phys. **44**, 4287–4298 (2017).

[15] V. Y. Yu, A. Tran, D. Nguyen, M. Cao, D. Ruan, D. A. Low, and K. Sheng, "The development and verification of a highly accurate collision prediction model for automated noncoplanar plan delivery," Med. Phys. **42**, 6457–6467 (2015).

[16] E. Mainegra-Hing, D. W. Rogers, and I. Kawrakow, "Calculation of photon energy deposition kernels and electron point dose kernels in water," Med. Phys. **32**, 685–699 (2005).

[17] A. Wachter and L. T. Biegler, "On the Implementation of a Primal-Dual Interior Point Filter Line Search Algorithm for Large-Scale Nonlinear Programming," Mathematical Programming **106**, 25–57 (2006).

[18] D. W. O. Rogers, I. Kawrakow, J. P. Seuntjens, B. R. B. Walters, and E. Mainegra-Hing, "NRC user codes for EGSnrc," NRCC Report PIRS-702 (Rev. B) (2003).

[19] S. K. Darby, M. Ewertz, P. McGale, A. M. Bennet, U. Blom-Goldman, D. Brønnum, C. Correa, D. Cutter, G. Gagliardi, B. Gigante, M.-B. Jensen, and A. Nisbet, "Risk of ischemic heart disease in women after radiotherapy for breast cancer," N Engl J Med **368**, 987–998 (2013).

[20] F. van Nimwegen, M. Schaapveld, D. Cutter, C. Janus, A. Krol, M. Hauptmann, K. Kooijman, J. Roesink, R. van der Maazen, S. Darby, B. Aleman, and F. van Leeuwen, "Radiation dose-response relationship for risk of coronary heart disease in survivors of Hodgkin lymphoma," J. Clin. Oncol. **34**, 235–243 (2015).

[21] L. B. Marks, S. M. Bentzen, J. O. Deasy, F.-M. Kong, J. D. Bradley, I. S. Vogelius, I. El Naqa, J. L. Hubbs, J. Y. Lebesque, R. D. Timmerman, M. K. Martel, and A. Jackson, "Radiation dose-volume effects in the lung," Int. J. Radiat. Oncol., Biol., Phys. **76**, S70–S76 (2010).

[22] A. M. Allen, M. Czerminska, P. A. Jänne, D. J. Sugarbaker, R. Bueno, J. R. Harris, L. Court, and E. H. Baldini, "Fatal pneumonitis associated with intensity-modulated radiation therapy for mesothelioma," Int. J. Radiat. Oncol., Biol., Phys. **65**, 640–645 (2006).

[23] S. L. Sailer, J. G. Rosenman, J. R. Symon, T. J. Cullip, and E. L. Chaney, "The tetrad and hexad: maximum beam separation as a starting point for noncoplanar 3D treatment planning: prostate cancer as a test case," Int. J. Radiat. Oncol., Biol., Phys. **30**, 439–446 (1994).

[24] R. A. Price, G. E. Hanks, S. W. McNeeley, E. M. Horwitz, and W. H. Pinover, "Advantages of using noncoplanar vs. axial beam arrangements when treating prostate cancer with intensity-modulated radiation therapy and the step-and-shoot delivery method," Int. J. Radiat. Oncol., Biol., Phys. **53**, 236–243 (2002).

6.8 Clarifications after manuscript publication

- In the introduction of this manuscript, the presented simultaneous trajectory generation and VMAT optimization approach is described as distinct from the two-step approaches that have commonly been used in the literature. However, the objectives of this work were not to make direct comparisons to the two-step approaches, due to: i) there does not exist a standard clinical practice for trajectory-based optimization; ii) there are numerous challenges in satisfactorily implementing and validating a trajectory-based optimization approach from the literature for the means of comparing to the simTr-VMAT optimization algorithm. Instead, this observation motivated the implementation of the random trajectory validation approach as a means of independently evaluating the performance of the optimization algorithm.

- One of the purported benefits of the trajectory optimization approaches presented by Dong *et al.* and Lyu *et al.* was noted as the monotonically increasing couch rotation angle, which may help to ensure patient comfort and safety during the treatment delivery, as well as simplifying the optimization process for both methodologies [10, 11]. However, such an approach limits the complexity of the trajectories during the optimization process, which may result in inferior treatment plan quality. Additionally, the influence of couch rotation on patient comfort and delivery accuracy has been conclusively determined in the literature. Thus, in the simTr-VMAT approach, the trajectories are not limited to a monotonically increasing couch rotation angle in the interest of improved treatment plan quality.

- The software implementation of the simTr-VMAT algorithm was written in C++ to interface with an in-house optimization framework that uses the IPOPT library as the computational solver [17]. Beamlet dose calculations were performed using an in-house collapsed-cone convolution-superposition dose calculation algorithm, and final dose calculations were obtained through an in-house treatment planning system called Radify, which provides a front-end user interface for instantiating Monte Carlo dose calculations using EGSnrc [18].

- The coordinate system for the gantry and couch rotation angles was not explicitly described in this manuscript, but the coordinate system conventions used in this thesis can be seen in Fig. 4.5.

- In the description of collision zones in section 6.3.1, it is stated that candidate beam orientations lying within the restricted collision region are removed during the treatment plan optimization. As a clarification, these beam orientations are not considered during the pricing problem phase of the optimization in which candidate apertures are constructed. In the implementation, a two-dimensional array-based representation of the gantry-couch coordinate space is computed prior to the start of the optimization, in which each element contains a boolean value denoting the existence of the beam orientation within a collision region. During the optimization, this array is queried prior to proceeding to the pricing problem step for each candidate beam orientation.

- For the lung and glioblastoma patients, the coplanar VMAT treatment plans optimized using the clinical treatment planning system were not delivered clinically. For the prostate patient, the 3-arc coplanar VMAT plan was delivered clinically. In a previous version of the manuscript prior to publication, treatment plan comparisons were against the clinically delivered plans (for the glioblastoma patient: an intensity-modulated radiation therapy treatment plan; for the lung patient, a three-dimensional conformal radiation therapy treatment plan), but for a more consistent comparison to the simTr-VMAT optimization approach, coplanar VMAT plans were optimized for these patients.

- In the Discussion section, it is stated that the final treatment plan quality is dependent on the initial beam orientation selection. In the implementation of simTr-VMAT, there are up to 9 possible coordinates in the gantry/couch grid from which the initial beam orientation is chosen. The available candidate beam orientations as the optimization proceeds will be dependent on this selection, and will invariably result in a different trajectory path and

final treatment plan compared to an optimization that was initialized with a different beam orientation.

- The potential detriments of the chosen method for the selection of the initial beam orientation (through the pricing problem applied to the initial candidate beam orientations) is also addressed, as well as an alternative approach wherein a physician or treatment planner could make an informed selection. In order to train a user to make an informed selection of the initial beam orientation, it may be necessary to accrue statistics for different treatment sites on the initial beam orientation for the trajectory-based delivery, and provide recommendations based on this.

7

Delivery verification of trajectory-based treatment plans

Joel Mullins, Veng Heng, and Jan Seuntjens

Preface

With the development of the simTr-VMAT optimization methodology presented in the previous chapter, the complex trajectory paths resulting from the optimizations were regarded as potentially prohibitive to future clinical implementation. Research evaluating the dose delivery accuracy for trajectory-based treatment plans was scarce in the literature, leading to the objectives of this study: to verify the delivery accuracy for simTr-VMAT plans, and to implement a trajectory smoothing procedure to further assuage concerns about patient comfort and delivery accuracy during trajectory-based delivery.

7.1 Abstract

Purpose: The dose delivery accuracy for trajectory-based treatment plans has not been previously demonstrated. This work uses patient-specific quality assurance protocols to evaluate delivery accuracy for trajectory-based treatment plans, in addition to trajectories that have undergone a smoothing procedure to aid in delivery accuracy.

Methods: Trajectory-based treatment plans were obtained for three patient cases (lung, glioblastoma, prostate) based on previously published work (simTr-VMAT). During the optimization, a trajectory smoothing procedure was implemented that identified trajectory beam orientations that violated a smoothness criteria, and removed or repositioned the violating beam orientations. Repositioned apertures were reshaped prior to continuing the trajectory optimization using a simulated annealing approach. Treatment plans for the initially optimized (base) and smoothed trajectories were delivered on the TrueBeam or TrueBeam STx linear accelerators, with ionization chamber and radiochromic film measurements recorded. These measurements were compared against Monte Carlo dose calculations.

Results: The trajectory smoothing procedure yielded treatment plans of comparable quality to the initially optimized (base) treatment plans, although the smoothed trajectory objective functions were numerically increased compared to those of the base trajectory. The dose calculation measurements demonstrated a systematically lower dose compared to the ionization chamber measurements, with an average difference of (-3.5$\pm$2.0)%. The film dose measurements, when scaled based on the ionization chamber agreement, yielded gamma pass rates above 95% for the lung and glioblastoma smoothed trajectory deliveries, while the prostate smoothed trajectory had a pass rate of 89.2%. Each of the gamma pass rates were improved compared to the base trajectory delivery.

Conclusion: The smoothing procedure effectively reduced the instances of gantry or couch directional reversals without negatively impacting the treatment plan quality. The accuracy of the trajectory delivery, although within combined standard uncertainty, was not satisfactorily verified, but the film gamma pass rates for the smoothed trajectory plans indicate improved agreement between measurement and calculation compared to the base trajectory plans.

7.2 Introduction

Trajectory-based treatment delivery involves the coordinated motion of different mechanical components of a linear accelerator. Commonly, a series of gantry and couch rotation angles

define a noncoplanar trajectory, resulting in steeper dose gradients outside the target volume while avoiding irradation of critical structures, but dynamic collimator rotation may also be included [1–11].

There have been several approaches to trajectory-based treatment plan optimization presented in the literature, but few of these studies have investigated the accuracy of treatment delivery under these dynamic conditions. The management of positional uncertainty, specifically of the treatment couch, has instead been addressed through the treatment plan optimization approach, such as through the implementation of a monotonically increasing couch rotation angle during delivery [7, 8, 11], or by defining a series of arc segments at a static couch rotation angle [3].

In the interest of patient comfort, Wilson *et al.* implemented trajectory-based treatment plans including a monotonically increasing couch rotation angle, and evaluated the delivery accuracy with ionization chamber and radiochromic film measurements, as well as analysis of the trajectory log files associated with the delivery. The measurements demonstrated ionization chamber measurements within 2% of Eclipse AAA dose calculations, film gamma passing rates greater than 96% (criteria: 3 mm, 3%), and the root mean square error for the gantry and couch rotation angles on the order of 0.05°, supporting the claims of accurate treatment delivery under these conditions [11]. A second study by Wilson *et al.* performed trajectory log analysis for dynamic couch rotation, determining no clinically significant rotational error [12]. The work of Fix *et al.* provided an implementation for trajectory-based delivery with a monotonically increasing gantry rotation angle, while the couch rotation angle was determined through an A* pathfinding algorithm that permits reversals in the couch rotation direction during the trajectory. For one head and neck patient case, film measurements demonstrated greater than a 99% passing rate with a criteria of 2 mm and 2% [10].

In previous work, a trajectory optimization algorithm was outlined that in general does not preclude the potential for directional changes of the gantry or couch rotation angle during delivery [13]. The purpose of the present study is to deliver these trajectory-based treatment plans on a Varian TrueBeam linear accelerator (Varian Medical Systems, Palo Alto, CA, USA), and evaluate the dose delivery accuracy under these dynamic conditions. Additionally, a trajectory smoothing implementation is added to the optimization algorithm to reduce the instances of rotation directional changes, while maintaining the treatment plan quality of the original dynamic trajectory.

7.3 Materials and Methods

7.3.1 Trajectory-VMAT Optimization

The simultaneous trajectory generation and volumetric modulated arc therapy optimization algorithm (simTr-VMAT) [13] presented in previous work is based on the column generation approach [14–16], in which the treatment plan and trajectory path are simultaneously constructed through the iterative addition of multileaf collimator (MLC) apertures with an associated beam orientation corresponding to a gantry-couch coordinate. A feature of the optimization algorithm is a progressively increasing gantry-couch grid resolution on which the trajectories are formed, defining the gantry and couch angle spacing between adjacent control points comprising the trajectory. Following the completion of a trajectory at a given grid resolution, the optimization proceeds to refine the trajectory path at an increased grid resolution. To assuage concerns of delivery accuracy and patient comfort due to complicated, unsmoothed trajectories at a high gantry-couch grid resolution, the optimization algorithm was simplified at the final grid resolution ($(\Delta g, \Delta c) = (2.5^\circ, 1.25^\circ)$) to linearly connect between the previously defined control points, ensuring that the minimum arc segment has a length of 5° couch rotation or 10° gantry rotation.

7.3.2 Trajectory Smoothing

The trajectory smoothing methodology identifies control points that violate a simple smoothness criteria, and either repositions the control point on the discrete gantry-couch grid or removes it from the treatment plan (see Fig. 7.1). Control points were defined as violating if they resulted in an immediate reversal in the gantry or couch rotation direction. Smoothing was initially applied to violating control points based on the couch rotation angle, then subsequently applied with respect to the gantry rotation angle.

The repositioning of control points to a new beam orientation may result in an aperture shape that is not appropriate for the shifted patient geometry from the new beam's eye view, perturbing the treatment plan and worsening the objective function value. In order to recover the plan quality, a simulated annealing-based procedure was implemented. With each iteration, the active leaves for the repositioned apertures were candidates to be randomly repositioned, defining a new aperture shape and associated dose. The random change was retained if the reoptimized cost function value was reduced, or if an acceptance probability based on a cooling schedule was passed. This procedure was repeated for a total number of iterations equal to 500 times the number of repositioned apertures. The cooling schedule was defined as:

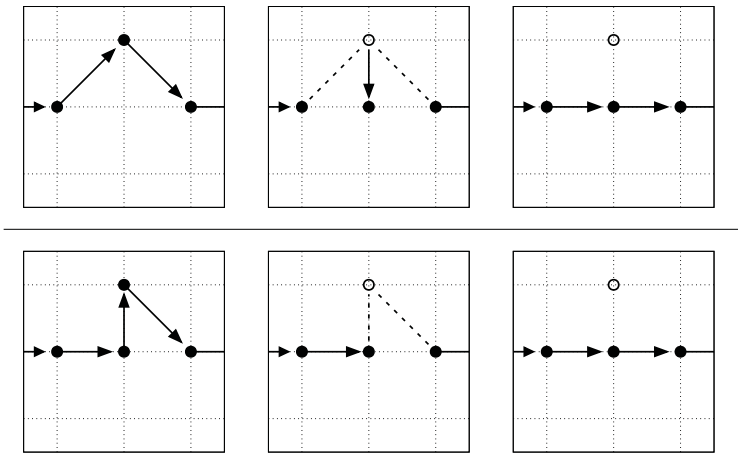

Figure 7.1 Trajectory smoothing is performed by repositioning violating beam orientations (top) or removal of the beam orientation from the treatment plan optimization (bottom).

$$t_k = \frac{t_0}{1 + \alpha k} \tag{7.1}$$

where t_k is the temperature at the kth iteration, with an initial temperature t_0 of 1.0, and α defined to be 0.1.

Due to the final grid resolution behaviour of the simTr-VMAT optimization algorithm, the trajectory smoothing procedure was implemented prior to the optimization at the final grid resolution, since any subsequent control points added to the trajectory will not violate any smoothness criteria.

7.3.3 Deliverable Arc Treatment Plan

The completion of a treatment plan optimization results in the specification of a series of control points with an associated gantry angle, couch angle, multileaf collimator aperture shape, and optimization weight (proportional to the monitor unit output). The treatment plan is effectively a step-and-shoot treatment plan with static MLC apertures, and must be converted into an arc-based delivery. This conversion is predicated on the assumption that the control point angular spacing is adequately fine that the radiation delivery over an arc segment rather than at a specific beam orientation will not substantially alter the dose distribution compared to the optimized dose. In the literature, clinically acceptable control point spacing has been demonstrated to be on the order of 2–3° (between gantry angles). [17–19]. To convert the optimization to an arc-based delivery,

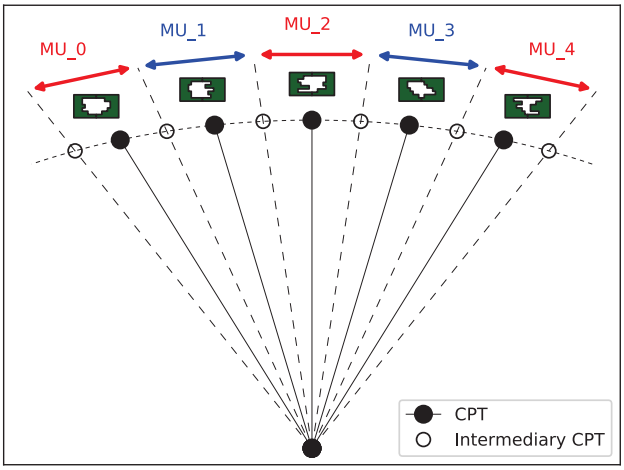

Figure 7.2 The output of a treatment plan optimization defines a series of aperture shapes with an associated MU weight, corresponding to a step-and-shoot delivery. For the conversion to an arc-based treatment plan, the aperture shapes were specified at the beam orientations for each control point, and intermediary control points were inserted to facilitate the treatment delivery. At the intermediary control point, the MLC apertures are interpolated between the adjacent control points, while the MU output specified for a given control point is delivered over the arc segment defined by the adjacent intermediary control points.

the aperture shapes were specified at the beam orientation associated with the control points, and intermediary control points were defined at the midpoint between adjacent control points, with the aperture shape specified as the linear interpolation between the adjacent aperture shapes. The monitor unit output specified for the original control point was delivered throughout the arc segment defined by the intermediary control points. Fig. 7.2 illustrates this procedure.

The optional research mode for the TrueBeam linear accelerator ("developer's mode") permits the custom specification of treatment plans in an XML-formatted file, as a series of control points defining the treatment planning parameters. The converted arc delivery was used to define the XML files to be used for the treatment delivery.

7.3.4 Patient Cases

The patients used in this study were a lung stereotactic body radiation therapy (SBRT) patient prescribed 48 Gy in 3 fractions, a glioblastoma patient prescribed 60 Gy in 30 fractions, and a

prostate patient prescribed 60 Gy to the prostate gland and 44 Gy to the pelvic lymph nodes in 20 fractions. For each patient, three treatment plans were optimized: (i) a simTr-VMAT treatment plan; (ii) a simTr-VMAT treatment plan with trajectory smoothing, with simulated annealing applied to reshape the repositioned apertures; (iii) a simTr-VMAT treatment plan with trajectory smoothing, but without the simulated annealing step. The treatment plan for the lung patient was prepared for delivery on a TrueBeam STx linear accelerator equipped with the High Definition 120-leaf MLC (HDMLC, interior leaf width: 2.5 mm at isocentre), while the treatment plans for the glioblastoma and prostate patients were prepared for delivery on a TrueBeam linear accelerator equipped with a Millennium MLC (MMLC, interior leaf width: 5.0 mm at isocentre). For the optimization, increased safety margins were added to the defined collision avoidance regions.

7.3.5 Treatment Plan Delivery

For the dosimetric measurements, the treatment plans were delivered to a 30 cm $\times$ 30 cm $\times$ 14 cm water-equivalent phantom (Solid Water, Gammex, Middleton, WI, USA), with Exradin A1SL ionization chamber (Standard Imaging, Madison, WI, USA) measurements recorded at 3.4 cm depth, and Gafchromic EBT3 film (Ashland Specialty Ingredients, Wilmington, DE, USA) measurements recorded at a 2.0 cm depth. Dose calculations matching the treatment plan delivery conditions were performed using EGSnrc Monte Carlo (MC) [20], with beam orientations added intermediary to the defined control points with interpolated MLC leaf positions and MU output. The MC dose calculations were performed under static conditions, with the final angular spacing between control points intended to minimize the degradation of the treatment plan quality with an arc-based delivery. The MU output for the treatment deliveries was scaled such that the film plane dose maximum was within the range of the calibration film doses (maximum: 3.2 Gy). The comparisons of measurement to calculated dose were performed following recommendations of the American Association of Physicists in Medicine (AAPM) Task Group 218 report, which suggests tolerance and action limits for plan specific quality assurance. For ionization chamber measurements, the tolerance and action limits placed on the absolute agreement are $\leq$2% and $\leq$3%, respectively, while for gamma index analysis for radiochromic film measurements, the tolerance and action limits are $\geq$95% and $\geq$90%, respectively. Exceeding the tolerance limit indicates a clinically acceptable result, while measurements that meet only the action limit should prompt further investigation, but do not necessarily indicate a clinically unacceptable treatment plan.

Table 7.1 For the base and smoothed trajectories, the number of direction reversals for the gantry rotation and couch rotation are listed, with the difference showing the net effect of the smoothing algorithm on the trajectory path.

Patient Case	Gantry			Couch		
	Base	Smoothed	Difference	Base	Smoothed	Difference
Lung	8	8	0	7	5	2
Glioblastoma	4	2	2	11	3	8
Prostate	10	0	10	10	4	6

In addition to the simTr-VMAT and smoothed treatment plans, the optimized treatment plans for the glioblastoma patient were delivered as step-and-shoot plans with static MLC, to validate the arc-based delivery conversion of the optimized treatment plan. Trajectory log files were collected for the glioblastoma arc deliveries to evaluate the discrepancies between the expected and actual positions of the gantry, couch, and leaves of the MLC.

7.4 Results

7.4.1 Treatment Plan Optimization

Dose-volume histograms comparing the base simTr-VMAT optimization to the smoothed trajectory optimization for each patient are shown in Fig. 7.3. The discrepancies between the two treatment plans for each patient are marginal and not clinically relevant. Fig. 7.4 shows a comparison of the base and smoothed trajectory paths. The number of removed control points during the smoothing is 3, 3, and 2, for the lung, glioblastoma, and prostate plans, respectively, and the number of repositioned control points during the smoothing is 3, 6, and 7, for the lung, glioblastoma, and prostate plans, respectively. The rotation direction is denoted by the colour of the line segments, with positive/negative couch rotation shown as blue/cyan, and positive/negative gantry rotation as red/orange. The number of directional changes for the smoothed trajectories compared to the base trajectory for each patient case are listed in Table 7.1. Fig. 7.5 illustrates the objective function value as a function of the iteration number for each of the optimizations performed on the patient cases.

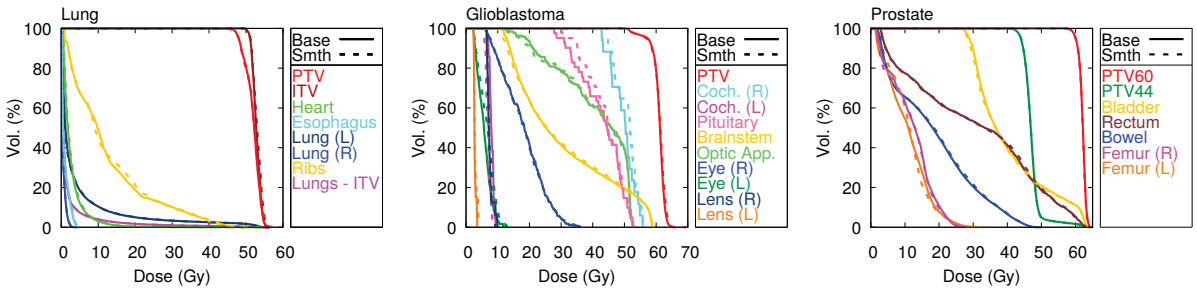

Figure 7.3 Dose-volume histograms for the three patient cases, comparing the dose distributions for the simTr-VMAT optimization to the smoothed trajectory optimizations with simulated annealing. Left: lung; middle: glioblastoma; right: prostate.

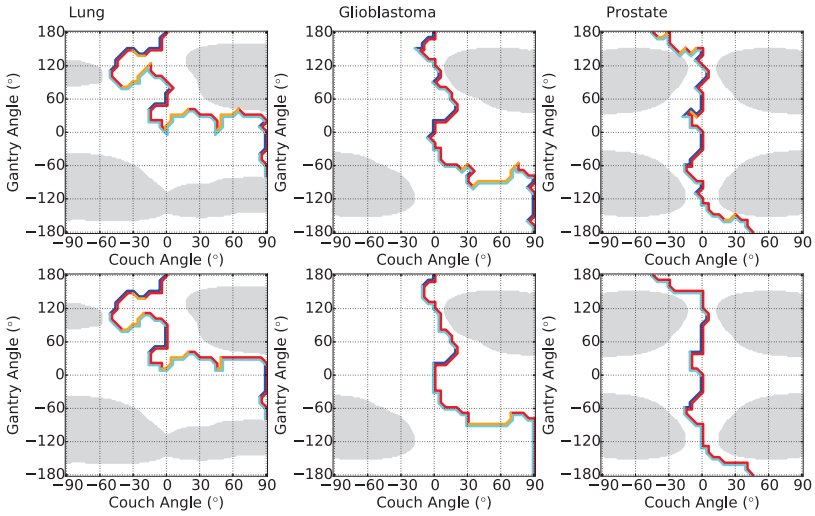

Figure 7.4 Base and smoothed trajectory paths for each patient case. Left: lung; middle: glioblastoma; right: prostate. Monotonically increasing arc rotations for the gantry and couch are denoted by the colour of the line segment, with positive/negative couch rotation shown as blue/cyan, and positive/negative gantry rotation shown as red/orange. Grey regions indicate collision zones.

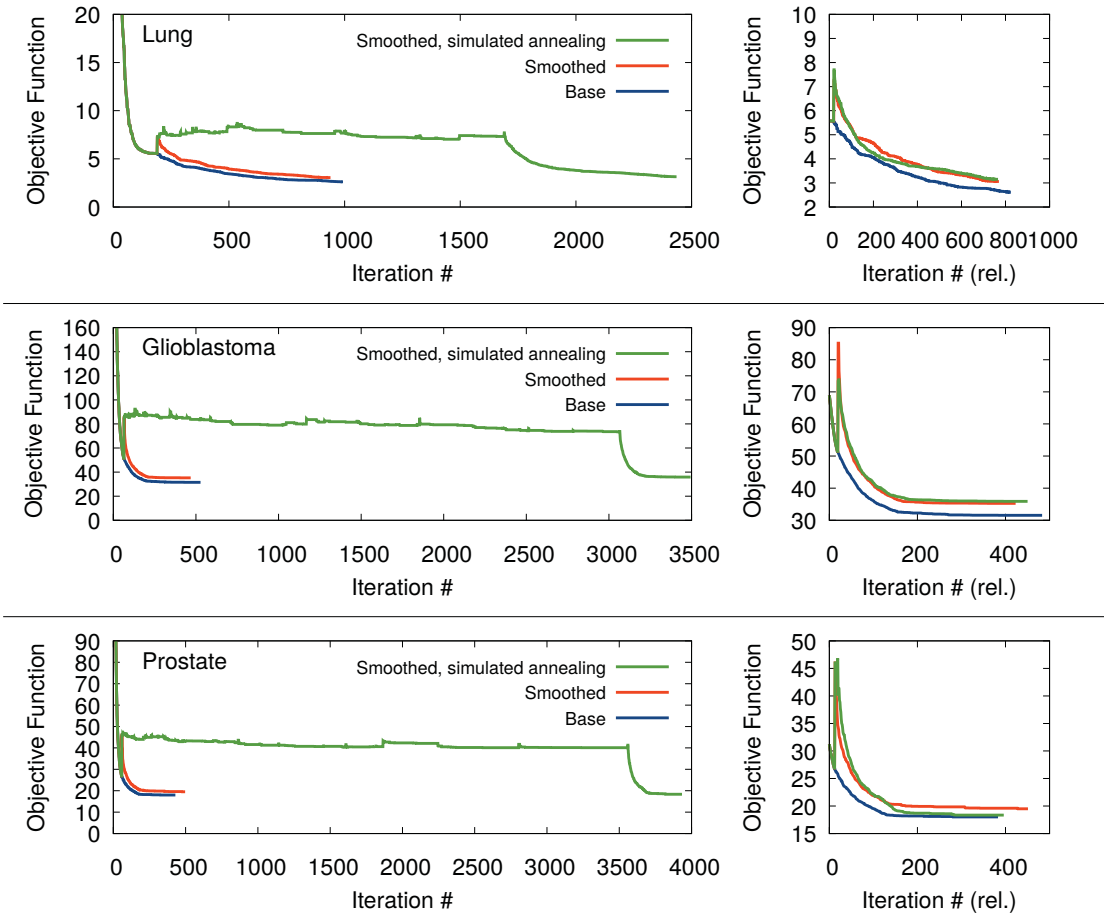

Figure 7.5 Left: as a function of the optimization iteration number, the objective function value was recorded for the simTr-VMAT optimization, the smoothed optimization without simulated annealing, and the smoothed optimization using simulated annealing. Right: the objective function progression for each optimization, excluding the simulated annealing steps, are compared. Top: lung; middle: glioblastoma; bottom: prostate.

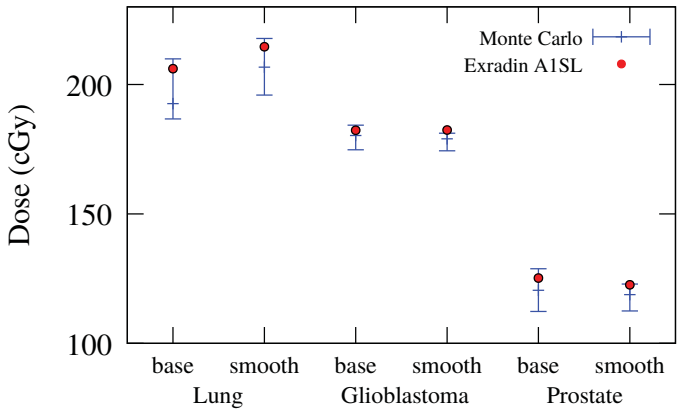

Figure 7.6 MC dose calculations relative to Exradin A1SL ionization chamber measurements for the base and smoothed treatment plans for each patient. The calculated point dose minimum and maximum to the contoured ionization chamber volume as upper and lower bounds on the average chamber dose are shown as horizontal blue lines, with the red points indicating the ionization chamber measurements.

7.4.2 Plan Delivery

The ionization chamber measurements are shown with the MC dose calculation statistics in Fig. 7.6, showing the 20th percentile, median, and 80th percentile dose for the simulation. The number of histories simulated in the MC dose calculations yielded an average dose uncertainty for voxels receiving greater than 50% of the maximum dose of less than 1% of the maximum dose. Table 7.2 provides the numerical values. The MC dose distributions demonstrated a consistent underestimation of measured ionization chamber dose, which was corroborated by comparing the maximum dose of the film measurements. The gamma analysis was applied for criteria of 3% global dose difference, 2 mm distance-to-agreement, with a threshold of 10% of the maximum dose applied, following the recommendations of AAPM Task Group 218 [21]. The film dose was rescaled based on the ionization chamber agreement with the MC measurements, and the gamma analysis was repeated. Fig. 7.7, 7.8, and 7.9 show isodose contours for the film (scaled) and MC dose planes, as well as the corresponding gamma maps, for the base and smoothed treatment plans for each of the patient cases. The percentage of passing pixels for each analysis is shown in Table 7.2.

The gliobastoma base and smoothed treatment plans were delivered under equivalent measurement conditions as both arc deliveries and step-and-shoot deliveries, with the ionization

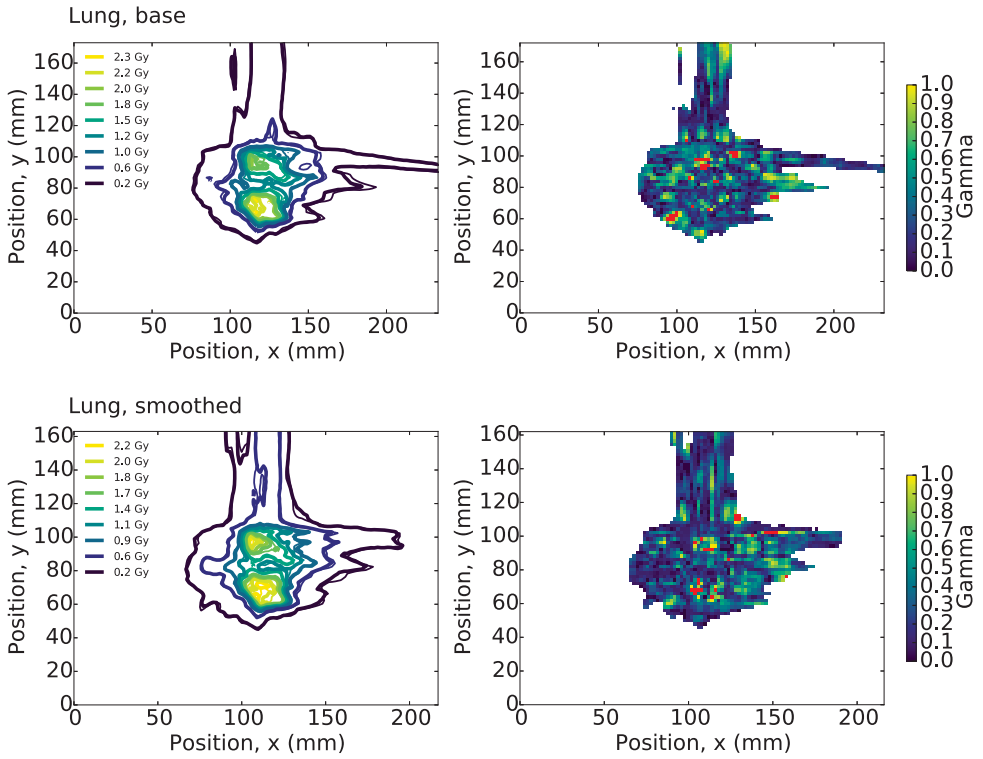

Figure 7.7 Left: Isodose lines comparing the radiochromic film dose (thin lines) and corresponding Monte Carlo dose plane (thick lines) for the lung patient, for the base simTr-VMAT trajectory (top) and smoothed simTr-VMAT trajectory (bottom). Right: the corresponding gamma distributions are shown with a 10% threshold of the maximum dose applied, and criteria of 2 mm distance-to-agreement and 3% global dose difference.

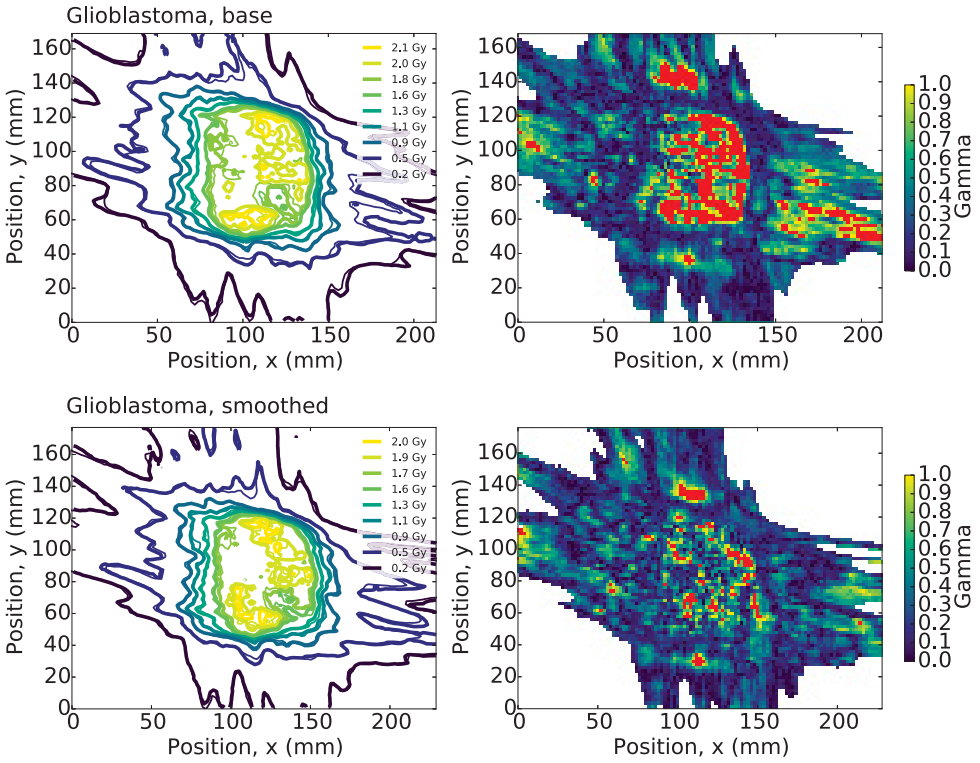

Figure 7.8 Left: Isodose lines comparing the radiochromic film dose (thin lines) and corresponding Monte Carlo dose plane (thick lines) for the glioblastoma patient, for the base simTr-VMAT trajectory (top) and smoothed simTr-VMAT trajectory (bottom). Right: the corresponding gamma distributions are shown with a 10% threshold of the maximum dose applied, and criteria of 2 mm distance-to-agreement and 3% global dose difference.

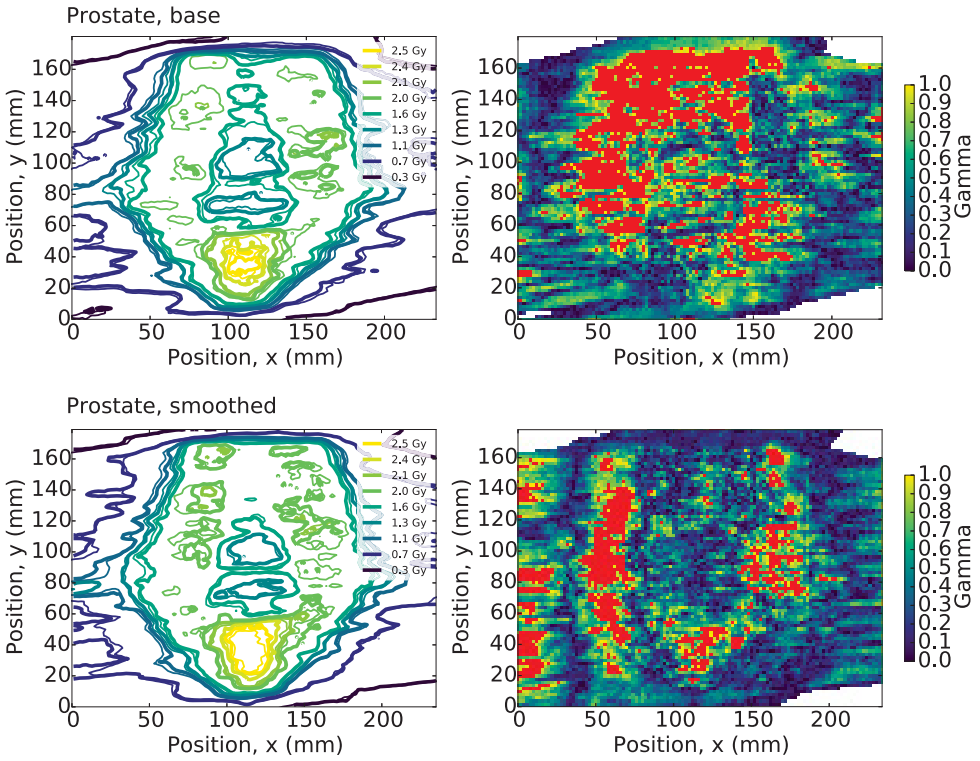

Figure 7.9 Left: Isodose lines comparing the radiochromic film dose (thin lines) and corresponding Monte Carlo dose plane (thick lines) for the prostate patient, for the base simTr-VMAT trajectory (top) and smoothed simTr-VMAT trajectory (bottom). Right: the corresponding gamma distributions are shown with a 10% threshold of the maximum dose applied, and criteria of 2 mm distance-to-agreement and 3% global dose difference.

Table 7.2 Measurement and simulation results for the trajectory-based deliveries. D_{20} and D_{80} denote the 20th and 80th percentiles for the dose measurement to the chamber voxels. The percentage difference for the ionization chamber results is calculated relative to the MC-calculated dose. Gamma analysis was applied to the radiochromic film measurements using a 3%/2 mm criteria, and the percentage of passing pixels is indicated in the table. The relative ionization chamber agreement was used to rescale the film dose measurements, and the percentage of pixels passing the gamma analysis was recalculated.

	Monte Carlo			Ionization Chamber		Film	
	D_{20} (cGy)	D_{med} (cGy)	D_{80} (cGy)	D_{cham} (cGy)	Diff (%)	Γ_{raw}(%)	Γ_{scal} (%)
Lung							
Base	186.7	192.6	209.9	206.1	-7.0	93.1	98.2
Smoothed	195.9	206.7	217.8	214.6	-3.8	97.9	98.5
Glioblastoma							
Base	174.8	180.3	184.3	182.3	-1.1	87.1	91.0
Smoothed	174.4	179.0	181.2	182.4	-1.9	94.3	97.8
Prostate							
Base	112.3	120.5	128.8	125.2	-3.9	95.1	80.5
Smoothed	112.5	118.8	122.9	122.6	-3.2	84.7	89.2

chamber dose recorded for each. The percentage difference of the arc measurement relative to the step-and-shoot measurement was 0.87% and 0.75%, for the base and smoothed plans, respectively.

Throughout the glioblastoma treatment plan deliveries, including setup and repeated measurements, trajectory log files were collected, totalling 9 logs for the base glioblastoma arc delivery, and 5 logs for the smoothed delivery. For each log file, the difference between the expected and actual positions for the gantry rotation angle, couch rotation angle, and each MLC leaf position (for leaves within the jaw-defined field) was calculated at each time point in the log file (sampling frequency: 20 ms). The root mean square error (RMSE) of the positional discrepancies was determined, and the mean RMSE and standard error of the mean was calculated across all deliveries for both the base and smoothed treatment plans. The results are listed in Table 7.3.

7.5 Discussion

In this work, a methodology was developed to simplify a complex trajectory during a simTr-VMAT optimization by removing or repositioning control points comprising the trajectory. The methodology includes a simulated annealing-based procedure that reshapes the apertures for the repositioned control points, in order to adapt the aperture dose distribution to the patient anatomy at the new beam orientation. Although the smoothing and simulated annealing-based procedures

Table 7.3 Trajectory log analysis was performed for 9 deliveries of the base gliobastoma treatment plan, and 5 deliveries of the smoothed glioblastoma treatment plan. The deviation of the actual positions of the gantry rotation, couch rotation, and MLC leaves from the expected positions was used to calculate the root mean square error for each sample (sampling interval: 20 ms). The average RMSE for each treatment plan was calculated, with the uncertainty given as the standard error of the mean.

Glioblastoma	RMSE		
	Gantry Rotation (°)	Couch Rotation (°)	MLC Leaf Position (cm)
Base	0.1259 ± 0.0002	0.03219 ± 0.00005	0.00284 ± 0.00002
Smoothed	0.12563 ± 0.00011	0.02901 ± 0.00005	0.00299 ± 0.00002

are implemented directly into the simTr-VMAT optimization algorithm, these approaches could be adapted to other trajectory-based optimization techniques.

The dose distributions resulting from the smoothed optimizations showed only minor discrepancies compared to the base treatment plans, indicating that the perturbation to the treatment plan caused by the adjustment to the trajectory path did not substantially reduce the benefits of trajectory-based delivery through the simTr-VMAT technique. The progression of the objective function value throughout each optimization shows a numerical benefit to the base optimization that does not yield a clinically-relevant difference in the dose distribution.

The advantage of the simulated annealing approach for the smoothed trajectories was not supported following evaluation of the objective function progression, with comparisons to the smoothed trajectory without simulated annealing. When the column generation procedure resumes, the constructed apertures added to the treatment plan rapidly correct the perturbations to the objective function by the smoothing procedure, with greater effectiveness than the simulated annealing. The final objective function value for the simulated annealing optimizations was not improved in all cases compared to the smoothed optimizations without simulated annealing. Additionally, the simulated annealing applied to the lung treatment plan did not provide a net decrease to the objective function value, although this may be a result of the random nature of the approach and the specific patient case. The simTr-VMAT optimization time, excluding the simulated annealing step, is dependent on the size of the patient anatomy and target volume, and ranged between 1-6 hours. The simulated annealing implementation performed stochastic adjustments to the aperture shapes only, rather than the standard simulated annealing approach for radiation therapy optimization in which the optimization weights would also undergo stochastic

adjustments. Instead, a more consistent but computationally inefficient approach was used, by re-optimizing the weights following each stochastic change to the aperture shapes. The increase to the treatment optimization time by the simulated annealing step was also dependent on the size of the patient anatomy and target volume, as well as the number of repositioned apertures following the trajectory smoothing.

The dosimetric measurements were compared to MC dose calculations following recommendations of the AAPM Task Group 218 report [21]. For the glioblastoma patient, the ionization chamber measurements for both trajectories were within the tolerance limit ($\leq$2%), but for the lung and prostate patients, the ionization chamber measurements for both trajectories were outside of the action limits ($\leq$3%), indicating clinically unacceptable agreement. The glioblastoma step-and-shoot treatment plan deliveries provide a replication of the MC simulation environment without confounding factors such as gantry or couch positioning errors or the arc trajectory conversion influencing the measurement results. The ionization chamber agreement within 1% of the corresponding arc and step-and-shoot deliveries suggests that the arc trajectory conversion is not the cause of the systematically increased ionization chamber measurements relative to the dose calculations. In reviewing the experimental setup and the simulation environment, the following factors may influence the agreement between measured and calculated dose:

- The accurate modelling of radiation transmission through the MLC leaf pairs has not been validated.
- The treatment couch model and material density used for the dose calculations has not been validated through measurement.
- The positioning of the delivery isocentre and the calculation isocentre may not be aligned accurately.
- For the film dose calculations, the slice thickness was 2 mm, with the film dose plane determined as a linear interpolation between two adjacent slices to match the film measurement depth (2.0 cm). The measured film and calculated dose planes may not be accurately aligned.
- For the delivery, backscattered radiation from the collimator jaws may be collected by the linear accelerator monitor chamber, influencing the total radiation output for the delivery. This is a function of the field size relative to reference conditions (10 cm $\times$ 10 cm^2 field), with smaller field sizes resulting in decreased radiation output. The corresponding Monte Carlo dose calculations may not be adequately accounting for this effect.

- In clinical procedures, the material density of the water-equivalent phantom is defined as water for dose calculations, but the actual material density is slightly greater than water (ρ_w = 1.00 g / cm^2; ρ_{sw} = 1.03 - 1.04 g / cm^2). In addition, the density throughout may not be uniform, influencing the results.

These factors are potential sources of disagreement, but do not necessarily resolve the discrepancy. For example, including the material density of the water-equivalent phantom would be expected to decrease the calculated dose, with a greater disagreement to the ionization chamber measurement. A careful review and evaluation of these factors is necessary to determine the cause of the measurement and calculation disagreement.

In spite of the ionization chamber systematic discrepancy, with rescaling of the film dose distributions using the ionization chamber results, the percentage of passing pixels for the smoothed lung and glioblastoma treatment plans are within the tolerance limit suggested by the TG-218 report ($\geq$95%), each with an increased passing rate relative to the base treatment plans (base lung: $\geq$95%; base glioblastoma: $\geq$90%), while both the base and smoothed prostate film measurements violated the action limits. The base prostate plan showed 95.1% agreement prior to rescaling, deteriorating to 80.5% agreement after rescaling. This is in contrast to each of the other treatment plans, which yielded an increased gamma passing rate upon applying the rescaling factor. Given the ionization chamber measurement discrepancy for the base prostate plan, the film gamma passing rate is unlikely to be accurate. Overall, the film dose measurements were in support of the ionization chamber results, as the MC calculations were systematically lower than the dose for most of the comparison plane.

For the prostate patient, the lymph node involvement may be a contributor to the failing gamma pass rates as well as the ionization chamber discrepancy, as substantial leaf motion from one nodal region to the other nodal region with arc delivery would result in decreased dose to the nodes and an increased dose to the center region where the ionization chamber was situated, due to the linear interpolation between adjacent control points. For the lung and glioblastoma patient, however, this rationale would not apply, as they are comprised of a less complex target volume.

The trajectory log analysis yielded RMSE estimates for the gantry rotation angle of approximately 0.13° for both the base and smoothed trajectories, while the RMSE for the couch rotation was 0.032° and 0.029° for the base and smoothed trajectories, respectively, of the glioblastoma patient. These results demonstrate that the more substantial discrepancies in the actual positions compared to the expected positions were due to the gantry rotation rather than the couch rotation, in contrast to the concerns suggested in the literature. Additionally, the gantry rotation RMSE was an order of magnitude greater than those reported by Wilson *et al.*, while the couch rotation

RMSE was less than the reported couch RMSE [11]. While maintaining smooth couch rotation may remain important for patient comfort during treatment delivery, the dose deposition accuracy for trajectory-based optimization may benefit from increased attention to the gantry rotation angle. The agreement of the couch rotation angle for the smoothed delivery was marginally improved relative to the base delivery. The reported RMSE positional accuracy for the MLC leaves was negligible, much less than a millimetre.

7.6 Conclusion

There were three main objectives to the methods applied in this work: (i) to determine the delivery accuracy for complex, trajectory-based treatment plans; (ii) to implement and evaluate a trajectory smoothing procedure using simulated annealing; (iii) to determine the relative improvement in delivery accuracy for smoothed trajectory plans compared to the base plans. For the first objective, the dose delivery accuracy could not be wholly demonstrated through the ionization chamber and film measurements. Although the delivery accuracy were largely within combined standard uncertainty with coverage factor 2, the systematic discrepancy between the measurements and Monte Carlo calculations requires further investigation. For the second objective, the trajectory smoothing successfully reduced the instances of couch or gantry direction reversals for each patient case, while retaining the treatment quality based on the dose-volume histograms. The simulated annealing step to resample the repositioned apertures in the smoothed trajectory did not yield an advantage to the final objective function value. For the third objective, the ionization chamber agreement and film gamma passing rates were improved relative to the base treatment plans for all patients. More work is necessary to investigate the reasons for the observed discrepancies including scrutinization of the MC simulation environment with incorporation of the treatment couch and the experimental details, along with phantom materials and homogeneity and choice of detector.

References

[1] M. Langhans, J. Unkelbach, T. Bortfeld, and D. Craft, “Optimizing highly noncoplanar VMAT trajectories: the NoVo method,” Phys. Med. Biol. **63**, 025023 (2018).

[2] Y. Yang, P. Zhang, L. Happersett, J. Xiong, J. Yang, M. Chan, K. Beal, G. Mageras, and M. Hunt, "Choreographing couch and collimator in volumetric modulated arc therapy," Int. J. Radiat. Oncol., Biol., Phys. **80**, 1238–1247 (2011).

[3] R. L. MacDonald and C. G. Thomas, "Dynamic trajectory-based couch motion for improvement of radiation therapy trajectories in cranial SRT," Med. Phys. **42**, 2317–2325 (2015).

[4] G. Smyth, J. C. Bamber, P. M. Evans, and J. L. Bedford, "Trajectory optimization for dynamic couch rotation during volumetric modulated arc therapy," Phys. Med. Biol. **58**, 8163–8177 (2013).

[5] D. Papp, T. Bortfeld, and J. Unkelbach, "A modular approach to intensity-modulated arc therapy optimization with noncoplanar trajectories," Phys. Med. Biol. **60**, 5179–5198 (2015).

[6] E. Wild, M. Bangert, S. Nill, and U. Oelfke, "Noncoplanar VMAT for nasopharyngeal tumors: Plan quality versus treatment time," Med. Phys. **42**, 2157–2168 (2015).

[7] Q. Lyu, V. Y. Yu, D. Ruan, R. Neph, D. O'Connor, and K. Sheng, "A novel optimization framework for VMAT with dynamic gantry couch rotation," Phys. Med. Biol. **63**, 125013 (2018).

[8] P. Dong, H. Liu, and L. Xing, "Monte Carlo tree search-based non-coplanar trajectory design for station parameter optimized radiation therapy (SPORT)," Phys. Med. Biol. **63**, 135014 (2018).

[9] R. L. MacDonald, C. G. Thomas, and A. Syme, "Dynamic collimator trajectory algorithm for multiple metastases dynamic conformal arc treatment planning," Med. Phys. **45**, 5–17 (2018).

[10] M. K. Fix, D. Frei, W. Volken, D. Terribilini, S. Mueller, O. Elicin, H. Hemmatazad, D. M. Aebersold, and P. Manser, "Part 1: Optimization and evaluation of dynamic trajectory radiotherapy," Med. Phys. **45**, 4201–4212 (2018).

[11] B. Wilson, K. Otto, and E. Gete, "A simple and robust trajectory-based stereotactic radiosurgery treatment," Med. Phys. **44**, 240–248 (2017).

[12] B. Wilson and E. Gete, "Machine-specific quality assurance procedure for stereotactic treatments with dynamic couch rotations," Med. Phys. **44**, 6529–6537 (2017).

[13] J. Mullins, M.-A. Renaud, M. Serban, and J. Seuntjens, "Simultaneous trajectory generation and volumetric modulated arc therapy optimization," Med. Phys. **47**, 3078–3090 (2020).

[14] H. E. Romeijn, R. K. Ahuja, J. F. Dempsey, and A. Kumar, "A column generation approach to radiation therapy treatment planning using aperture modulation," SIAM J. Optim. **15**, 838–862 (2005).

[15] F. Peng, X. Jia, X. Gu, M. A. Epelman, H. E. Romeijn, and S. B. Jiang, "A new column-generation-based algorithm for VMAT treatment plan optimization," Phys. Med. Biol. **57**, 4569–4588 (2012).

[16] M.-A. Renaud, M. Serban, and J. Seuntjens, "On mixed electron-photon radiation therapy optimization using the column generation approach," Med. Phys. **44**, 4287–4298 (2017).

[17] K. Otto, "Volumetric modulated arc therapy: IMRT in a single gantry arc," Med. Phys. **35**, 310–317 (2008).

[18] L. Masi, R. Doro, V. Favuzza, S. Cipressi, and L. Livi, "Impact of plan parameters on the dosimetric accuracy of volumetric modulated arc therapy," Med. Phys. **40**, 071718 (2013).

[19] E. Christiansen, E. Heath, and T. Xu, "Continuous aperture dose calculation and optimization for volumetric modulated arc therapy," Phys. Med. Biol. **63**, 21NT01 (2018).

[20] D. W. O. Rogers, I. Kawrakow, J. P. Seuntjens, B. R. B. Walters, and E. Mainegra-Hing, "NRC user codes for EGSnrc," NRCC Report PIRS-702 (Rev. B) (2003).

[21] M. Miften, A. Olch, D. Mihailidis, J. Moran, T. Pawlicki, A. Molineau, H. Li, K. Wijesooriya, J. Shi, P. Xia, N. Papanikolaou, and D. A. Low, "Tolerance limits and methodologies for IMRT measurement-based verification QA: Recommendations of AAPM Task Group No. 218," Med. Phys. **45**, e53–e83 (2018).

8

Spherical decomposition for trajectory-based delivery

Joel Mullins and Jan Seuntjens

Preface

During the development of the simTr-VMAT optimization approach, the trajectory paths were forced to terminate when a gantry angle of $\pm 180^{\circ}$ was reached, at an arbitrary couch angle. This behaviour was enforced due to the realization that the addition of further control points at a new couch rotation did not yield a distinct, independent beam orientation, and thereby increased the trajectory length and degraded the efficiency of the treatment plan. It was hypothesized that trajectories under a spherical coordinate system, rather than the conventional gantry-couch coordinate system, would yield improved treatment plans due to a more consistent angular spacing between adjacent control points.

8.1 Abstract

Purpose: The conventional approach to trajectory optimization involves the definition of the trajectory path within a gantry-couch coordinate system, but this results in degenerate gantry-couch coordinates that correspond to the same beam orientation - leading to loss in delivery efficiency. The purpose of this work was to compare trajectories implemented on a cartesian gantry-couch coordinate system to trajectories implemented on a spherical coordinate system.
Methods: The angular space was decomposed into regions of approximately equal solid angle, defining the spherical coordinate system using θ, ϕ indices. A trajectory optimization method was implemented using a overlap score map approach with the optimal trajectory determined using Dijkstra's Shortest Path First algorithm. Separate trajectory optimizations were defined for the cartesian coordinate system and the spherical coordinate system. Volumetric modulated arc therapy optimization was performed using the column generation approach, and applied for each coordinate system to 7 patient cases.
Results: The distribution of arclengths calculated between adjacent control points was found to be reduced for the spherical trajectories when arc segments with couch-only rotations were present in the cartesian trajectory, which occurred in 4 out of 7 cases. In comparing the Dijkstra paths, the spherical trajectories had a shorter cumulative overlap score for 4 patients, with negligible differences in the cumulative overlap score for 2 patients. The spherical trajectory optimizations yielded improved objective function values in 4 out of 7 cases, but for two of the instances where the cartesian trajectories outperformed the spherical trajectories, the result was attributed to limitations of the optimization approach when applied to a spherical coordinate system, yielding inferior coplanar treatment plans to the cartesian treatment plans.
Conclusion: The trajectories optimized under a spherical coordinate system were less susceptible to the existence of couch-only rotations between adjacent control points, yielding a more consistent distribution of arclengths independent of patient case. The spherical trajectories did not, however, consistently yield improved objective function values compared to the cartesian trajectories. Limitations of the overlap score map approach for trajectory optimization were demonstrated when implemented with the spherical coordinate system.

8.2 Introduction

Recent developments in linear accelerator technology have enabled the use of dynamic trajectories that involve the coordinated motion of the gantry and treatment couch during radiation delivery.

This capability has led to several publications implementing treatment planning techniques that combine dynamic gantry and couch rotation with volumetric modulated arc therapy (VMAT) optimization [1–10].

Conventionally, the trajectories are defined as a series of control points with an associated gantry angle and couch angle. Through the VMAT optimization, multileaf collimator (MLC) apertures are defined, and the weight corresponding to the radiation output is determined. The gantry and couch angles (g,c) can be visualized as coordinates on a cartesian grid, with limits defined by the allowable linear accelerator positions ($-180 \leq g \leq 180$, $-90 \leq c \leq 90$). Trajectories are thus represented as paths traversing discrete points on the cartesian coordinate system.

This approach using a gantry-couch coordinate system is potentially inefficient, as it does not uniformly sample the angular space. The arclength between coordinates separated by a couch rotation is dependent on the gantry angle. This can be illustrated in Fig. 8.1. For a coplanar trajectory spanning 360° of gantry rotation, the arclength separation between adjacent control points is uniform. With the addition of couch rotation, as seen in the baseball stitch trajectory, the angular spacing is no longer uniform. For trajectories that include arc segments with only couch rotation, such as in the simTr-VMAT treatment plan, the arclength can vary substantially throughout the trajectory. In particular, it can be observed that for a gantry angle of 0° or ±180°, any rotation of the couch does not yield a distinct beam orientation, and that the arclength spacing is maximized for gantry angles equalling ±90°.

We hypothesize that the implementation of a trajectory optimization algorithm under a spherical coordinate system may result in improved or more efficient treatment plans. In this work, a trajectory optimization algorithm was implemented under both a cartesian and spherical coordinate system, and applied to seven patient cases. The resulting treatment plans were evaluated on the basis of their optimization objective function and trajectory path.

8.3 Materials and Methods

8.3.1 Spherical Decomposition

A spherical coordinate system was defined based on the approaches outlined by Beckers *et al.* [11]. The spherical decomposition is visualized in Fig. 8.2. The polar angle θ is discretized into 10° increments, with the integer number of ϕ divisions chosen to approximate the same solid angle for each region. Under this coordinate system, for a gantry rotation angle of 0° or ±180°, any couch angle is projected onto the same solid angle region at the poles of the sphere.

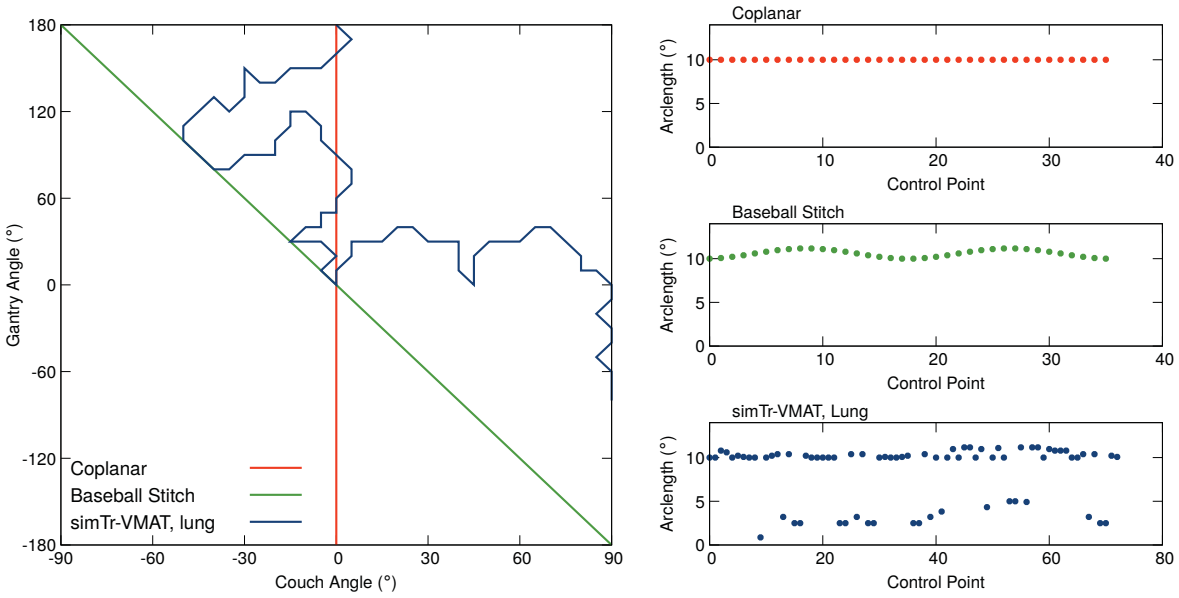

Figure 8.1 Left: gantry-couch coordinate system depicting trajectory paths for three example trajectories. For each trajectory, the arclength difference between adjacent control points was calculated and shown in the figures on the right.

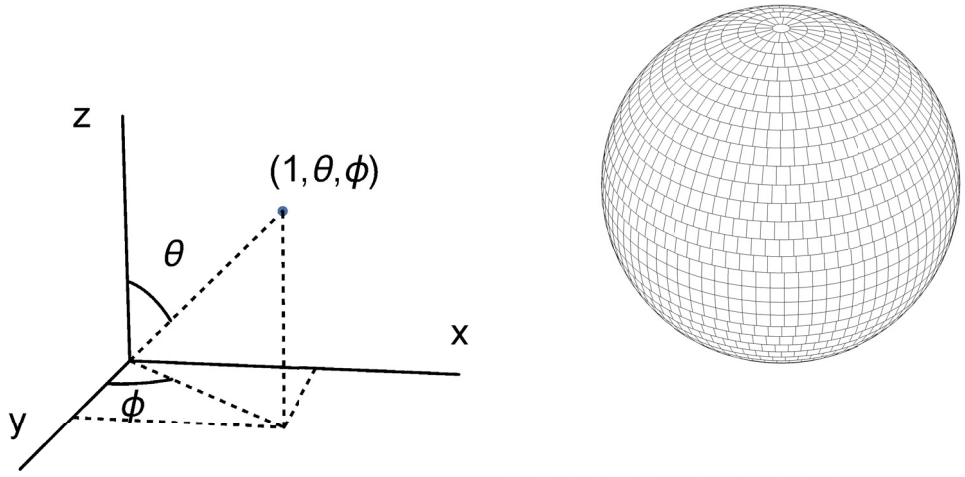

Figure 8.2 Decomposition of the 4π angular space into regions of approximately equal solid angle. The polar angle θ divisions are separated by 10°, while the integer number of azimuthal regions was selected to maintain a consistent solid angle for each region.

8.3.2 Trajectory Optimization

Overlap Score Map

The method adopted in this work to define a gantry-couch trajectory was based on the work of Yang *et al.* and Smyth *et al.*, using a cost map based on the beam's eye view overlap between the planning target volume (PTV) and surrounding organs-at-risk (OARs), and using Dijkstra's Shortest Path First algorithm to determine the shortest path through the cost map [2, 4, 12].

To calculate the overlap score for a given beam orientation, voxels corresponding to the PTV and OARs were projected onto a pixelized plane orthogonal to the beam orientation. A bounding box for the PTV was defined, analogous to the radiation field during treatment delivery, and the score was calculated as:

$$S(g,c) = \sum_s \frac{O_{s,t}(g,c)}{A_t(g,c)} + \frac{O_{s,t}(g,c)}{A_s(g,c)} \tag{8.1}$$

where $O_{s,t}$ corresponds to the number of overlapping pixels for the sth OAR and the PTV, A_t is the total number of pixels for the PTV, and A_s is the total number of pixels for the sth OAR. This score is minimized when the PTV is unoccluded ($O_{s,t} = 0$), and increases as the fractional overlap of the PTV by the OARs increases, or the fractional overlap of the OARs by the PTV increases.

The overlap scores were comprehensively determined for each gantry-couch coordinate (for the cartesian coordinate system) and at each θ-ϕ coordinate (for the spherical coordinate system), and normalized to a maximum of 1.0. For beam orientations that resulted in an overlap score of 0, a minimum score of 0.00001 was set. Fig. 8.3 shows an example of the score map in each coordinate system for a patient case. The yellow regions correspond to forbidden zones due to the potential for collision between the gantry and couch. The dark blue regions surrounding the spherical coordinate system are used solely for visualization. As the spherical coordinate system is a projection of a three-dimensional sphere into two dimensions, the edges of the figure are implicitly adjacent to each other. The top pole of the spherical coordinate system corresponds to a gantry angle of 0°, while the bottom pole corresponds to a gantry angle of $\pm$180°. A gantry rotation through -180° to 0° traverses the left hemisphere, while a gantry rotation through 0° to 180° traverses the right hemisphere.

Dijkstra's Algorithm

Dijkstra's Shortest Path First algorithm is a pathfinding algorithm that can efficiently determine the shortest path between two nodes in a directed graph with non-negative weights. For this

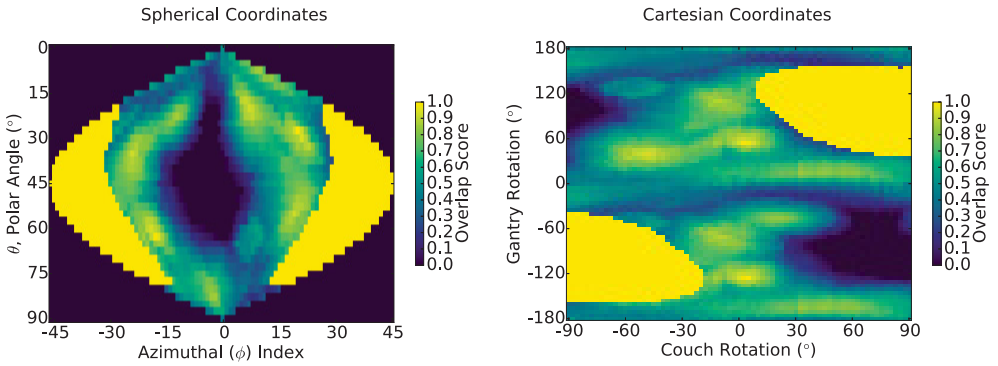

Figure 8.3 Overlap score maps for an example patient depicted in a spherical coordinate system (left) and a cartesian coordinate system (right). Solid yellow regions denote forbidden collision zones.

application, the graph nodes and weights correspond to beam orientations and the overlap scores, respectively.

For the cartesian coordinate system, edges connecting the nodes were defined for any adjacent node with a non-negative gantry rotation. For each couch angle in the discretized graph, the shortest path was determined for an initial coordinate at a gantry angle of -180°. The resulting trajectory spanned a 360° gantry arc, ending at a gantry angle of 180°. Each of the Dijkstra paths originating at a distinct couch angle were compared, and the shortest overall path was used to define the optimization trajectory.

For the spherical coordinate system, a pre-processing step was performed to determine edges connecting between different nodes, based on the arclength separating the corresponding beam orientations. At the same polar angle, edges were added to adjacent nodes if the arclength was less than a specified threshold, with a maximum of two edges added. For the subsequent polar angle (corresponding to a positive gantry rotation), any number of nodes were connected if the arclength was less than the specified threshold. The threshold was calculated based on the maximum arclength for one unit of gantry rotation (5°) and one unit of couch rotation (2.5°) from the cartesian coordinate system, equalling 5.59°. To ensure a full 360° gantry arc rotation, the pre-processing step was applied for nodes in the left and right hemispheres of the spherical coordinate system separately. Dijkstra's algorithm was similarly applied in two steps, determining the shortest path connecting the poles in the left hemisphere, followed by the shortest path connecting the poles in the right hemisphere.

For dose calculations, VMAT optimization, and treatment delivery on a linear accelerator, the trajectory path must be transformed from θ-ϕ coordinates into gantry-couch coordinates. As indicated previously, for a given ϕ angle, there may exist multiple degenerate couch rotation angles that correspond to the same solid angle region. During the transformation to gantry-couch coordinates, the couch angle was selected to minimize the jagged trajectory paths while remaining in the same solid angle region of the spherical decomposition, when possible.

8.3.3 Treatment Plan Optimization

For this study, trajectory paths under both coordinate systems were generated for 7 patient cases with cranial targets. For each coordinate in the trajectory path, a rectangular grid of non-diverging 2.5 mm $\times$ 2.5 mm beamlets was arranged, with beamlet doses calculated using a collapsed-cone convolution-superposition algorithm. Treatment plans were generated using the column generation approach applied to VMAT optimization [13–15]. The treatment planning constraints had been previously defined for the patient cohort in a previous study, and were applied without adjustment to both the cartesian and spherical trajectory optimizations.

8.4 Results

The trajectory paths generated through the overlap score maps are shown in Fig. 8.4 under both coordinate systems for two example patient cases (#1, #3). For each trajectory, the arclength between adjacent control points was calculated, illustrated in Fig. 8.5. The top row corresponds to trajectories under the cartesian coordinate sysem, while the bottom corresponds to trajectories under the spherical coordinate system. For the cartesian trajectories, the arclengths for individual points can be interpreted as belonging to a distinct category: (i) gantry rotation only, with an arclength of 5°; (ii) couch rotation only, with an arclength less than or equal to 2.5°; (iii) gantry and couch rotation, with an arclength greater or equal to 5°. For the spherical coordinate system, couch-only rotations can be identified, but with a minimum arclength of approximately 3.5°. Table 8.1 presents statistics that describe the arclength distribution for each trajectory.

For each trajectory, the average overlap score was calculated by dividing the Dijkstra path length by the number of nodes, shown in Fig. 8.6a. For patient #2, the only relevant OARs in proximity to the PTV were easily avoided by both the cartesian and spherical trajectory, resulting in a minimum path score. The objective function value following the VMAT optimizations was

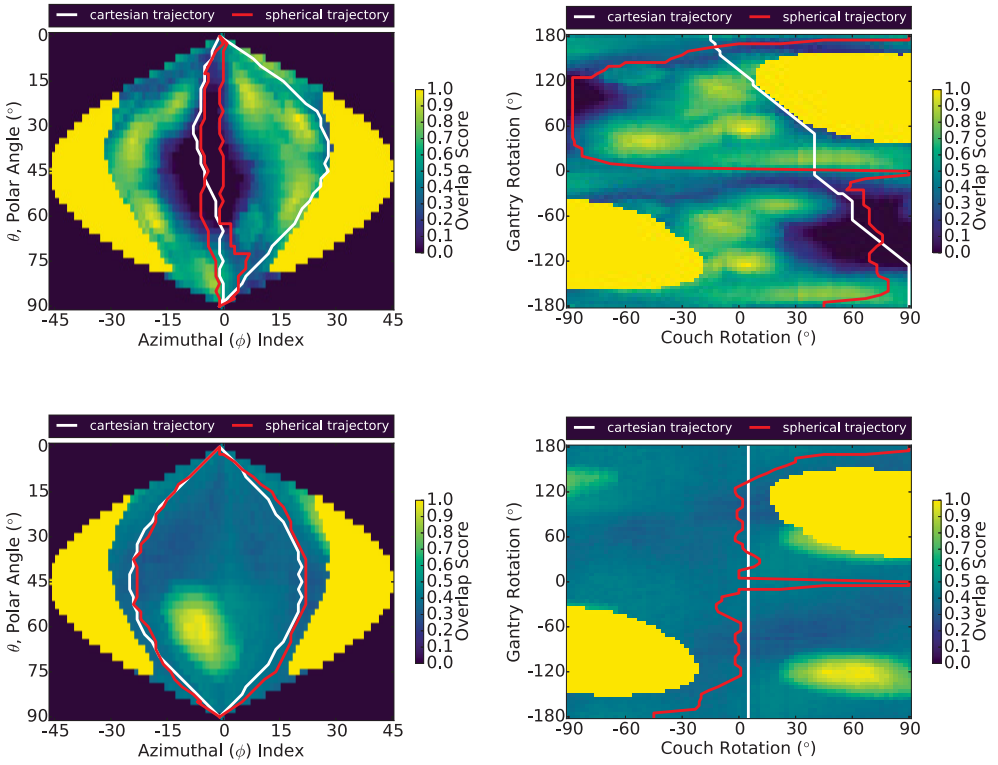

Figure 8.4 Dijkstra shortest path trajectories were calculated under conditions of a spherical coordinate system (red) and a cartesian coordinate system (white). For comparison, both trajectories are illustrated on the overlap score map for each coordinate system (left: spherical; right: cartesian). Top: patient #1; bottom: patient #3.

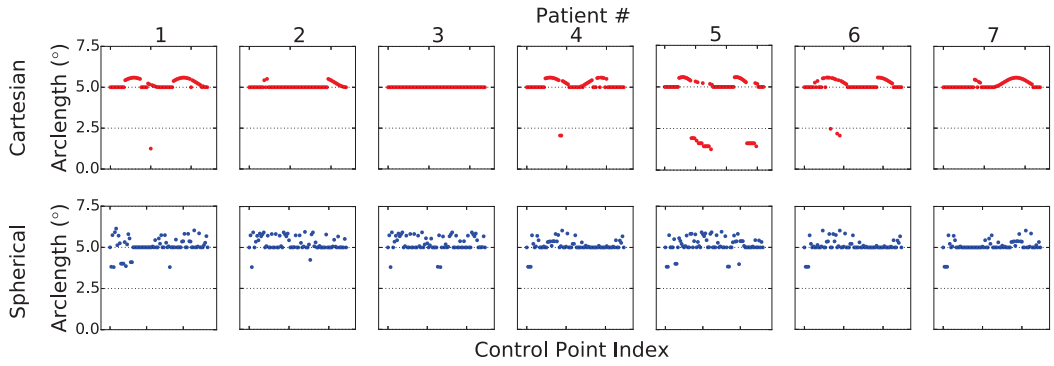

Figure 8.5 For each trajectory, the arclength between successive control points was calculated. The patient cases are arranged from left to right, with points indicating the arclength for the cartesian trajectories (top) and the spherical trajectories (bottom) as a function of the control point index.

Table 8.1 For the data illustrated in Fig. 8.5, the average arclength and standard deviation was calculated for each trajectory. The coefficient of variation (COV) is calculated to describe the relative distribution of the data.

	Cartesian			Spherical		
Patient Case	Mean Arclength (°)	Standard Deviation (°)	COV (%)	Mean Arclength (°)	Standard Deviation (°)	COV (%)
1	5.2	0.5	10.1	5.1	0.5	9.8
2	5.06	0.14	2.7	5.3	0.4	7.8
3	5.0	0.0	0.0	5.3	0.5	8.7
4	5.1	0.6	10.9	5.1	0.4	7.2
5	4.3	1.6	37.2	5.2	0.5	9.7
6	5.1	0.6	12.3	5.1	0.4	7.4
7	5.2	0.2	4.2	5.1	0.4	7.0

also recorded and normalized to the spherical treatment plan objective function value for each patient (Fig. 8.6b).

8.5 Discussion

The purpose of this study was to investigate the consequences of trajectory-based treatment plan optimization under a gantry-couch coordinate system, which inherently does not uniformly sample the angular space, through comparisons to treatment plan optimizations under a spherical coordinate system. The trajectory optimization algorithm implemented was based on existing literature using a two-step approach, where the trajectory path is determined in the first step based on an overlap score map using Dijkstra's algorithm, followed by a VMAT optimization performed on the trajectory in the second step.

The spherical coordinate system approach was effective in minimizing the variation in arclength spacing for a trajectory when compared against cartesian trajectories that included only couch rotations between adjacent control points (4 out of 7 patients). The arclength for a couch rotation under the cartesian coordinate system is at most 2.5°, while the spherical equivalent, azimuthal rotations, had an arclength of at least 3.5°. For the remaining three patients, the spherical trajectories were unnecessary to ensure more uniform angular sampling. However, the arclength distributions for the spherical trajectories were more consistently dispersed compared to the cartesian trajectories, which could correspond to more consistent treatment planning results that are independent of the patient. The requirement of a 360° rotation of the gantry defining the trajectory, combined with the shortest path algorithm, discouraged extending the trajectory path

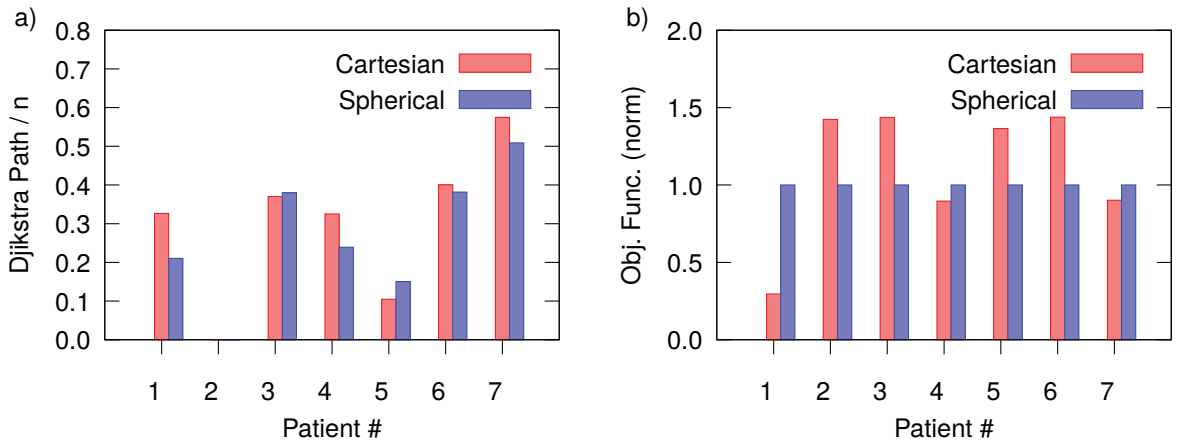

Figure 8.6 Left: the average overlap score was calculated as the Dijkstra path divided by the number of nodes, for each trajectory. For patient #2, the beam orientations forming the trajectories under each coordinate system avoided any overlap between the target and OARs. Right: the objective function value following the VMAT optimizations was recorded. For each patient, the objective function values were normalized to the objective function value for the spherical treatment plan optimization.

through couch rotations; the overlap score penalty of adding a node at an increased gantry angle was rarely large enough to divert the trajectory through a couch-only rotation.

The objective function was improved for the spherical trajectories in 4 out of 7 patient cases, but definitive reasons are difficult to assert. Due to the degeneracy of the couch angle for a gantry angle of 0°, the trajectory paths determined under the spherical coordinate system were afforded increased freedom to explore the entire angular space compared to the cartesian trajectories, as demonstrated by the improved or comparable Dijkstra path score in 6 out 7 patients for the spherical trajectory. Additionally, although multiple control points defined at a degenerate couch angle may lead to an inefficient treatment delivery, the plan quality is unlikely to suffer from the optimization having an increased number of decision variables.

The freedom of the spherical trajectories to explore the angular space highlighted shortcomings with the overlap score map approach for trajectory-based optimization. As illustrated in the top left image of Fig. 8.4, the spherical trajectory for patient #1 traversed similar beam orientations for each half of the trajectory, despite each being restricted to a single hemisphere. In practice, this results in two coplanar 180° gantry arcs that deliver radiation to the patient along the same beam orientations, resulting in dose buildup to healthy tissue, and preventing conditions of dose homogeneity and conformity from being achieved. Trajectories of a similar nature were

also observed for patients #4, #6, and #7, which includes the other two instances in which the cartesian trajectory outperformed the spherical trajectory (#4, #7). Ultimately, these trajectories were favoured by the shortest path algorithm because each beam orientation was considered independently, without consideration for the clinical objectives beyond irradiation of the target volume and sparing critical structures.

The impact that trajectories obtained through a spherical coordinate system would have on a treatment delivery, specifically the delivery time, radiation delivery accuracy, and patient comfort, has not been investigated. The increased angular freedom of the spherical approach frequently resulted in substantial couch rotations at a gantry angle of 0° due to the degeneracy of this beam orientation, which would result in increased treatment time. Additionally, the beam orientations resulting from the spherical decomposition were unable to yield smooth, monotonic couch rotations over the trajectory path, potentially impacting the delivery accuracy. For this optimization approach, a post-processing step could be used to generate a smooth trajectory while retaining the treatment plan quality of the original trajectory path.

Overall, a more comprehensive evaluation of the treatment plan quality with dosimetric results, delivery efficiency, and with consideration to specific patient anatomy, may be necessary to substantiate the advantage of trajectory delivery with spherical coordinates.

8.6 Conclusion

A score map-based trajectory optimization approach using Dijkstra's shortest path algorithm was implemented under a cartesian gantry-couch coordinate system, and a spherical coordinate system. The distribution of calculated arclengths between adjacent control points in the spherical trajectories was less susceptible to couch rotations at a static gantry angle. The spherical trajectories resulted in improved objective function values for 4 out of 7 patient cases, with the improved objective function value for the cartesian trajectory in two of the remaining three cases attributed to limitations of the trajectory optimization method when combined with the spherical coordinate system.

References

[1] M. Langhans, J. Unkelbach, T. Bortfeld, and D. Craft, "Optimizing highly noncoplanar VMAT trajectories: the NoVo method," Phys. Med. Biol. **63**, 025023 (2018).

[2] Y. Yang, P. Zhang, L. Happersett, J. Xiong, J. Yang, M. Chan, K. Beal, G. Mageras, and M. Hunt, "Choreographing couch and collimator in volumetric modulated arc therapy," Int. J. Radiat. Oncol., Biol., Phys. **80**, 1238–1247 (2011).

[3] R. L. MacDonald and C. G. Thomas, "Dynamic trajectory-based couch motion for improvement of radiation therapy trajectories in cranial SRT," Med. Phys. **42**, 2317–2325 (2015).

[4] G. Smyth, J. C. Bamber, P. M. Evans, and J. L. Bedford, "Trajectory optimization for dynamic couch rotation during volumetric modulated arc therapy," Phys. Med. Biol. **58**, 8163–8177 (2013).

[5] D. Papp, T. Bortfeld, and J. Unkelbach, "A modular approach to intensity-modulated arc therapy optimization with noncoplanar trajectories," Phys. Med. Biol. **60**, 5179–5198 (2015).

[6] E. Wild, M. Bangert, S. Nill, and U. Oelfke, "Noncoplanar VMAT for nasopharyngeal tumors: Plan quality versus treatment time," Med. Phys. **42**, 2157–2168 (2015).

[7] Q. Lyu, V. Y. Yu, D. Ruan, R. Neph, D. O'Connor, and K. Sheng, "A novel optimization framework for VMAT with dynamic gantry couch rotation," Phys. Med. Biol. **63**, 125013 (2018).

[8] P. Dong, H. Liu, and L. Xing, "Monte Carlo tree search-based non-coplanar trajectory design for station parameter optimized radiation therapy (SPORT)," Phys. Med. Biol. **63**, 135014 (2018).

[9] M. K. Fix, D. Frei, W. Volken, D. Terribilini, S. Mueller, O. Elicin, H. Hemmatazad, D. M. Aebersold, and P. Manser, "Part 1: Optimization and evaluation of dynamic trajectory radiotherapy," Med. Phys. **45**, 4201–4212 (2018).

[10] B. Wilson, K. Otto, and E. Gete, "A simple and robust trajectory-based stereotactic radiosurgery treatment," Med. Phys. **44**, 240–248 (2017).

[11] B. Beckers and P. Beckers, "A general rule for disk and hemisphere partition into equal-area cells," Computational Geometry **45**, 275–283 (2012).

[12] E. W. Dijkstra, "A note on two problems in connexion to graphs," Numerische Mathematik **1**, 269–271 (1959).

[13] H. E. Romeijn, R. K. Ahuja, J. F. Dempsey, and A. Kumar, "A column generation approach to radiation therapy treatment planning using aperture modulation," SIAM J. Optim. **15**, 838–862 (2005).

[14] F. Peng, X. Jia, X. Gu, M. A. Epelman, H. E. Romeijn, and S. B. Jiang, "A new column-generation-based algorithm for VMAT treatment plan optimization," Phys. Med. Biol. **57**, 4569–4588 (2012).

[15] M.-A. Renaud, M. Serban, and J. Seuntjens, "On mixed electron-photon radiation therapy optimization using the column generation approach," Med. Phys. **44**, 4287–4298 (2017).

9

Summary and Outlook

9.1 Summary

The focus of this thesis was to determine the potential for trajectory-based delivery as a clinically viable treatment delivery technique. The presented research investigated aspects of trajectory-based delivery including: the application of unexplored trajectory approaches, the implementation of a novel optimization methodology, the delivery accuracy for complex trajectory-based treatment plans, and the consequences of a gantry-couch coordinate system for defining trajectory paths. The following sections provide a summary of each of the studies presented in this paper, and highlight the main results and conclusions.

9.1.1 Trajectory-based VMAT for cranial targets with delivery at shortened SAD

The initial work performed in this thesis was presented in Chapter 5, on the application of translational couch motion to a patient-generalized noncoplanar trajectory, reducing the effective treatment distance. The patient cases considered featured cranial targets, due to the additional

collision-free angular space. The use of translational couch motion to shorten the effective treatment distance had not been previously explored, and the advantages were hypothesized to be a reduced projected MLC leaf width at the isocentre and an increased effective dose rate. The optimization of the treatment plans followed three steps: i) beamlet dose calculations using a collapsed cone-convolution superposition algorithm, ii) treatment plan optimization using the column generation approach for VMAT, iii) final dose calculations in Eclipse using the analytical anisotropic algorithm. Tr-VMAT plans were generated at a shortened SAD (80 cm) and standard SAD (100 cm), and were compared to the clinical treatment plans.

The main outcome of this study was the result that the increased effective dose rate yielded shorter treatment delivery times dependent on the fractionation size, which has implications for patient throughput, and limiting intrafraction motion during delivery. This was determined by estimating the treatment time using the treatment plan control point specifications and the nominal values for linear accelerator motion and dose rate, with the agreement to timed delivery of standard tr-VMAT plans establishing the validity of this approach. The investigation into the benefits of reduced projected MLC leaf widths was inconclusive, as the shortened SAD and standard SAD treatment plans were indistinguishable in plan quality; this result was attributed to the use of a beamlet-based grid with discrete rather than continuous positions. Finally, comparison of ionization chamber dose measurements and dose calculations for collapsed delivery of shortened SAD and standard SAD tr-VMAT treatment plans validated the use of AAA dose calculations at shortened SADs.

9.1.2 Simultaneous trajectory and volumetric modulated arc therapy optimization

The second study presented featured a novel trajectory optimization implementation that addressed limitations in previously published approaches to trajectory-based treatment planning, namely the two-step approach defining trajectory paths independently of VMAT optimization, and the avoidance of complex trajectory paths in favour of monotonically increasing couch rotations throughout the trajectory. The hypothesis providing the motivation for this research was that a simultaneous trajectory and VMAT optimization strategy would demonstrate improved treatment plan quality by allowing adaption of the trajectory path through consideration of the treatment planning objectives during the optimization. The trajectory optimization implementation was based on the column generation approach, with the ability of the pricing problem to construct and select an optimal aperture leveraged to additionally determine the trajectory path. The simTr-

VMAT optimization approach was applied to three patient cases (lung, glioblastoma, and prostate), and evaluated against coplanar VMAT plans optimized with the clinical treatment planning system, as well as randomly generated trajectories that represented the solution space for the trajectory optimization problem.

The simTr-VMAT results demonstrated improved treatment plan quality compared to the coplanar VMAT for the lung and glioblastoma patients, with non-inferior plan quality for the prostate patient. The simTr-VMAT approach was further validated through the comparisons to randomly generated trajectories, in which the simTr-VMAT optimizations ranked above the 96th percentile for each of the patient cases, as well as the correspondence to other highly ranking trajectory paths. The random trajectory validation was also demonstrated as an effective method to assess trajectory-based treatment plan optimization algorithms without relying exclusively on treatment planning comparisons. These results taken together establish the potential for the simTr-VMAT optimization methodology as a clinically-relevant treatment technique.

9.1.3 Delivery verification of trajectory-based treatment plans

In Chapter 7, the purpose was to perform delivery verification of trajectory-based plans in order to validate the simTr-VMAT optimization approach and the resulting complex trajectory paths, as well as to address the scarcity of dosimetric measurements for trajectory delivery in the literature. The objectives were to evaluate the delivery accuracy for simTr-VMAT treatment plans using plan-specific quality assurance procedures, and to implement and evaluate a trajectory smoothing algorithm. The trajectory smoothing procedure identified beam orientations that violated a smoothness criteria, and either removed them from the treatment plan, or repositioned them at a different beam orientation. For the repositioned apertures, a simulated annealing approach was used to reshape the apertures. This resulted in a base trajectory plan and a smoothed trajectory plan for each of the three patient cases (lung, glioblastoma, prostate), which were delivered on the TrueBeam linear accelerator, yielding ionization chamber and radiochromic film measurements. Monte Carlo dose calculations matching the treatment delivery conditions were also recorded.

Through this work, the trajectory smoothing procedure was able to maintain the treatment plan quality while reducing the instances of beam orientations that violated the smoothness criteria. The simulated annealing approach was determined to be unnecessary, as the resumption of the column generation approach was more effective in minimizing the impact of the perturbation to the objective function caused by the smoothing. In general, the delivery accuracy, while largely within combined standard uncertainty with coverage factor 2, showed a systematic difference

between ionization chamber measurements and Monte Carlo dose calculations that requires further analysis. However, the smoothed trajectory deliveries yielded improved agreement relative to the base trajectory treatment plans for both ionization chamber measurements and film gamma passing rates, and the trajectory log analysis indicated accurate positioning of the gantry angle, couch angle, and MLC leaves throughout the treatment delivery. These results did not wholly determine the accuracy of trajectory-based delivery, but demonstrates that consideration for the trajectory smoothness would be advantageous for accurate radiation delivery.

9.1.4 Spherical decomposition for trajectory-based delivery

The final study in this thesis challenges the conventional approach in the literature for trajectory-based optimization of a coordinate system defined by the gantry and couch rotation angles. During implementation of the simTr-VMAT optimization methodology, it was observed that control points added to a trajectory at a gantry angle of $\pm 180^{\circ}$ and an arbitrary couch angle were equivalent to rotations of the collimator with no change in beam orientation. Based on this observation, the objective of this study was to evaluate treatment plan quality for trajectory-based optimization under a gantry-couch (cartesian) coordinate system and a spherical coordinate system. A score map-based trajectory optimization was implemented, and applied for 7 patient cases on a gantry-couch coordinate system, as well as a spherical coordinate system defined by decomposing the angular space into regions of approximately equal solid angle.

The treatment plans under each coordinate system were compared based on the arclength calculated between successive control points of the trajectory, and the resultant objective function value of the optimization. The spherical trajectories yielded a more consistent angular spacing when arc segments with only couch rotation were included in the cartesian trajectory, but were otherwise unnecessary. The assessment of the objective function values yielded inconclusive results; although the Dijkstra path score for the spherical trajectories was non-inferior to the cartesian trajectories, the objective function values were improved in 4 out of 7 patient cases. Due to the implementation of the spherical trajectory optimization, the trajectory path was afforded greater access to the angular space, and for four patient cases, traversed similar regions for each half of the trajectory, resulting in a quasi-coplanar delivery with an expected negative impact on the treatment plan quality. This result demonstrates the shortcomings of a two-step approach to trajectory-based optimization. More work is necessary to assess the impact of the spherical coordinate-based trajectories on actual treatment plan quality on a broad set of patient cases.

9.2 Future Directions

As previously stated, the work presented in this thesis was performed to support the clinical implementation of trajectory-based treatment plans. The supporting evidence in the current literature is hindered by a lack of consistent trajectory-based optimization implementation, a limited number of patients included in the study, and diverse treatment sites, and as a result it is difficult to ascertain definite benefits of trajectory-based delivery. Thus, future work towards the clinical implementation of trajectory-based delivery could include a more comprehensive treatment planning comparison with an increased number of patient cases, and preferably targeted to a specific treatment site. The simTr-VMAT methodology was shown to be an effective trajectory optimization technique for the cases considered, and would be a suitable candidate for future validation on a larger patient cohort.

Secondly, as the results of Chapter 7 did not satisfactorily verify the treatment delivery accuracy for the trajectory-based plans, further work is necessary to validate the delivery with comparisons of measurements and dose calculations. If the delivery accuracy cannot be shown with the simTr-VMAT approach, more aggressive smoothing implementations or adjustments to the optimization algorithm may be required, and their impact on the treatment plan quality assessed.

Finally, the individual studies presented in this thesis are not exclusive and can be combined into a single trajectory optimization framework. The simTr-VMAT optimization approach can be redefined for implementation on a spherical coordinate system, and translational couch motion can be included to reduce the effective treatment distance. The implementation of the smoothing procedure into the simTr-VMAT framework has already been demonstrated in Chapter 7. Ideally, this holistic approach to trajectory-based treatment delivery would yield definite advantages compared to conventional clinical treatment plans, and help to expedite the clinical implementation of trajectory-based delivery.

References

[1] J. Tobias and D. Hochhauser, *Cancer and its Management*. Wiley Blackwell, 7 ed., (2015).

[2] D. R. Brenner, H. K. Weir, A. A. Demers, L. F. Ellison, C. Louzado, A. Shaw, D. Turner, R. R. Woods, and L. M. Smith, "Projected estimates of cancer in Canada in 2020," Canadian Medical Association Journal **192**, E199–205 (2020).

[3] R. C. Bast, Jr., C. M. Croce, W. N. Hait, W. K. Hong, D. W. Kufe, M. Piccart-Gebhart, R. E. Pollock, R. R. Weichselbaum, H. Wang, and J. F. Holland, *Holland-Frei Cancer Medicine*. Wiley Blackwell, 9 ed., (2017).

[4] R. Atun, D. A. Jaffray, M. B. Barton, F. Bray, M. Baumann, B. Vikram, T. P. Hanna, F. M. Knaul, Y. Lievens, T. Y. M. Lui, M. Milosevic, B. O'Sullivan, D. L. Rodin, E. Rosenblatt, J. Van Dyk, M. L. Yap, E. Zubizarreta, and M. Gospodarowicz, "Expanding global access to radiotherapy," The Lancet Oncology Commission **16**, 1153–1186 (2015).

[5] E. B. Podgorsak, *Radiation Oncology Physics: A Handbook for Teachers and Students*. International Atomic Energy Agency, (2005).

[6] M. Guckenberger, N. Andratschke, H. Alheit, R. Holy, C. Moustakis, U. Nestle, and O. Sauer, "Definition of stereotactic body radiotherapy," Strahlentherapie und Onkologie **190**, 26–33 (2014).

[7] ICRU, "ICRU Report 91: Prescribing, Recording and Reporting of Stereotactic Treatments with Small Photon Beams," Journal of the International Commission on Radiation Units and Measurements **14** (2014).

[8] J. T. Bushberg, J. A. Seibert, E. M. Leidholdt, Jr., and J. M. Boone, *The Essential Physics of Medical Imaging*. Lippincott Williams & Wilkins, (2002).

[9] T. Landberg, J. Chavaudra, J. Dobbs, G. Hanks, K. A. Johansson, T. Möller, and J. Purdy, "ICRU Report 50: Prescribing, Recording and Reporting Photon Beam Therapy," Journal of the International Commission on Radiation Units and Measurements **os26** (1993).

[10] T. Landberg, J. Chavaudra, J. Dobbs, J. P. Gerard, G. Hanks, J. C. Horiot, K. A. Johansson, T. Möller, J. Purdy, N. Suntharalingam, and H. Svensson, "ICRU Report 62: Prescribing, Recording and Reporting Photon Beam Therapy (Supplement to ICRU Report 50)," Journal of the International Commission on Radiation Units and Measurements **os32** (1999).

[11] ICRU, "ICRU Report 83: Prescribing, Recording and Reporting Photon-Beam Intensity-Modulated Radiation Therapy (IMRT)," Journal of the International Commission on Radiation Units and Measurements **10** (2010).

[12] T. Bortfeld, "IMRT: a review and preview," Phys. Med. Biol. **51**, R263–R379 (2006).

[13] D. Amelio, M. Winter, D. Habermehl, O. Jäkel, J. Debus, and S. E. Combs, "Analysis of inter- and intrafraction accuracy of a commercial thermoplastic mask system used for image-guided particle radiation therapy," J. Radiat. Res. **54**, i60–i76 (2013).

[14] M. S. Hoogeman, J. J. Nyuttens, P. C. Levendag, and B. J. Heijmen, "Time dependence of intrafraction patient motion assessed by repeat stereoscopic imaging," Int. J. Radiat. Oncol., Biol., Phys. **70**, 609–618 (2007).

[15] M. Teoh, C. H. Clark, K. Wood, S. Whitaker, and A. Nisbet, "Volumetric modulated arc therapy: a review of current literature and clinical use in practice," Br J Radiol **84**, 967–996 (2011).

[16] C. X. Yu, "Intensity-modulated arc therapy with dynamic multileaf collimation: an alternative to tomotherapy," Phys. Med. Biol. **40**, 1435–1449 (1995).

[17] K. Otto, "Volumetric modulated arc therapy: IMRT in a single gantry arc," Med. Phys. **35**, 310–317 (2008).

[18] G. Smyth, P. M. Evans, J. C. Bamber, and J. L. Bedford, "Recent developments in non-coplanar radiotherapy," Br. J. Radiol. **92** (2019).

[19] J. Mullins, M.-A. Renaud, V. Heng, R. Ruo, F. DeBlois, and J. Seuntjens, "Trajectory-based VMAT for cranial targets with delivery at shortened SAD," Med. Phys. **47**, 3103–3112 (2020).

[20] J. Mullins, M.-A. Renaud, M. Serban, and J. Seuntjens, "Simultaneous trajectory generation and volumetric modulated arc therapy optimization," Med. Phys. **47**, 3078–3090 (2020).

[21] E. B. Podgorsak, *Radiation Physics for Medical Physicists*. Springer, (2010).

[22] P. R. Almond, P. J. Biggs, B. M. Coursey, W. F. Hanson, M. S. Huq, R. Nath, and D. W. O. Rogers, "AAPM's TG-51 protocol for clinical reference dosimetry of high-energy photon and electron beams," Med. Phys. **26**, 1847–1870 (1999).

[23] I. J. Das, C.-W. Cheng, R. J. Watts, A. Ahnesjö, J. Gibbons, X. A. Li, J. Lowenstein, R. K. Mitra, W. E. Simon, and T. C. Zhu, "Accelerator beam data commissioning equipment and procedures: Report of the TG-106 of the Therapy Physics Committee of the AAPM," Med. Phys. **35**, 4186–4215 (2008).

[24] D. A. Low, J. M. Moran, J. F. Dempsey, L. Dong, and M. Oldham, "Dosimetry tools and techniques for IMRT," Med. Phys. **38**, 1313–1338 (2011).

[25] I. Kawrakow, "Accurate condensed history Monte Carlo simulation of electron transport. I EGSnrc, the new EGS4 version," Med. Phys. **27**, 485–498 (1999).

[26] A. Ahnesjö, "Dose calculations for external photon beams in radiotherapy," Phys. Med. Biol. **44**, R99–R152 (1999).

[27] J. Sievinen, W. Ulmer, and W. Kaissl, "AAA Photon Dose Calculation Model in Eclipse," tech. rep., Varian Medical Systems, (2005).

[28] A. Fogliata, G. Nicolini, E. Vanetti, A. Clivio, and L. Cozzi, "Dosimetric validation of the anisotropic analytical algorithm for photon dose calculation: fundamental characterization in water," Phys. Med. Biol. **51**, 1421–1438 (2006).

[29] A. Van Esch, L. Tillikainen, J. Pyykkonen, M. Tenhunen, H. Helminen, S. Siljamäki, J. Alakuijala, M. Paiusco, and M. I. amd Dominique P Huyskens, "Testing of the analytical anisotropic algorithm for photon dose calculation," Med. Phys. **33**, 4130–4148 (2006).

[30] F. Hasenbalg, H. Neueunschwander, R. Mini, and E. J. Born, "Collapsed cone convolution and analytical anisotropic algorithm dose calculations comparted to VMC++ Monte Carlo simulations in clinical cases," Phys. Med. Biol **52**, 3679–3691 (2007).

[31] A. Ahnesjö, "Collapsed cone convolution of radiant energy for photon dose calculation in heterogeneous media," Med. Phys. **16**, 577–592 (1989).

[32] N. Childress, E. Stevens, D. Eklund, and M. Zhang, "Mobius3d White Paper: Dose Calculation Algorithm," tech. rep., Mobius Medical Systems, (2012).

[33] M. Miften, A. Olch, D. Mihailidis, J. Moran, T. Pawlicki, A. Molineau, H. Li, K. Wijesooriya, J. Shi, P. Xia, N. Papanikolaou, and D. A. Low, "Tolerance limits and methodologies for IMRT measurement-based verification QA: Recommendations of AAPM Task Group No. 218," Med. Phys. **45**, e53–e83 (2018).

[34] D. A. Low and J. F. Dempsey, "Evaluation of the gamma dose distribution comparison method," Med. Phys. **30**, 2455–2464 (2003).

[35] G. A. Ezzell, J. W. Burmeister, N. Dogan, T. J. LoSasso, J. G. Mechalakos, D. Mihailidis, A. Molineau, J. R. Palta, C. R. Ramsey, B. J. Salter, J. Shi, P. Xia, N. J. Yue, and Y. Xiao, "IMRT commissioning: Multiple institution planning and dosimetry comparisons, a report from AAPM Task Group 119," Med. Phys. **36**, 5359–5373 (2009).

[36] M. S. Bazaraa, H. D. Sherali, and C. M. Shetty, *Nonlinear Programming: Theory and Algorithms*. John Wiley & Sons, 3 ed., (2006).

[37] J.-B. Hiriart-Urruty and C. Lemaréchal, *Convex Analysis and Minimization Algorithms I*. Springer, (1996).

[38] D. G. Luenberger and Y. Ye, *Linear and Nonlinear Programming*. Springer, 4 ed., (2016).

[39] P. J. M. Laarhoven and E. H. L. Aarts, *Simulated Annealing: Theory and Applications*. Springer, (1987).

[40] A. Wachter and L. T. Biegler, "On the Implementation of a Primal-Dual Interior Point Filter Line Search Algorithm for Large-Scale Nonlinear Programming," Mathematical Programming **106**, 25–57 (2006).

[41] B. Choi and J. O. Deasy, "The generalized equivalent uniform dose function as a basis for intensity-modulated treatment planning," Phys. Med. Biol. **47**, 3579–3589 (2002).

[42] Q. Wu, R. Mohan, A. Niemierko, and R. Schmidt-Ullrich, "Optimization of intensity-modulated radiotherapy plans based on the equivalent uniform dose," Int. J. Radiat. Oncol., Biol., Phys. **52**, 224–235 (2002).

[43] H. E. Romeijn, J. F. Dempsey, and J. G. Li, "A unifying framework for multi-criteria fluence map optimization models," Phys. Med. Biol. **49**, 1991–2013 (2004).

[44] T. Bortfeld, "Optimized planning using physical objectives and constraints," Seminars in Radiation Oncology **9**, 20–34 (1999).

[45] J. O. Deasy, "Multiple local minima in radiotherapy optimization problems with dose-volume constraints," Med. Phys. **24**, 1157–1161 (1997).

[46] J. Llacer, J. O. Deasy, T. R. Bortfeld, T. D. Solberg, and C. Promberger, "Absence of multiple local minima effects in intensity modulated optimization with dose-volume constraints," Phys. Med. Biol. **48**, 183–210 (2003).

[47] J. M. Galvin, X.-G. Chen, and R. M. Smith, "Combining multileaf fields to modulate fluence distributions," Int. J. Radiat. Oncol., Biol., Phys. **27**, 697–705 (1993).

[48] S. Webb, "Optimizing the planning of intensity-modulated radiotherapy," Phys. Med. Biol. **39**, 2229–2246 (1994).

[49] T. R. Bortfeld, D. L. Kahler, T. J. Waldron, and A. L. Boyer, "X-ray field compensation with multileaf collimator," Int. J. Radiat. Oncol., Biol., Phys. **28**, 723–730 (1994).

[50] P. Xia and L. J. Verhey, "Multileaf collimator leaf sequencing algorithm for intensity modulated beams with multiple static segments," Med. Phys. **25**, 1424–1434 (1998).

[51] D. J. Convery and M. E. Rosenbloom, "The generation of intensity-modulated fields for conformal radiotherapy by dynamic collimation," Phys. Med. Biol. **37**, 1359–1374 (1992).

[52] S. V. Spirou and C. S. Chui, "Generation of arbitrary intensity profiles by dynamic jaws or multileaf collimators," Med. Phys. **21**, 1031–1041 (1994).

[53] J. Stein, T. Bortfeld, B. Dorschel, and W. Schlegel, "Dynamic x-ray compensation for conformal radiotherapy by means of multi-leaf collimation," Radiother. Oncol. **32**, 163–173 (1994).

[54] D. M. Shepard, M. A. Earl, X. A. Li, S. Naqvi, and C. Yu, "Direct aperture optimization: A turnkey solution for step-and-shoot IMRT," Med. Phys. **29**, 1007–1018 (2002).

[55] H. E. Romeijn, R. K. Ahuja, J. F. Dempsey, and A. Kumar, "A column generation approach to radiation therapy treatment planning using aperture modulation," SIAM J. Optim. **15**, 838–862 (2005).

[56] J. Unkelbach, T. Bortfeld, D. Craft, M. Alber, M. Bangert, R. Bokrantz, D. Chen, R. Li, L. Xing, C. Men, S. Nill, D. Papp, E. Romeijn, and E. Salari, "Optimization approaches to volumetric modulated arc therapy planning," Med. Phys. **42**, 1367–1377 (2015).

[57] S. Luan, C. Wang, D. Cao, D. Z. Chen, D. M. Shepard, and C. X. Yu, "Leaf-sequencing for intensity-modulated arc therapy using graph algorithms," Med. Phys. **35**, 61–69 (2008).

[58] K. Bzdusek, H. Friberger, K. Eriksson, B. Hårdemark, D. Robinson, and M. Kaus, "Development and evaluation of an efficient approach to volumetric arc therapy planning," Med. Phys. **36**, 2328–2338 (2009).

[59] J. L. Bedford, "Treatment planning for volumetric modulated arc therapy," Med. Phys. **36**, 5128–5138 (2009).

[60] C. Men, H. E. Romeijn, X. Jia, and S. B. Jiang, "Ultrafast treatment plan optimization for volumetric modulated arc therapy (VMAT)," Med. Phys. **37**, 5787–5791 (2009).

[61] F. Peng, X. Jia, X. Gu, M. A. Epelman, H. E. Romeijn, and S. B. Jiang, "A new column-generation-based algorithm for VMAT treatment plan optimization," Phys. Med. Biol. **57**, 4569–4588 (2012).

[62] M.-A. Renaud, M. Serban, and J. Seuntjens, "On mixed electron-photon radiation therapy optimization using the column generation approach," Med. Phys. **44**, 4287–4298 (2017).

[63] E. B. Podgorsak, A. Olivier, M. Pla, P.-Y. Lefebvre, and J. Hazel, "Dynamic stereotactic radiosurgery," Int. J. Radiat. Oncol., Biol., Phys. **14**, 115–126 (1988).

[64] S. F. Shaitelman, L. H. Kim, D. Yan, A. A. Martinez, F. A. Vicini, and I. S. Grills, "Continuous arc rotation of the couch therapy for the delivery of accelerated partial breast irradiation: a treatment planning analysis," Int. J. Radiat. Oncol., Biol., Phys. **80**, 771–778 (2011).

[65] B. Fahimian, V. Yu, K. Horst, L. Xing, and D. Hristov, "Trajectory modulated prone breast irradiation: a LINAC-based technique combining intensity modulated delivery and motion of the couch," Radiother. Oncol. **109**, 475–481 (2013).

[66] C. C. Popescu, W. A. Beckham, V. V. Patenaude, I. A. Olivotto, and M. T. Vlachaki, "Simultaneous couch and gantry dynamic arc rotation (CG-Darc) in the treatment of breast cancer with accelerated partial breast irradiation(APBI): a feasibility study," J. Appl. Clin. Med. Phys. **14**, 161–175 (2012).

[67] M. Langhans, J. Unkelbach, T. Bortfeld, and D. Craft, "Optimizing highly noncoplanar VMAT trajectories: the NoVo method," Phys. Med. Biol. **63**, 025023 (2018).

[68] Y. Yang, P. Zhang, L. Happersett, J. Xiong, J. Yang, M. Chan, K. Beal, G. Mageras, and M. Hunt, "Choreographing couch and collimator in volumetric modulated arc therapy," Int. J. Radiat. Oncol., Biol., Phys. **80**, 1238–1247 (2011).

[69] R. L. MacDonald and C. G. Thomas, "Dynamic trajectory-based couch motion for improvement of radiation therapy trajectories in cranial SRT," Med. Phys. **42**, 2317–2325 (2015).

[70] R. L. MacDonald, J. L. Robar, and C. G. Thomas, "Overlap-guided fixed-patient support positioning optimization for cranial SRT," Med. Phys. **44**, 17–27 (2017).

[71] G. Smyth, J. C. Bamber, P. M. Evans, and J. L. Bedford, "Trajectory optimization for dynamic couch rotation during volumetric modulated arc therapy," Phys. Med. Biol. **58**, 8163–8177 (2013).

[72] E. W. Dijkstra, "A note on two problems in connexion to graphs," Numerische Mathematik **1**, 269–271 (1959).

[73] E. P. Hart, N. J. Nilsson, and B. Raphael, "A formal basis for the heuristic determination of minimum cost paths," IEEE Transactions on System Science and Cybernetics **4**, 100–107 (1968).

[74] D. Papp, T. Bortfeld, and J. Unkelbach, "A modular approach to intensity-modulated arc therapy optimization with noncoplanar trajectories," Phys. Med. Biol. **60**, 5179–5198 (2015).

[75] E. Wild, M. Bangert, S. Nill, and U. Oelfke, "Noncoplanar VMAT for nasopharyngeal tumors: Plan quality versus treatment time," Med. Phys. **42**, 2157–2168 (2015).

[76] J. Krayenbuehl, J. B. Davis, and I. F. Ciernik, "Dynamic intensity-modulated non-coplanar arc radiotherapy (INCA) for head and neck cancer," Radiother. Oncol. **81**, 151–157 (2006).

[77] B. Wilson, K. Otto, and E. Gete, "A simple and robust trajectory-based stereotactic radiosurgery treatment," Med. Phys. **44**, 240–248 (2017).

[78] G. Smyth, P. M. Evans, J. C. Bamber, H. C. Mandeville, L. C. Welsh, F. H. Saran, and J. L. Bedford, "Non-coplanar trajectories to improve organ at risk sparing in volumetric modulated arc therapy for primary brain tumors," Radiother. Oncol. **121**, 124–131 (2016).

[79] Q. Lyu, V. Y. Yu, D. Ruan, R. Neph, D. O'Connor, and K. Sheng, "A novel optimization framework for VMAT with dynamic gantry couch rotation," Phys. Med. Biol. **63**, 125013 (2018).

[80] P. Dong, H. Liu, and L. Xing, "Monte Carlo tree search-based non-coplanar trajectory design for station parameter optimized radiation therapy (SPORT)," Phys. Med. Biol. **63**, 135014 (2018).

[81] P. Zhang, L. Happersett, Y. Yang, Y. Yamada, G. Mageras, and M. Hunt, "Optimization of collimator trajectory in volumetric modulated arc therapy: development and evaluation for paraspinal SBRT," Int. J. Radiat. Oncol. Biol. Phys. **77**, 591–599 (2010).

[82] R. L. MacDonald, C. G. Thomas, and A. Syme, "Dynamic collimator trajectory algorithm for multiple metastases dynamic conformal arc treatment planning," Med. Phys. **45**, 5–17 (2018).

[83] M. K. Fix, D. Frei, W. Volken, D. Terribilini, S. Mueller, O. Elicin, H. Hemmatazad, D. M. Aebersold, and P. Manser, "Part 1: Optimization and evaluation of dynamic trajectory radiotherapy," Med. Phys. **45**, 4201–4212 (2018).

[84] V. Y. Yu, B. P. Fahimian, L. Xing, and D. H. Hristov, "Quality control procedures for dynamic treatment delivery techniques involving couch motion," Med. Phys. **41**, 081712 (2014).

[85] A. Rodrigues, F.-F. Yin, and Q. Wu, "Dynamic electron arc radiotherapy (DEAR): a feasibility study," Phys. Med. Biol. **59**, 327–345 (2014).

[86] V. Y. Yu, A. Landers, K. Woods, D. Nguyen, M. Cao, D. Du, R. K. Chin, K. Sheng, and T. B. Kaprealian, "A prospective 4π radiation therapy clinical study in recurrent high-grade glioma patients," Int. J. Radiat. Oncol., Biol., Phys. **101**, 144–151 (2018).